International Journal of Engineering Technologies (IJET)

Printed ISSN: 2149-0104
e-ISSN: 2149-5262

Volume: 5
No: 2
June 2019

International Journal of Engineering Technologies is an international peer–reviewed journal and published quarterly. The opinions, thoughts, postulations or proposals within the articles are but reflections of the authors and do not, in any way, represent those of the Istanbul Gelisim University.

CORRESPONDENCE and COMMUNICATION:

Istanbul Gelisim University Faculty of Engineering and Architecture
Cihangir Mah. Şehit P. Onb. Murat Şengöz Sk. No: 8
34315 Avcilar / Istanbul / TURKEY
Phone: +90 212 4227020 **Ext.** 159 or 221
Fax: +90 212 4227401
e-Mail: ijet@gelisim.edu.tr
Web site: https://ijet.gelisim.edu.tr
https://dergipark.org.tr/ijet
Twitter: @IJETJOURNAL

Printing and binding:
Anka Matbaa
Certificate Number: 12328
Phone: +90 212 5659033 - 4800571
E-mail: ankamatbaa@gmail.com

International Journal of Engineering Technologies (IJET) is included in:

International Journal of Engineering Technologies (IJET) is harvested by the following service:

Organization	URL	Starting Date
The OpenAIRE2020 Project	https://www.openaire.eu	2015
GOOGLE SCHOLAR	https://scholar.google.com.tr/	2015
WORLDCAT	https://www.worldcat.org/	2015
IDEALONLINE	http://www.idealonline.com.tr/	2018

INTERNATIONAL JOURNAL OF ENGINEERING TECHNOLOGIES (IJET)
International Peer–Reviewed Journal
Volume 5, No 2, June 2019 - Printed ISSN: 2149-0104, e-ISSN: 2149-5262

Editorial Board

Professor Birsen YAZICI, Rensselaer Polytechnic Institute, United States

Professor Mohammad ZAMI, King Fahd University of Petroleum and Minerals, Saudi Arabia

Associate Professor Lale T. ERGENE, Istanbul Technical University, Turkey

Associate Professor Leila PARSA, Rensselaer Polytechnic Institute, United States

Associate Professor Yuichiro SHIBATA, Nagasaki University, Japan

Associate Professor Kiruba SIVASUBRAMANIAM HARAN, University of Illinois, United States

Associate Professor Yilmaz SOZER, University of Akron, United States

Associate Professor Mohammad TAHA, Rafik Hariri University (RHU), Lebanon

Assistant Professor Kyungnam KO, Jeju National University, Republic of Korea

Assistant Professor Hidenori MARUTA, Nagasaki University, Japan

Assistant Professor Hulya OBDAN, Istanbul Yildiz Technical University, Turkey

Assistant Professor Mehmet Akif SENOL, Istanbul Gelisim University, Turkey

Dr. Jorge Guillermo CALDERÓN-GUIZAR, Instituto de Investigaciones Eléctricas, Mexico

Dr. Rafael CASTELLANOS-BUSTAMANTE, Instituto de Investigaciones Eléctricas, Mexico

Dr. Guray GUVEN, Conductive Technologies Inc., United States

Dr. Tuncay KAMAS, Eskişehir Osmangazi University, Turkey

Dr. Nobumasa MATSUI, Faculty of Engineering, Nagasaki Institute of Applied Science, Nagasaki, Japan

Dr. Cristea MIRON, Politehnica University in Bucharest, Romania

Dr. Hiroyuki OSUGA, Mitsubishi Electric Corporation, Japan

Dr. Youcef SOUFI, University of Tébessa, Algeria

Dr. Hector ZELAYA, ABB Corporate Research, Sweden

From the Editor

Dear Colleagues,

On behalf of the editorial board of International Journal of Engineering Technologies (IJET), I would like to share our happiness to publish the 18th issue of IJET. My special thanks are for members of Editorial Board, Publication Board, Editorial Team, Referees, Authors and other technical staff.

Please find the 18th issue of International Journal of Engineering Technologies at http://ijet.gelisim.edu.tr or http://dergipark.gov.tr/ijet. We invite you to review the Table of Contents by visiting our web site and review articles and items of interest. IJET will continue to publish high level scientific research papers in the field of Engineering Technologies as an international peer-reviewed scientific and academic journal of Istanbul Gelisim University.

Thanks for your continuing interest in our work,

Professor Mustafa BAYRAM
Istanbul Gelisim University
mbayram@gelisim.edu.tr

---

http://ijet.gelisim.edu.tr
http://dergipark.gov.tr/ijet
Printed ISSN: 2149-0104
e-ISSN: 2149-5262


International Journal of
Engineering Technologies
IJET

Table of Contents

International Journal of Engineering Technologies, IJET

e-Mail: ijet@gelisim.edu.tr
Web site: https://ijet.gelisim.edu.tr
https://dergipark.org.tr/ijet
Twitter: @IJETJOURNAL

A Framework for Production Capacity and Time Utilization of Mono Product Sequential Process Plants

Olayinka Mohammed Olabanji

Department of Mechanical Engineering, School of Engineering and Engineering Technology, Federal University of Technology Akure, P. M. B 704 Akure, Ondo State

Tel: +2348038552639, omolabanji@futa.edu.ng

Received: 07.01.2019 Accepted:14.05.2019

Abstract- This article addresses the challenges of estimating production capacity and time utilization problem in a sequential process plant. A framework and mathematical model are presented to aid the analysis and understanding of the proposed solution. A set of constraints is provided in order to specify the requirements for production capacity and time utilization planning in a sequential process plant. In order to ascertain the performance of the framework, the mathematical models derived are tested using an existing designed process plant and the results obtained from the evaluation are also presented. The proposed model generates the utilized time for the process plant per batch and also the production capacity of the process plant as well as the production rates of individual machines in the process plant. Application of the model to an existing process plant demonstrates that the addition of buffer storage to store work in progress materials in a mono product sequential process plant will increase the production rate of the plant but the production rate of the machines in the plant remains constant. Also, the addition of buffer storage will increase the time utilized by the process plant to complete its operation per batch.

Keywords Process plants, Production capacity and planning, production framework.

1. Introduction

Sustainable national economic advancement can be attained through longevity of manufacturing firms which can be achieved by effective and continuous production capacity planning and time utilization of process plants in the firms. Production capacity and time utilization planning of process plant is a major task in process engineering. It is an essential stage in the design of a process plant that occurs in vast range of industries in process engineering [1-3]. These industries include chemical, agriculture, food, advanced material, mineral, pharmaceuticals and petrochemical among others. Production capacity and time utilization planning starts from the developmental stage of a process plant. It is usually conceptualized alongside the needs of the customers and it is factored in the design of production facilities that transform raw materials into finish products required by customers [4]. The design of process plants begins with the identification and establishment of process required to accomplish the transformation of raw material or resources. This is usually followed by conceptual and detail design of all the machines required for processes in the plant. Efforts are made by engineers to standardize the output of all the machines in the process plant. However, different machines in a plant may have different capacities due to factors or constraints such as availability of space, environmental impacts, safety precautions, capital involvement, operation and maintenance costs [5].

Furthermore, there is a wide range of technical factors that dictates the sizes and capacities of the machines in a process plant. These factors are the physical dimensions of the machines in comparison with the availability of space and building dimensions, arrangement of the machines in the plant, operating parameters of the prime movers in the process plant and availability of resources such as water and electricity [6]. In order to achieve the development of a safe and effective process plant, the engineer is required to provide a holistic view of the processes involved in the process plant and analyze the operating conditions of the machines in the process plant. This is usually achieved by developing models and simulations. The analysis of processes and machines involved will shed light on the sequence of operation of the machines depending on the type of production process and the stages involved in the transformation of the raw material into finished good [7].

Process plants can be classified based on the type of product it handles and the nature of the processes involved in the plant. Classification based on the products are the type of industries identified above. Sometimes, when the output of the process plant is a continuous stream of a particular type of product as a result of adding of one type of raw material, the plant is called a mono product process plant.

Classification based on the nature can further be grouped into concurrent and sequential process plants. Concurrent process plants are usually encountered when there are two different operations in the processing that must be done simultaneously. In this case two different machines will operate in conjunction with one another and the outputs from the machines are different from each other. The completion time of the two machines may be equal or unequal but, in most cases, it is usually unequal. In some cases, the raw materials in this type of process plants are usually more than one [4]. The sequential process plants are encountered in situations when one operation must be completed before another operations starts. In some cases, the succeeding operations may start when the preceding operation is about to finish. Both categories of process plants usually operate effectively when the system is automated [8].

The production capacity of a process plant can be defined as the maximum amount of product that can be produced per unit time with existing machines and resources used in the plant provided that the availability of variable factors of production is not restricted [9-10]. The time involved in this definition is the utilized time or duration of operation of the process plant. Considering this definition, it is necessary to consider the variable factors that must not be restricted in the production process. These factors are; availability of raw materials for the process plant, product demand by customers, availability of power, availability of workspace for storage of raw material, work in progress and finished goods [3]. These factors play major roles in affecting the operations of the plant. Considering the effect of availability of raw material, process plants that work on seasonal materials will have to stop operation when there is scarcity of the raw material. When there is abundance of raw material the machine will have to produce excessively and it will be difficult to ascertain the capacity of the plant over a period of scarcity and surplus raw material except if it is based on just in time production [11].

Fluctuations in demand of the product also affects the capacity of the plant especially when the product cannot stay for a long time in the processing factory. Most of the time a balance needs to be created between the lead time and quantity of product required from the plant. This is necessary in order to ensure that the production rate of the plant is fully optimized in order to satisfy the fluctuations in demand of the customers [12]. The production rate in this case can be defined as the number of final products that the plant will turn out during a given period of time (which is usually expressed in batch). In practice, it is usually necessary to improvise a buffer store for work in progress along the process plant in order to maximize the high production capacity of some machines in the process plant. The buffer store can be defined as a temporary storage in a process plant where stocks (that are work in progress) can be stored while awaiting further processing. This also assist the process plant to achieve its optimal production capacity [13].

Considering these factors, there is a need to establish the production capacity of process plants and time utilization because this will assist in estimating the total amount of the product that the plant can produce and the time required by the plant to produce the estimated capacity per batch of production [14-15]. The aim of this article is to develop a framework and a mathematical model that will assist in evaluating the production capacity and time utilization of a sequential process plant. The novelty of the developed model is the ability to consider the outputs of individual machines alongside their utilized time and selecting the machines with the smallest output as a benchmark. A summation of the time utilized by each machine in the process plant and handling time gives the total utilized time by the process plant. Furthermore, the model also considers the introduction of buffer storage to machines with higher production capacity in order to increase the overall capacity of the process plant. However, this will increase the time utilized by the plant because the time spent to process the work in progress from the buffer storage will be added to the total utilized time.

2. Materials and Methods

2.1. Framework and Mathematical Model for Capacity Planning and Time Utilization

In order to create a flow of the proposed model, it is necessary to develop a framework to analyze the basic necessities, operations and requirements of a sequential process plant. Figure 1 shows the developed framework. Considering Fig. 1, it is evident that a production capacity model will be effective when all the capacity of machines in the plant are established and regulated so that the output from the last machine in the plant will be the same as the outputs from other machines in the process plant [16]. It is also clear from the model that capacity of the process plant can also be affected by the presence or absence of buffer store for work in progress depending on whether there is a machine in the plant that can be designed for high capacity without exceeding the available space or affecting other machines in the plant. Also, the time utilization is a function of the time spent by all the machines in the plant and the loading time from the buffer stores in the process plant [17-19].

2.2. Definitions and Formulations

In order to simplify the analysis, it is necessary to consider the definitions of the notations and symbols used in the formulation. These symbols and notations are presented as follows;

$M_i =$ Number of Machines in the process plant;

$M_{C_i} =$ The Capacity of machines in the plant that can be transferred from one machine to another (kg)

$B_{C_n} =$ Capacity of the buffers that can be loaded on the machines working on buffer (kg)

$n =$ Number of times the buffers loads work in progress into the process plant

$M_{B_m} =$ Capacity of the machines working on the work in progress stored in the buffer (kg)

$nB =$ Number of buffer in the process plant

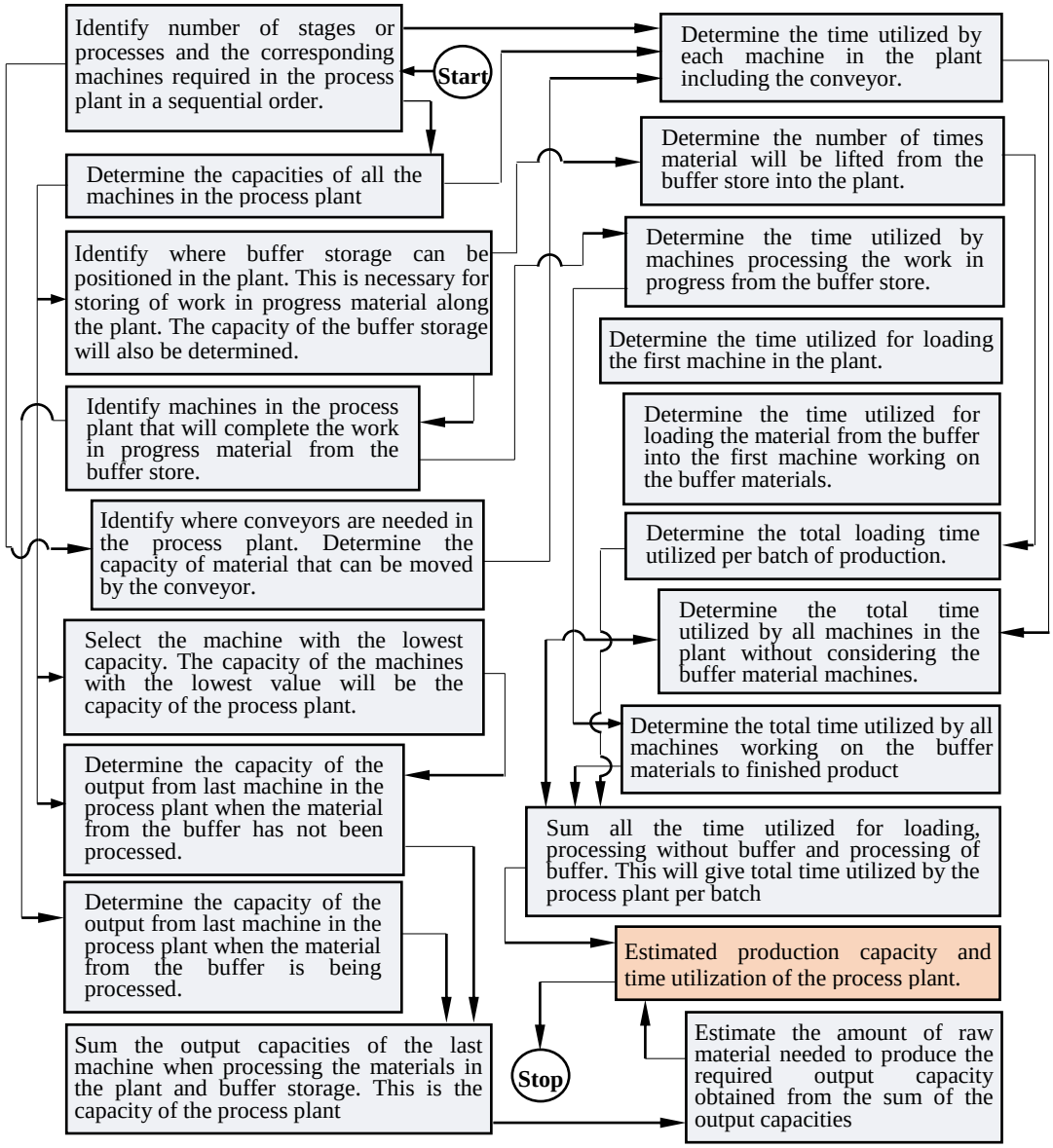

Fig. 1. Framework of the proposed model for estimating production capacity and time utilization sequential process plants.

M_{P1} = Capacity of the process plant excluding the material processed from the buffer (*kg*)

M_{P2} = Capacity of the process plant as a result of materials processed from the buffer (*kg*)

M_P = Total capacity of the process plant per batch (*kg*)

P_R = Production rate of process plant on an hour (*kg/hr*)

M_{t_i} = Time spent by each machine in the process plant including conveyors (*hr*)

M_{tm} = Time spent by machines working on materials from buffer work in progress (*hr*)

M_{P_t} = Time utilized by the plant to produce per batch (*hr*)

M_{Pt_1} = Time required by the process plant to produce per batch excluding the processing of buffer materials (*hr*)

M_{Pt_2} = Time required by the process plant for processing of the buffer materials (*hr*)

T_L = Total loading time (*hr*)

P_{RM_i} = Production rate of each machine in the process plant (*kg/hr*)

T_{m_1} = Time required to load the first machine in the process plant with material (*hr*)

N_{mB} = Number of machines working on buffer stored materials

T_B = Time required to load the work in progress materials from buffer to first machine working on the buffer (*hr*).

In order to simplify the analysis, it is necessary to make the following assumptions;

1. The plant is fully automated and individual machines in the plant are arranged in such a way

that the output of one machine is transferred directly to the next machine as input. Hence, the volume of the inputs for the succeeding machine is equal to the volume of the output of the preceding machine.

2. Minimal material lost in each of the machine is negligible. Hence, the capacity of a machine in the plant will be transferred totally to another machine and this will be taken as the output of the process plant. i.e. $M_{C_i} = \text{Constant}$; $M_{B_m} = \text{Constant}$.
3. The target capacity of the process plant is equal to the output capacity of any of the machine in the process plant that can be transferable to other machines in the plant. Also, the completion time of the process plant is the summation of individual completion time of all the machines because it is expected that all the machines in the process plant would have completed their operation before the final product is obtained.
4. The machines in the plant are arranged to work in a sequential order. However, some may be allowed to work when the preceding machine is about to finish. This implies that, the operation of one machine depends on the successful completion of the previous machine or the desired completion time of the preceding machine.

Firstly, considering assumption three, since the machines in the plant are arranged in a sequential manner, it follows that;

$$M_{P1} = \text{Min}\left\{M_{C_i}\right\} \tag{1}$$

Since the number of times the buffer can load materials into the plant is represented by *n* it follows that;

$$M_{P2} = \sum_{nB=0}^{nB} n\left[\text{Min}\left\{B_{c_n}\right\}\right] \tag{2}$$

Since the capacity of the plant is a function of the output volume or mass of the last machine, it can be deduced that the capacity of the process plant is a summation of the output excluding the material processed from the buffer store and the output of machines obtained by processing the work in progress materials in the buffer. In essence the total capacity of the plant can be expressed as;

$$M_P = M_{P1} + M_{P2} \tag{3}$$

Combining equations (1), (2) and (3) the expression for the total capacity of the process plant can be obtained as;

$$M_P = \text{Min}\left\{M_{C_i}\right\} + \sum_{nB=0}^{nB} n\left[\text{Min}\left\{B_{c_n}\right\}\right] \tag{4}$$

Furthermore, it is evident that the time required by the plant to produce per batch excluding the buffer materials is a function of individual time spent by each machine in the plant and as such this can be represented as;

$$M_{Pt_1} = \sum_{i=1}^{i} M_{t_i} \tag{5}$$

Additionally, depending on the size and number of buffers, the total loading time is a summation of the time required to load the first machine working on buffer stock in the plant, and the first machine in the process plant. The time required to load the first machine working on the buffer is a function of the number of times materials are loaded from the buffer and the number of buffers in the plant. Hence, the total loading time can be expressed as;

$$T_L = T_{m1} + nT_B \tag{6}$$

The time required to process the materials from the buffer is a function of the number of times the buffer supplies the machines and the time spent by the machines handling the work in progress from the buffer. This will be greatly affected by the number of buffers in the process plant. In essence, the time required to completely process the material from the buffer can be obtained from;

$$M_{Pt_2} = n\left[\sum_{N_{mB}=1}^{N_{mB}} M_{tm_n}\right] \tag{7}$$

The total time utilized by the plant is a function of the time spent on loading, time spent by individual machines when processing the actual capacity and time spent to process the work in progress from the buffer store. This can be expressed as presented in equation (8);

$$M_{P_t} = M_{Pt_1} + M_{Pt_2} + T_L \tag{8}$$

Combining equations 5, 6, 7 and 8, the total time utilized by the process plant per batch can be deduced as;

$$M_{P_t} = \sum_{i=1}^{i} M_{t_i} + n\left[\sum_{N_{mB}=1}^{N_{mB}} M_{tm_n}\right] + T_{m\,1} + nT_B \tag{9}$$

The rate of production of the plant (P_R) in an hour can be deduced as;

$$P_R = \frac{M_P}{M_{P_t}} \tag{10}$$

Combining equations (4), (9) and (10) we obtain;

$$P_R = \frac{M_{C_i} + \sum_{nB=0}^{nB} nB_{c_n}}{\sum_{i=1}^{i} M_{t_i} + n\left[\sum_{N_{mB}=1}^{N_{mB}} M_{tm_n}\right] + T_{m\,1} + nT_B} \tag{11}$$

This expression can be used to determine the capacity of the process plant per day provided that the number of working hours per day is specified for the operators. The production rate of each machine in the process plant $\left(P_{RM_i}\right)$ can also be obtained by dividing the total capacity of the process plant by the time spent by the machines in each operation. This can be expressed as;

$$P_{RM_i} = \frac{M_P}{M_{t_i}} \quad (12)$$

2.3 Application of the framework to a *Poundo* yam process plant

In order to test the developed mathematical model, a process plant for production of *Poundo* yam [6, 20] will be used as a case study in this article. The process plant transforms yam into a flour that can be used to make a doughy food called *Poundo* yam. The plant has seven machines operating sequentially and performing different operations. The operations in the plant are washing, peeling and slicing, parboiling, conveying, drying, milling and sieving.

Since there is no buffer in the process plant, the buffer components of the equations will be neglected. These operations are carried out sequentially with the aid of different machines as presented in Fig. 2 and Fig. 3. The following data are obtained from the operation of the process plant as presented in Table 1.

Considering assumption 3, the transferable output that can be handled by all the machines in the process plant is *0.635* m^3 of sliced cubes of yam. Hence the target capacity of the *Poundo* yam process plant (M_{ci}) is *0.635* m^3. In order to determine the time utilized by the washing ($M_{t\ washing}$) and peeling/slicing ($M_{t\ peeling}$) machines to produce the target capacity of the process plant, it is necessary to consider the bulk density and average mass of yam that will produce *0.635* m^3 of the sliced cubes of yam. The average mass and bulk density of yam are *5 kg* and *1104* kg/m^3 respectively [21-23].

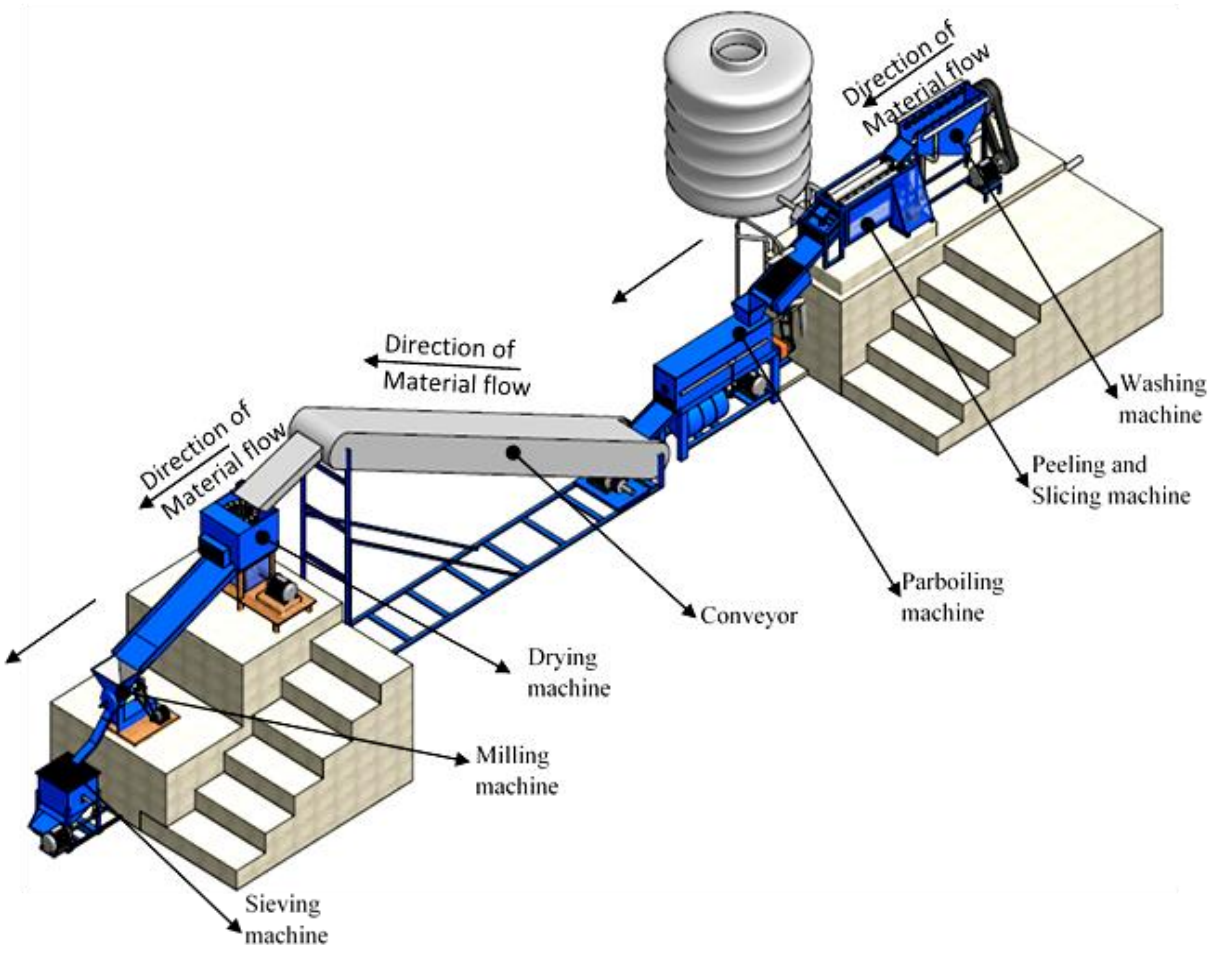

Fig. 2. A pictorial View of the *Poundo* Yam Process Plant [20]

Table 1. Data obtained from the operation of the *Poundo* yam process plant

S/N	Machines	Machine Outputs (MC_i)	Time Utilized (M_{ti})
1	Washing machine	(MC_1): Continuous production	*(1.5 min/tuber)*
2	Peeling and Slicing Machine	(MC_2): Continuous production	*(1.25 min/tuber)*
3	Parboiling Machine	(MC_3): *0.635 m^3* of sliced cubes	$M_{t\ parboiling}$: *3 hrs.*
4	Conveyor	(MC_4): Continuous operation (*1.52 tons/hr.*)	$M_{t\ conveying}$: *(25/60) hr.*
5	Drying Machine	(MC_5): *0.771 m^3* of sliced cubes	$M_{t\ drying}$: *3 hrs.*
6	Milling Machine	(MC_6): *0.738 m^3* of sliced cubes	$M_{t\ milling}$: *(15/60) hr.*
7	Sieving Machine	(MC_7): *0.682 m^3* of sliced cubes	$M_{t\ sieving}$: *(22/60) hr.*

Fig. 3. Fabricated *Poundo* Yam Process Plant [20]

Hence;

$$M_{twashing} = \left[\frac{M_{ci} * \rho_{yam}}{M_{yam}}\right] * min/\ tuber\big|_{washing} \quad (13)$$

$$M_{tpeeling} = \left[\frac{M_{ci} * \rho_{yam}}{M_{yam}}\right] * min/\ tuber\big|_{peeling} \quad (14)$$

Therefore,

$$M_{twashing} = \left[\frac{0.635*1104}{5}\right] * 1.5 = 3.5\ hrs.$$

$$M_{tpeeling} = \left[\frac{0.635*1104}{5}\right] * 1.25 = 3\ hrs$$

Furthermore, considering assumption 3 and equation 5 we can deduce that;

$$M_{Pt_1} = \sum_{i=1}^{i} M_{t_i} = M_{t_{washing}} + M_{t_{peeling}} + M_{t_{parboiling}} + M_{t_{conveying}} + M_{t_{drying}} + M_{t_{milling}} + M_{t_{sieving}} \quad (15)$$

$$\therefore M_{Pt_1} = 3.5 + 3 + 3 + \left(\frac{25}{60}\right) + 3 + \left(\frac{15}{60}\right) + \left(\frac{22}{60}\right) = 13.53\ hrs$$

Hence the mass of yam the plant can handle per batch (M_P) is $M_{yam/batch}$ can be obtained as described in equation (16) [24]:

$$M_P = M_{yam/batch} = M_{C_i} * \rho_{yam} \quad (16)$$

Where ρ_{yam} is the average density of yam

$$\therefore M_p = M_{yam/batch} = 0.635*1104 = 701.04\ kg$$

The production rate (P_R) of the *Poundo* yam process plant can be obtained from equation (10) as;

$$P_R = \frac{701.04}{13.53} = 51.8 \simeq 52\ kg/hr$$

Since the raw material processed by the plant is yam, it is necessary to express the capacity in the form of tubers. The number of tubers of yam that the plant can handle per batch $\left(N_{tubers/batch}\right)$, can be obtained from equation (17) using the average mass of a yam tuber [22-24];

$$N_{tubers/batch} = \frac{M_{yam/batch}}{M_{yam}} \quad (17)$$

$$\therefore N_{tubers/batch} = \frac{701.04}{5} = 140.2 \simeq 140\ tubers/batch$$

The production rate of the Poundo yam process plant in an hour in the form of tubers $\left(P_{R(tub)}\right)$ can also be obtained using equation 10 as;

$$P_{R(tub)} = \frac{N_{tubers/batch}}{M_{P_t}} \quad (18)$$

$$\therefore P_{R(tub)} = \frac{140}{13.53} = 10.4 \simeq 10\ tubers\ per\ hour$$

Where;

$P_{R(tub)}$ = The production rate of the *Poundo* yam process plant in form of tubers

$N_{tubers/batch}$ = Number of yam tubers the process plant can handle per batch

$M_{yam/batch}$ = Mass of yam the process plant can handle per batch

M_{yam} = Average mass of a tuber of yam

M_{Pt_1} = Time required by the *Poundo* yam process plant to produce per batch excluding the processing of buffer materials (*hr*)

However, in order to identify and ascertain the effect of buffer storage on how it affects the production capacity and time utilization, let us assume that an imaginary buffer storage which content can be loaded twice is added to the system with a negligible loading time. Since the washing machine, peeling and slicing machine are allowed to work continuously, then the excess materials processed from these machines will be stored in the buffer storage. In view of this the imaginary buffer can be positioned after the peeling and slicing machine. It is worthwhile to know that the maximum amount of work in progress that can be loaded from the buffer storage cannot be greater than the targeted capacity of the process plant.

Also, the washing and peeling/slicing machines will continue to work during the parboiling and drying operation and as such the time for washing and peeling to produce the buffer material will not be considered in the overall time of the process plant when working on buffer but will be considered for the production rate of the machines. The components of the buffer storage in the model equations will be considered in this case and as such, the plant capacity and production rate are expected to change. Hence the machines that will process the materials from the buffer storage are parboiling machine, conveyor, drying machine, milling machine and sieving machine. Furthermore, considering assumption two, the benchmarked or throughput capacity will also be produced from the plant when processing the materials from the buffer. Table 1 can be adjusted to provide details for the imaginary buffer as shown in Table 2.

Hence, the following parameters can be deduced for the imaginary buffer storage.,

$N_{mB} = 5$

$T_B = 0$

$B_{C_n} = M_{B_m} = M_{C_i} = 0.635\ m^3$

$n = 2$

$nB = 1$ (Number of buffer storage in the process plant)

From equation (2); $M_{P2} = 1.270\ m^3$

Table 2. Introduction of Imaginary buffer to the operation of the *Poundo* yam process plant

S/N	Machines	Machine Outputs (MC_i)		Time Utilized (M_{ti})	
		No Buffer	Imaginary Buffer added	No Buffer	Imaginary Buffer added
1	Washing machine	Continuous production		*(1.5 min/tuber)*	
2	Peeling and Slicing Machine	Continuous production		*(1.25 min/tuber)*	
3	Parboiling Machine	*0.635m^3*	*1.270m^3*	*3hrs*	*6hrs*
4	Conveyor	Continuous operation		*(25/60) hr*	*(25/30) hr*
5	Drying Machine	*0.771 m^3*	*1.542 m^3*	*3hrs*	*6hrs*
6	Milling Machine	*0.738 m^3*	*1.467 m^3*	*(15/60) hr*	*(15/30) hr*
7	Sieving Machine	*0.682 m^3*	*1.364 m^3*	*(22/60) hr*	*(22/30) hr*

Hence, the capacity of the process plant when the imaginary buffer is introduced is obtained from equations (3) and (4) as;

$$M_P = \text{Min}\left\{M_{C_i}\right\} + \sum_{nB=0}^{nB} n\left[\text{Min}\left\{B_{c_n}\right\}\right] =$$

$$0.635 + 1.270 = 1.905 m^3$$

Hence that volume of *Poundo* yam that the plant will produce per batch in the presence of the imaginary buffer is $1.905 m^3$. Similarly, the mass of yam that the plant can handle per batch can also be obtained from the bulk density of yam as $2103 kg$. Also, the total time utilized by the plant can also be obtained using equation (7) to (9) as follows;

$$M_{Pt_2} = n\left[\sum_{N_{mB}=1}^{N_{mB}} M_{tm_n}\right] =$$

$$2\left[3 + \left(\frac{25}{60}\right) + 3 + \left(\frac{15}{60}\right) + \left(\frac{22}{60}\right)\right] = 14.07 hrs$$

Since the loading time is negligible the total time utilized by the process plant per batch can be deduced as;

$$M_{P_t} = \sum_{i=1}^{i} M_{t_i} + n\left[\sum_{N_{mB}=1}^{N_{mB}} M_{tm_n}\right] =$$

$$13.53 + 14.07 = 27.6 hrs$$

Hence the mass of yam the plant can handle per batch with imaginary buffer (BM_P) is $BM_{yam/batch}$ can be obtained as:

$$BM_P = BM_{yam/batch} = M_P * \rho_{yam} = 1.905 * 1104 = 2103\ kg$$

Similarly, the production rate of the *Poundo* yam process plant $P_{R(buffer)}$ considering the imaginary buffer can also be obtained from equation (11) as;

$$P_{R(buffer)} = \frac{2103}{27.6} = 76.2 \simeq 76\ kg/hr$$

Also, the number of tubers of yam that the plant can handle per batch under the imaginary buffer $\left(BN_{tubers/batch}\right)$, can be obtained from;

$$BN_{tubers/batch} = \frac{BM_{yam/batch}}{M_{yam}} = \frac{2103}{5} \simeq 421\ tubers$$

Hence, the production rate of the Poundo yam process plant in an hour in the form of tubers when considering the buffer storage can also be obtained as;

$$BP_R = \frac{BN_{tubers/batch}}{M_{P_t}} = \frac{421}{27.6} = 15\ tubers/hr$$

In order to appraise the performance of the model and create a basis for comparison, another mathematical model was used to analyze the *Poundo* yam process plant. The results obtained from the comparison are presented in Table 4. The production rate, production capacity and time utilized by a mono product sequential process plant are obtained as follows [5].

$$R_P = \frac{60}{T_p} \tag{19}$$

Where R_P is the production rate and time utilized by the plant. Also, T_p is the production time per work which can be obtained from equation (20) as;

$$T_p = \frac{T_b}{Q} \tag{20}$$

Where Q is the output of the plant per batch in terms of quantity and T_b is the batch processing time of the plant which can be obtained from equation (21) as;

$$T_b = T_{su} + QT_c \tag{21}$$

Where T_{su} is the set-up time to prepare for batch production of all the machines in the process plant and T_c is the operation cycle time per batch. The production capacity of the process plant can be obtained from equation (22);

$$PC = \frac{nSHR_p}{n_o} \tag{22}$$

Where S and H are numbers of shifts per batch and Hours per batch respectively, while n and n_o are the numbers of plants in the facility and number of machines in the process plant.

3. Results

An estimation of the output capacity per batch, time utilization per batch and production rate per batch for each machine and the process plant as a whole is presented in

Table 3. This estimation is based on the presence and absence of the imaginary buffer storage in the process plant. It is evident from the results of the application of the model that the introduction of buffer into the plant increases the output capacity of the machines, time utilized and production rate of the process plant. The buffer storage did not alter the production rate of individual machines in the process plant because the production rate is a function of the machine output and utilized time. This implies that, as the machines output increases the utilized time increases and as such the production rate remains constant. However, the production rate of the process plant increases (from 51.8 *kg/hr* to 76 *kg/hr*) as the buffer storage is introduced into the plant. The increased production rate can be attributed to an increase in the utilized time. This increase is due to simultaneous operation of the machines when the buffer materials are processed. For instance, during the parboiling process the washing and peeling/slicing machine will continue to produce sliced cubes that will be stored in the buffer storage. In essence, the time utilized by the plant at this stage remains the same because the parboiling machine is still in operation while additional materials are added to the buffer storage. It can be hypothetically stated that buffer storage increases the production rate of the process plants if it will not require additional time to produce the work in progress or if the work in progress will be produced while other machines in the plant are in operation. The same scenario is experienced between the parboiling machine and drying machine because as the drying machine dries the parboiled cubes of yam from the parboiling machine another batch of sliced cubes are loaded into the parboiling machine. This implies that, the increased production rate of the process plant is due to the simultaneous operation of the machines which is contrary to the rest period experienced by the machines when there is no buffer storage in the process plant.The process plant transforms yam into a flour that can be used to make a doughy food called *Poundo* yam. The plant has seven machines operating sequentially and performing different operations. The operations in the plant are washing, peeling and slicing, parboiling, conveying, drying, milling and sieving. Since there is no buffer in the process plant, the buffer components of the equations will be neglected. These operations are carried out sequentially with the aid of different machines as presented in Figures 2 and 3. The following data presented in Table 1 are obtained from the operation of the process plant.

Considering assumption 3, the transferable output that can be handled by all the machines in the process plant is *0.635* m^3 of sliced cubes of yam. Hence the target capacity of the *Poundo* yam process plant (M_{ci}) is *0.635* m^3. In order to determine the time utilized by the washing ($M_{t\ washing}$) and peeling/slicing ($M_{t\ peeling}$) machines to produce the target capacity of the process plant, it is necessary to consider the bulk density and average mass of yam that will produce *0.635* m^3 of the sliced cubes of yam. The average mass and bulk density of yam are *5 kg* and *1104* kg/m^3 respectively [21-23].

4. Discussions

The results obtained from application of the model to the *Poundo* yam process plant shows that the mathematical model will function as intended. The model was able to obtain the production capacity of the process plant, as well as the time utilization. Furthermore, the model also obtained the production rate of individual machines in the process plant. The production rate of each machine obtained can be used to optimize the plant because it shows the machine with the highest and lowest production rate. It will also assist in positioning of buffers in the plant in order to increase the production capacity of the process plant. Considering the results presented in Table 3, a high production rate of 3259 *kg/hr* from the milling machine indicates that a buffer can be placed between the milling and sieving machine since the milling has high production rate. However, the drying machine preceding the milling machine has a low production rate and as such it can be increased or designed to be three or four drying machines in order to meet up with the high demand of the milling machine. This will also ensure that the high delivery rate of the conveyor is also utilized because the drying machine will demand for more materials when increased. Similarly, the capacities of the washing, peeling and slicing and parboiling machines can also be increased in order to meet the higher demands of machines in the system. The introduction of buffer storage in the process plant provides a significant increase in the output capacity of the process plant. However, this significant increase is reduced in the production rate of the plant as a result of time involvement. Considering this time involvement, the process plant can be optimized by introducing more machines to processes taking more time in the process plant or by improving the performance of the machines taking more time to complete their task. As stated earlier, in order to compare the performance of the developed model, another model was used to analyze the *Poundo* yam process plant. The other model used was able to estimate the production capacity, production rate and time utilization but the values obtained are different from the present study as presented in Table 4. The present study shows that the production rate of the machines in the process plant remain constant when operating the process plant with either no buffer storage or with buffer storage. Though, there is a difference in the production rate of the whole process plant when operating with buffer storage. On the other hand, the other model used for comparison shows significant difference in the production rate of the machines in the plant as well as the whole process plant. However, the production rates of the machines are expected to be constant either operating with buffer or with no buffer. This is necessary because the production rate is a function of time and output capacity. In view of this, when the buffer storage is added the time utilized increases as well as the output capacity and as such the production rate remains constant. As expected, the two

models provide substantial differences in the production capacities of the machines in the plant when operating with no buffer and when operating with buffer. It is expected that the production capacity of the machines and the whole process plant should be high when operating with buffer storage. This expectation was clearly demonstrated by the two models except for the milling and sieving machine which appears otherwise in the other model used for comparison. Similarly, the time utilized by the machines in the process plant and by the process plant as a whole is expected to increase when operating with buffer storage. The two models demonstrated this fact by showing a significant difference in the utilization time obtained from the evaluation process.

Table 3. Results for production rates and capacities of machines in the *Poundo* yam process plant

S/N	Machines	Production Rate (*kg/hr*)		Machine's output Capacity (*kg*)		Time Utilized per batch (*hr*)	
		No Buffer	Imaginary Buffer added	No Buffer	Imaginary Buffer added	No Buffer	Imaginary Buffer added
1	Washing machine	200	200	700.00	2100	3.50	10.50
2	Peeling and Slicing Machine	240	240	720.00	2160	3.00	9.00
3	Parboiling Machine	234	234	701.00	2103	3.00	9.00
4	Conveyor	1665	1664	699.20	2097	0.42	1.26
5	Drying Machine	284	284	851.18	2553	3.00	9.00
6	Milling Machine	3259	3259	814.75	2444	0.25	0.75
7	Sieving Machine	2035	2035	752.93	2259	0.37	1.11
	Process Plant	51.8	76	701.04	2103	13.53	27.6

Table 4. Comparison of the present study with another model using the *Poundo* yam process plant as a case study

S/N	Machines	Models for Comparison	Production Rate (*kg/hr*)		Machine's output Capacity (*kg*)		Time Utilized per batch (*hr*)	
			No Buffer	Imaginary Buffer added	No Buffer	Imaginary Buffer added	No Buffer	Imaginary Buffer added
1	Washing machine	Present Study	200	200	700.00	2100	3.50	10.50
		Another model	76.10	130.60	214.06	1880.64	2.63	16.10
2	Peeling and Slicing Machine	Present Study	240	240	720.00	2160	3.00	9.00
		Another model	86.36	127.00	242.92	1828.80	2.71	16.56
3	Parboiling Machine	Present Study	234	234	701.00	2103	3.00	9.00
		Another model	88.69	128.78	249.47	1854.43	2.63	16.12
4	Conveyor	Present Study	1665	1664	699.20	2097	0.42	1.26
		Another model	635.18	130.81	1786.67	1883.66	2.63	16.08
5	Drying Machine	Present Study	284	284	851.18	2553	3.00	9.00
		Another model	73.05	107.44	205.48	1547.14	3.20	19.57
6	Milling Machine	Present Study	3259	3259	814.75	2444	0.25	0.75
		Another model	915.76	112.24	2575.90	1616.26	3.06	18.74
7	Sieving Machine	Present Study	2035	2035	752.93	2259	0.37	1.11
		Another model	669.56	121.4	1883.38	1748.16	2.83	17.32
	Process Plant	Present Study	51.8	76	701.04	2103	13.53	27.6
		Another model	19.67	121.43	1022.55	1748.59	19.69	100.80

5. Conclusion

The development of process plants for achieving conversion of raw materials to finished goods plays a critical role in national development and technological sustainability. It is important to consider the capacity planning and time utilization alongside the development of these process plants from the conceptual stage of individual machines in the system. This is necessary because it will assist in optimizing the production from the process plant in order to meet the demand of the consumers. Capacity planning and time utilization of process plants will provide adequate information on the amount of raw material needed for production and the quantity of finished goods that can be moved into the system at a particular time. In order to achieve effective production capacity planning and time utilization of process plants, mathematical models are required. The mathematical model and framework presented in this article have been able to provide results by its application to a *Poundo* yam process plant. However, future work is still possible in the area of developing the framework into a model with user interface using the mathematical model and creating a computer aided process planning software that can be adopted by industries in order to know

the capacities of their plants. Further work is still necessary towards developing similar model for concurrent process plants since all process plants cannot be sequential in nature.

References

[1] C. S. Chen, S. Mestry, P. Damodaran and C. Wang, "The capacity planning problem in make-to-order enterprises". Mathematical and Computer Modelling. Vol. 50, No. 9, pp. 1461-1473, July 2009.

[2] S. C Graves, Manufacturing planning and control. Massachusetts institute of technology. Oxford University Press, New York, 2002 pp. 728-746, Ch 2, Section 18.5.

[3] T. A. Kletz, and P. Amyotte, Process plants. A handbook for inherently safer design, 2nd ed., CRC Press Taylor & Francis Group 6000 Broken Sound Parkway NW, Suite 300 Boca Raton, FL 33487-2742, 2010, pp. 241-250.

[4] R. Smith, Chemical Process: Design and Integration. John Wiley & Sons Ltd, The Atrium, Southern Gate, Chichester, West Sussex PO19 8SQ, England. 2005, pp. 17-57

[5] M. P. Groover. Automation, production systems, and computer-integrated manufacturing. 4th ed. Prentice Hall Press, Pearson Higher Education, Inc., Upper Saddle River, NJ 07458, 2015, pp. 36-74.

[6] S. P. Ayodeji, O. M Olabanji and M. K. Adeyeri, "Design of a Process Plant for the Production of *Poundo* yam", International Journal of Engineering, Vol. 6, No. 2, pp. 10-24, February 2012.

[7] S. Raundal, R. Badgujar, R. More and M. Nagare, "Capacity Planning Model for Manufacturing Organizations using AHP", International Journal of Engineering Research and Technology. IJERT. Vol. 5, No. 7, pp. 137-140, 2016.

[8] J. L. A. Koolen, Simple and Robust Plant Design. Design of Simple and Robust Process Plants. Singapoer, Toronto: Wiley VCH Verlag GmbH & Co. KGaA Germany 2002. pp. 23-34.

[9] S. Rajagopalan and J. M. Swaminathan, "A Coordinated Production Planning Model with Capacity Expansion and Inventory Management", Management Science INFORMS, Vol. 47, No. 11, pp. 1562–1580. November 2001.

[10] O. E. Maimon, E. Khmelnitsky, and K. Kogan, Optimal flow control in manufacturing systems: Production Planning and Scheduling. Vol. 18: Springer Science & Business Media 2013. pp. 59-77

[11] D. K. Harrison and D. J. Petty. Systems for planning and control in manufacturing. Newnes, An imprint of Elsevier Science Linacre House, Jordan Hill, Oxford OX2 8DP 225 Wildwood Avenue, Woburn MA 01801-2041 Butterworth-Heinemann, 2002, pp. 5-47.

[12] C. I Hsu and H. C Li, "Reliability evaluation and adjustment of supply chain network design with demand fluctuations", International Journal of Production Economics. Vol. 132, No. 1, pp. 131-145, 2011.

[13] J. R. Bradley and P. W. Glynn, "Managing Capacity and Inventory Jointly in Manufacturing Systems", Management Science INFORMS Vol. 48, No. 2, pp. 273–288, February 2002.

[14] C. I Hsu and H. C Li, "An integrated plant capacity and production planning model for high-tech manufacturing firms with economies of scale", International Journal of Production Economics. Vol. 118, No. 2, pp. 486-500, 2009.

[15] A. Russell, P. E. Ogle, R. Andrew and P. E. Carpenter, "Calculating the Capacity of Chemical Plants", American Institute of Chemical Engineers (AIChE), CEP Vol. 14, No. 8, pp. 59-63, August 2014.

[16] A. Dasci and V. Verter, "Evaluation of Plant focus strategies: A continuous approximation framework", Annals of Operations Research, Vol. 136, No. 1 pp. 303-327, April 2005.

[17] M. Barut and V. Sridharan, "Design and evaluation of a dynamic capacity apportionment procedure", European Journal of Operational Research. Vol. 155, No. 1, pp. 112-133, January 2004

[18] M. Kolhe, "Techno-Economic Optimum Sizing of a Stand-Alone solar Photovoltaic System", IEEE Transactions on Energy Conversion Vol. 24, No. 2, pp. 511-518, June 2009.

[19] J. M. Marvel Schaub, and G. Weckman, "Assessing the availability and allocation of production capacity in a fabrication facility through simulation modeling: a case study", International Journal of Industrial Engineering: Theory, Applications and Practice. Vol. 15, No. 2, pp. 166-175, 2008.

[20] O. M. Olabanji, Design of a Process Plant for the Prodution of Poundo Yam: A Thesis Submitted for the Award of Master of Engineering in Mechanical Engineering Department. Federal University of Technology Akure Ondo State Nigeria, 2012. pp. 163-167.

[21] M. O. Oke, S. Awonorin, O. Oyelade, J. Olajide, G. Olaniyan, and P. Sobukola, "Some thermo-physical properties of yam cuts of two geometries", African Journal of Biotechnology. Vol. 8, No. 7, pp. 1300-1304, 2009.

[22] F. A Tetchi, A. Rolland-Sabaté, G. N. G Amani, and P. Colonna, "Molecular and physicochemical characterization of starches from yam, cocoyam, cassava, sweet potato and ginger produced in the Ivory Coast", Journal of the Science of Food and Agriculture. Vol. 87, No. 10, pp. 1906-1916, 2007.

[23] O. O. Paul, K. Claire and D. Jacques, "Effects of planting methods and tuber weights on growth and yield of yam cultivars (Dioscorea rotundata Poir.) in Gabon", International Research Journal of Agricultural Science and Soil Science. Vol. 6, No. 3, pp. 032-042, 2016

[24] S. N. Moorthy, "Physicochemical and functional properties of tropical tuber starches: a review", Starch-Stärke. Vol. 54, No. 12, pp. 559-592. December, 2002.

Finite Element Analysis of Tungsten Inert Gas Welding Temperatures on the Stress Profiles of AIS1 1020 Low Carbon Steel Plate

Owunna Ikechukwu*‡, Ikpe Aniekan E.**

*‡Department of Mechanical Engineering, University of Benin, Nigeria.

**Department of Mechanical Engineering, University of Benin, Nigeria.

(ikechukwu.owunna@uniben.edu, aniekan.ikpe@eng.uniben.edu)

‡ Corresponding Author; Owunna I., Room 142, Department of Mechanical Engineering, University of Benin, Nigeria.

Tel: +2349034983495, ikechukwu.owunna@uniben.edu

Received: 06.03.2018 Accepted: 27.04.2019

Abstract- For better understanding of the residual stress fields associated with Tungsten Inert Gas (TIG) welding, thermal analysis was carried out using Solid Works 2017 version and ESI Visual-Environment 2016 version to compute the transient temperature profile due to welding thermal loading and resulting stress field in three categories namely; von-mises stress, axial stress and thermal stress. A range of welding temperatures including 1746^{o}C, 1912^{o}C, 2100^{o}C, 2410^{o}C and 2800^{o}C were experimentally applied in the joining process of AISI 1020 low carbon steel plate of 10 mm thickness and a strain gauge indicator was used to measure the thermal stresses induced in the steel plate which the average was recorded as 38,200MPa. The experimental parameters and conditions were applied in finite element simulation of the same plate dimension, and average von-mises stress of 37,508 MPa, average axial stress of 30,732 MPa and average thermal stress of 20,101 MPa was obtained. However, it was observed that the higher the welding temperature, the higher the stresses induced in the welding material. Hence, temperature for TIG welding process should be regulated at its optimum to avoid fatigue acceleration, stress propagation, early crack nucleation and possible fracture on the welded component which may limit the longevity and performance of such component in its service condition.

Keywords: TIG Welding, Induced stresses, Welding Temperature, Mild Steel, Finite Element Analysis.

1. Introduction

Welding is a process that involves joining two or more materials together, usually by melting the specimens into one piece and subsequent solidification of the melted parts [1]. Arc welding is divided into four (4) major processes such as Shielded Metal Arc Welding (SMAW) also known as Manual Metal Arc Welding, Gas Metal Arc Welding (GMAW) also known as Metal Inert Gas or Active Gas Welding (MIG/MAG), Flux Core Arc Welding (FCAW) and Gas Tungsten Arc Welding or Tungsten Inert Gas (TIG) which is the centre of focus in this paper [2, 3].

Due to the high temperature and heat distribution on the material in the Heat Affected Zone (HAZ), phase transformation in the melting zone as well as rapid cooling and solidification during TIG welding process, residual stresses and possible distortions are induced in the welded material as a result of thermal effects in the welding sequence [4, 5]. According to Kamble and Rao [6], heat distribution around the weldment usually can alter the chemical and mechanical properties which depends upon the chemical composition of the welded metal. Two methods are generally used in determining residual stresses, namely; experimental method and computer-based simulations method. Experimental methods is known to exist in two forms such as destructive and non-destructive methods of which diffraction methods are examples of non-destructive method [7].

In recent times, application of finite element analysis (FEA) in welding processes through computer-based simulation tools have proven to be more efficient and time saving, providing accurate results depending on the input data and significant reduction in simulation cost over experimental methods [8, 9]. Perhaps of even greater importance, is that computer-based simulations allow the user to better visualize the complex cause and effect relationship between the various welding parameters and the residual stresses induced on the weldment [10]. The application of welding operation on a material generally causes high tensile stresses, yield stresses, as well as compressive stresses in the welded metal. During service condition of the material, the thermally induced stresses on the weldment transforms to residual stresses which may result in premature failure of the welded components by causing fatigue acceleration, stress propagation, early crack nucleation and possible fracture [11].

However, residual stresses due to welding defects are trapped within the components microstructure which gradually accelerates, thereby, hampering the performance and longevity of such material in service condition. This implies that when an area of a welded component is under compressive residual stress, the neighbouring area equally suffers the effects of tensile residual stresses trapped within the weldment [12]. Although some components may not fail due to residual stresses, they can contribute immensely to stresses from external loads acting on such components. Hence, residual stresses usually tend to lessen the strength of the welded component in service condition [13]. Since welding residual stresses are primarily the result of volume changes during solidification, the stresses can be expressed in terms of three principal stresses (acting on a flat plate); axial stress, thermal stress and von-mises stress, which are the major areas of focus in this paper.

2. Materials and Methods

Two low carbon steel materials of 10mm thickness 50 mm x 35 mm (length x width) each were prepared for welding. Abrasive material (sand paper) was used to smoothen the entire material to eliminate all possible coatings, corrosion or rust that may have accumulated on the material. Prior to welding, surface of the samples to be welded were chemically cleaned with acetone to eliminate surface contamination and welding was applied on the flat plates using the conditions in Table 1. The weld pole as a result of heat application on the fusion zone is shown in Fig 1.

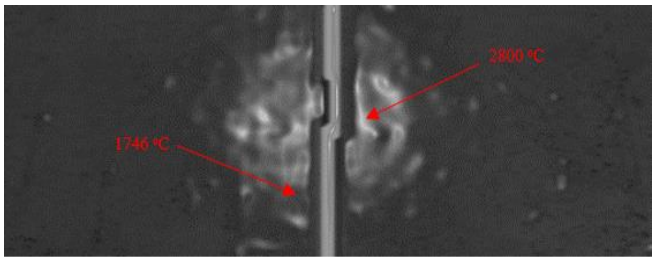

Fig. 1. Weld Pole of the Fusion Zone at Minimum and Maximum Temperature.

Table 1. Welding conditions applied in the TIG welding process

Tungsten Inert Gas	DCEN-Current	Welding Speed	Shielding Gas	Welding Power	Arc Voltage	Gas Flow Rate	Filler Rod Diameter
2.0L/min	130 A	0.18m/min	Pure argon	Alternating current (AC)	20V	20cfh	3/32

The welding runs were varied for different temperatures including 1746ºC, 1912ºC, 2100ºC, 2410ºC and 2800ºC respectively as presented in Fig 2. As shown in Fig 3, P3 strain indicator was used to measure the residual stresses induced in the steel plate which the average was recorded as 38,200 MPa.

Fig. 2. Welded Samples showing Welding Temperatures

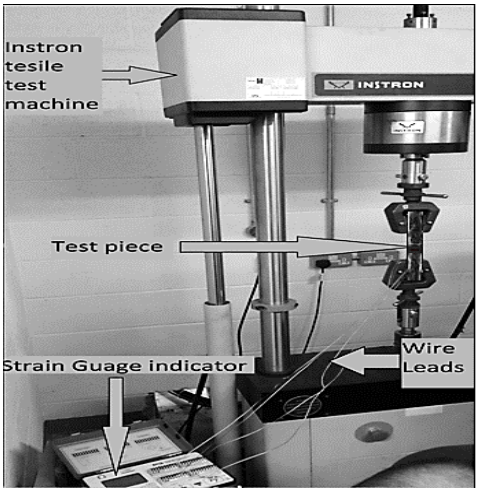

Fig. 3. Experimental Set-up showing the strain measurement

Using the available M-bond adhesive, rosette strain gauge was carefully and firmly applied at the back surface of the fusion zone on the test piece. Wire leads were soldered onto the nine terminals of the strain gauge rosette .This was carefully done

so as not to damage the strain gauge rosette. The stress values were obtained by multiplying the measured strain gauge values by the Young's modulus. However, visualization of thermally induced stress distributions on the material after the welding experimentation was complex. Considering the aforementioned welding parameters, computer–based simulations was conducted using Finite Element Analysis (FEA) to determine residual stress distribution and visualization across the material.

The FEA was carried out in two steps. A non-linear transient thermal analysis was initially conducted to obtain the global temperature profile generated during the welding process. Stress analysis was then developed with the temperatures obtained from the thermal analysis used as loading to the stress model. The FEA tool used to determine the von-mises stress was Solid Works 2017 version but the axial and thermal stresses were determined using ESI Visual-Environment. This is because Solid Works could only provide visuals of stress distribution on the welded parts, whereas, ESI Visual-Environment provided visuals of thermally induced stress distribution across the entire surface of the welded steel plate. Figure 4 represent temperature profile of the 10 mm mild steel plate in ESI Visual-Environment. Table 2 represents mechanical properties of the mild steel plate. The 3-D finite element model of the plate took a longer mesh converging time in solid works due to the large number of nodes (108015). As an alternative, a 2-D axisymmetric model in ESI Visual-Weld was developed using quadratic meshing elements (shown in Table 3) with 1342 nodes in order to simplify the mesh converging time and computational speed.

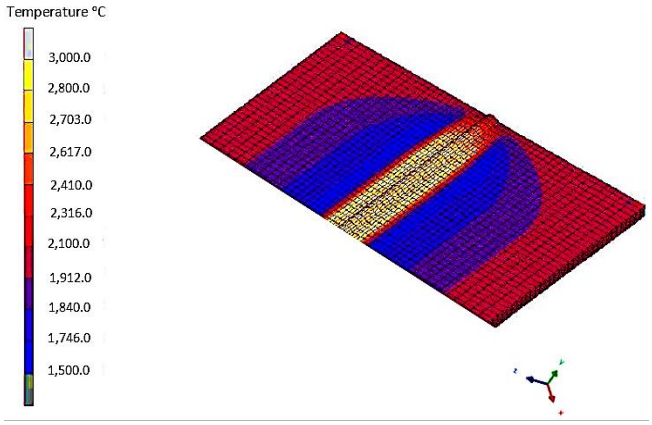

Fig. 4. Temperature Range Adopted for the FEA of 10 mm Mild Steel Plate

Table 2. Mechanical Properties of AISI 1020 Mild Steel plate

Material: AISI 1020	Properties	Model
Model type	Linear Elastic Isotropic	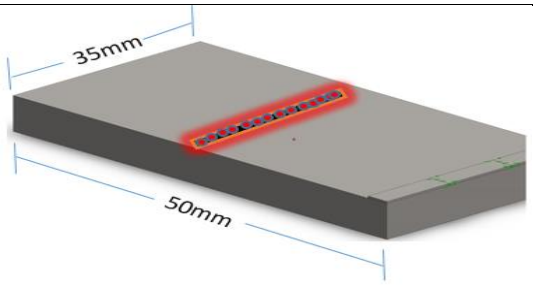
Default failure criterion	Max von Mises Stress	
Yield strength	351.571 N/mm^2	
Tensile strength	420.507 N/mm^2	
Elastic modulus	200000 N/mm^2	
Poisson's ratio	0.29	
Mass density	7900 g/cm^3	
Shear modulus	77000 N/mm^2	
Thermal expansion coefficient	1.5e-005 /Kelvin	

Table 3. Solid Works-Solid mesh and ESI Visual-Mesh Visualization

Solid Works-Solid mesh, 108015 nodes	ESI Visual-Mesh, 1342 nodes
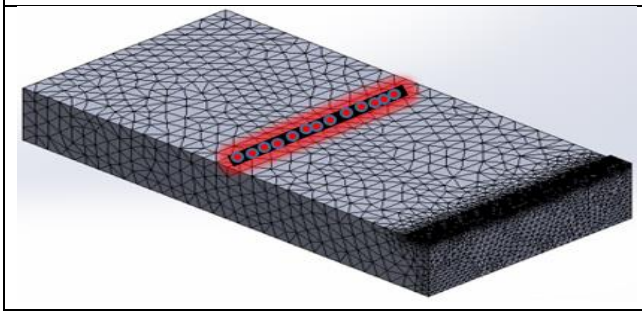	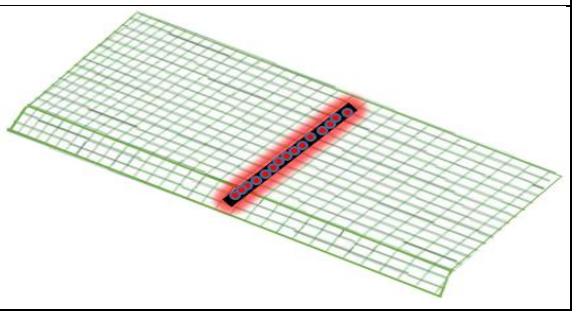

3. Thermal Analysis

During Tungsten Inert Gas welding process, the heat input per unit of time is given by equation 1;

$$\dot{Q} = \eta UI \quad (1)$$

where U is the voltage, I is the current and η is the arc efficiency.

Heat transfer in welding process is a non-linear condition due to the dependence of the material's thermos-physical properties on temperature. However, residual stresses and distortions are produced as a result of heterogeneous welding temperature caused by localized heat input during the welding

process. In this case, tungsten electrode is the heat source in which the state of heat transfer is given by equation 2.

$$\rho c \frac{\partial T}{\partial t} = \frac{\partial}{\partial x}\left(k\frac{\partial T}{\partial x}\right) + \frac{\partial}{\partial y}\left(k\frac{\partial T}{\partial y}\right) + \frac{\partial}{\partial z}\left(k\frac{\partial T}{\partial z}\right) + Q \quad (2)$$

Where p is the density, c is the specific heat capacity, k is the thermal conductivity coefficient and Q is the heat flux.

The heat source equation for first half of the mild steel plate is given by equation (3);

$$q(x,y,z,t) = \frac{6\sqrt{3Qf_f}}{abc_1\pi\sqrt{\pi}} e^{-3\left(\frac{x^2}{a^2}+\frac{y^2}{b^2}+\frac{(z-vt)^2}{c_1^2}\right)} \quad (3)$$

The heat source equation for the second half of the mild steel plate is given by equation (4);

$$q(x,y,z,t) = \frac{6\sqrt{3Qf_r}}{abc_2\pi\sqrt{\pi}} e^{-3\left(\frac{x^2}{a^2}+\frac{y^2}{b^2}+\frac{(z-vt)^2}{c_2^2}\right)} \quad (4)$$

Where q is the total heat source, v is the welding speed f_f and f_r are the energy fraction of the heat source, a, b, and c is the half axle in different directions, t is the thickness of the plate.

Heat losses on the workpiece surfaces by convection, q_c, and radiation, q_r, are introduced as boundary conditions, given by equation (5) and (6) respectively [14].

$$q_c = h(T - T_\infty) \quad (5)$$

$$q_r = \delta S\,(T^4 - T_\infty^4) \quad (6)$$

Where h and is the convention coefficient, T_∞ is the temperature of the surrounding fluid, δ is the Stefan-Boltzmann constant, S is the radiation area.

While modelling the plastic behaviour of a flat plate, it is important to define the elastic domain, which is usually based on the von Mises criterion derived from equation (7).

$$f = \sigma_v M - \sigma_y < 0 \quad (7)$$

Where f is the yielding function, σ_y is the material's yield stress and $\sigma_v M$ is the von Mises equivalent stress, given by equation 8 respectively [15].

$$\sigma_v M = \left[\frac{(\sigma_1-\sigma_2)^2+(\sigma_2-\sigma_3)^2+(\sigma_3-\sigma_1)^2}{2}\right]^{\frac{1}{2}} \quad (8)$$

Where σ_1, σ_2 and σ_3 are the principal stresses. According to the von Mises criterion, plastic strains will be developed when the condition in equation (7) is met.

In a typical welding process, there is heat source that provide the arc energy required for the operation, and this can cause localized increase in thermally induced stress as a result of the high temperature from the arc. To simulate the arc heating effect on the welded material, the equivalent heat input can be assumed as the combination of both the surface flux and body flux [16]. The surface flux qs and body flux qb are generally expressed as Gaussian distribution given by equation (9) and (10);

$$q_s = \frac{3Q_s}{\pi ac} exp\left\{\frac{3x^2}{a^2} - \frac{3z^2}{c^2}\right\} \quad (9)$$

$$q_b = \frac{6\sqrt{3Q_b}}{abc\pi\sqrt{\pi}} exp\left\{-\frac{3x^2}{a^2} - \frac{3y^2}{b^2}\,\frac{3z^2}{c^2}\right\} \quad (10)$$

Where a, b, and c are the semi-characteristic arc dimensions in x, y, direction.

4. Results

Table 4 represents the work flow sensitivity sensors which is a platform in solid works simulation that allows the sensor to be used in any plot using probe tool which can equally probe the simulation results at various scenarios for accuracy. Table 5 extracted from the solid works transient analysis represents the reaction forces (N) at different welding Temperature (°C). In addition, the stress results obtained from different welding temperatures is presented in Table 6, while the plot of stress results obtained from different welding temperature intervals is indicated in Fig. 5, respectively. However, the stress distribution across the two welded metals were somewhat similar and followed almost the same distribution trend. Therefore, the stress results presented in this section are only shown for one half of the welded mild steel plates at various welding temperature as shown in Figs. 6-20. For better visualization of the axial and thermally induced stress propagation and distribution across one half of the welded metal particularly at the surface, the same mild steel plate was also simulated in ESI Visual-Environment.

Table 4. Workflow Sensitive Sensors at different Welding Temperature

Points	Locations (mm)	Normal X	Normal Y	Normal Z	Shear XY	Shear XZ	Shear YZ
Workflow Sensitive Sensors at 1746°C (Stress Components - N/mm^2 (MPa))							
1	-5.2122, -15.3915, 14.6747	-12.72	643.50	-3.97	27.70	-3.53	3.90
2	-5.2122, -21.3290, 14.6747	-0.15	-1.34	-6.04	-0.16	-1.38	3.79
Workflow Sensitive Sensors at 1912°C (Stress Components - N/mm^2 (MPa))							
1	-5.2122, -15.3915, 14.6747	-10.05	599.19	-3.19	26.51	-2.86	4.93
2	-5.2122, -21.3290, 14.6747	-0.26	-1.28	-5.38	-0.22	-1.28	3.34
Workflow Sensitive Sensors at 2100°C (Stress Components - N/mm^2 (MPa))							
1	-5.2122, -15.3915, 14.6747	-17.57	915.29	-5.59	40.32	-4.82	5.67
2	-5.2122, -21.3290, 14.6747	-0.08	-2.07	-8.25	-0.26	-1.38	5.47
Workflow Sensitive Sensors at 2410°C (Stress Components - N/mm^2 (MPa))							
1	-5.2122, -15.3915, 14.6747	-16.73	989.23	-5.65	43.99	-4.63	7.73

2	-5.2122, -21.3290, 14.6747	-0.07	-2.26	-8.54	-0.33	-1.38	5.70
Workflow Sensitive Sensors at 2800ºC (Stress Components - N/mm^2 (MPa))							
1	-5.2122, -15.3915, 14.6747	-21.63	1303.54	-7.38	58.77	-5.94	10.35
2	-5.2122, -21.3290, 14.6747	-0.01	-3.16	-11.07	-0.45	-1.38	7.56

Table 5. Reaction Forces (N) at different welding Temperature (ºC)

Selection set	Welding Temperature (ºC)	Sum X	Sum Y	Sum Z	Resultant
Entire Model	1746	0.0576439	1.39219	0.0337265	1.39379
	1912	0.039957	1.34291	-0.0314658	1.34387
	2100	-0.0282955	1.41269	0.0461736	1.41373
	2410	-0.0388947	1.40332	0.0240045	1.40406
	2800	0.0572472	1.43699	-0.0527453	1.4391

Table 6. Stress results obtained from different Welding Temperatures

Welding Runs	Welding Temperature (ºC)	Max Experimental Thermal Stress (N/mm^2)	Max Von-mises Stress (N/mm^2)	Max Axial Stress (N/mm^2)	Max Thermal Stress (N/mm^2)
1	1,746	25,450	24,352.555	21,973.00	11,613.00
2	1,912	26,730	25,806.361	24,961.00	13,523.00
3	2,100	36,060	35,471.488	30,834.00	18,720.00
4	2,410	43,490	43,681.516	35,387.00	25,790.00
5	2,800	59,270	58,229.234	40,507.00	30,863.00
Average	2,194	38,200	37,508.2	30,732	20101.8

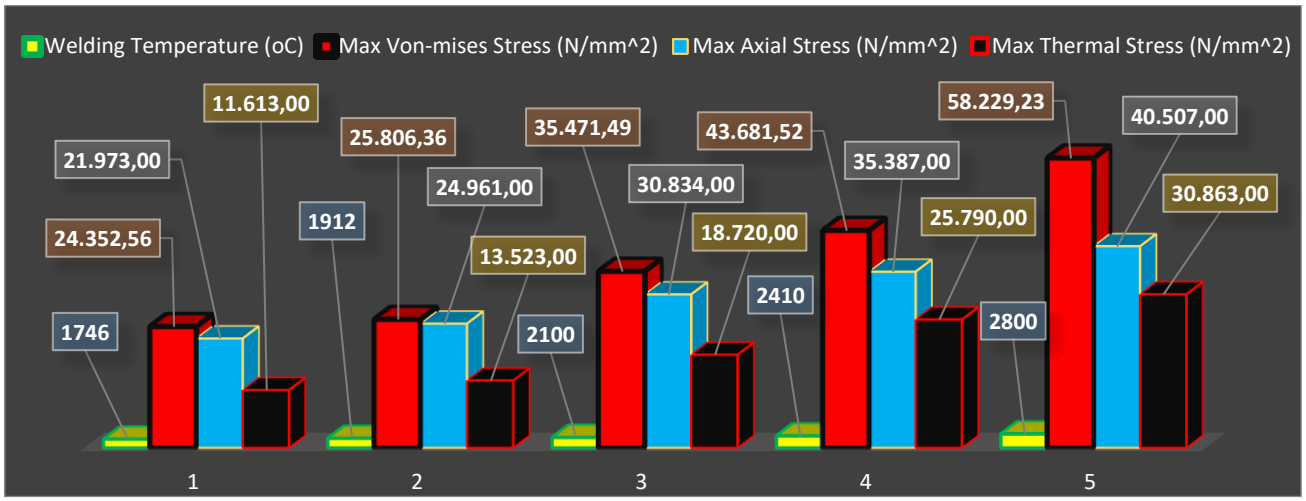

Fig. 5. Plot of Stress results obtained from different Welding Temperature Intervals

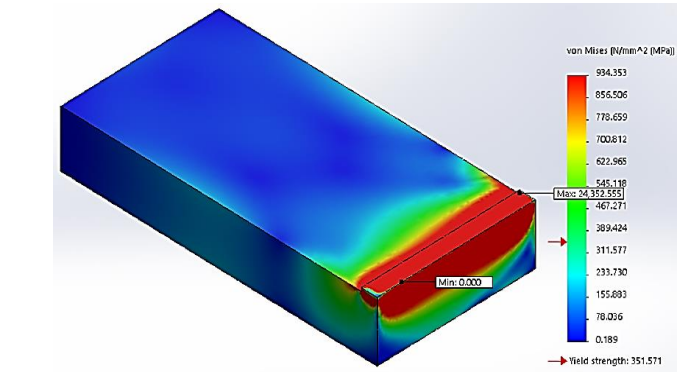

Fig. 6. Von-mises stress distribution Profile from solid Works at 1746ºC

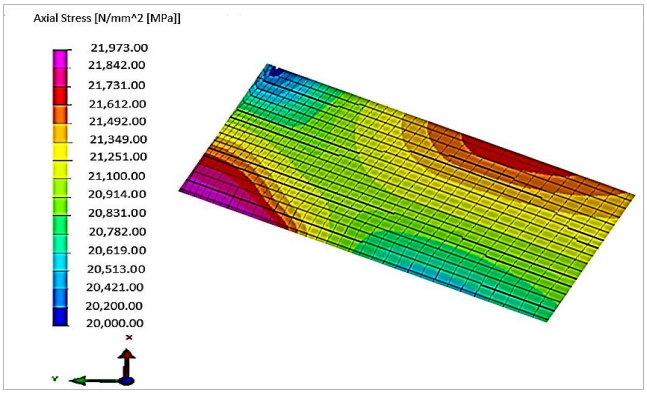

Fig. 7. Axial stress distribution Profile from ESI-Visual at 1746ºC

The thermally induced stresses in the fusion zone of the welded metal may be due to the welding parameters. This has been indicated in several studies carried out in recent times. For example, Owunna and Ikpe (2018) [17] reported that the hardness property of a welded metal can be affected by the Welding voltage, while the strength of the weld joints can improve with decreasing welding voltage but prone to thermal stress at increasing welding current. The higher welding amperage in effect can result in undercut due to welding operations conducted with relatively high amperage or relatively long arc length which would leave a groove in the base metal along either sides of the bead, thereby, causing residual stress build-up and reduction in the strength of the weldment [18]. It was observed in similar studies that excessively high welding temperature and voltage can result in a wider bead that would subject the weldment to thermal stress cracking, increased undercut, increased side wall fusion defects and difficulty in slag removal while amperage set too low may result in a narrow and erratic beads that would affect fusion of the metal plates [19].

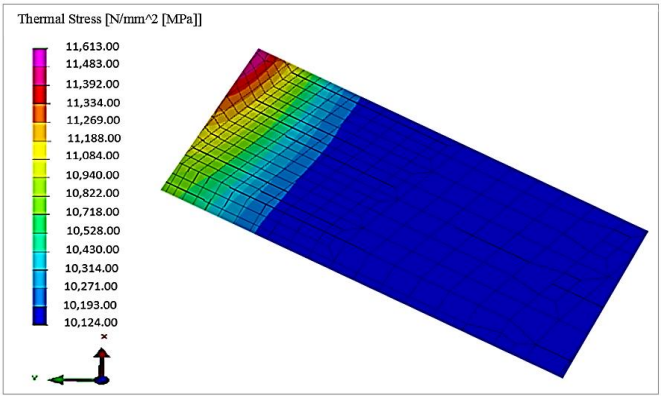

Fig. 8. Thermal induced stress distribution Profile from ESI-Visual at 1746ºC

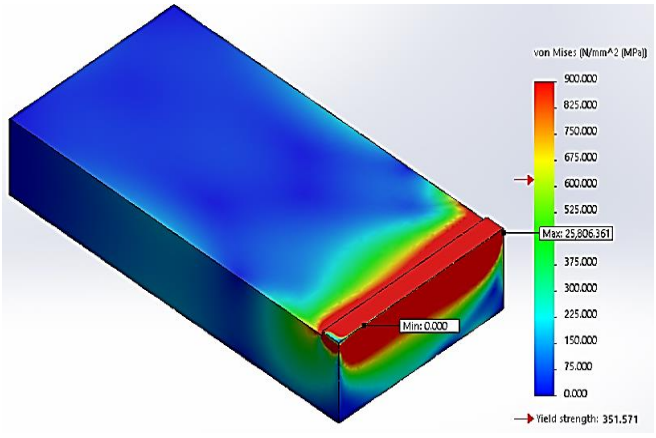

Fig. 9. Von-mises Stress Distribution Profile from Solid Works at 1912ºC

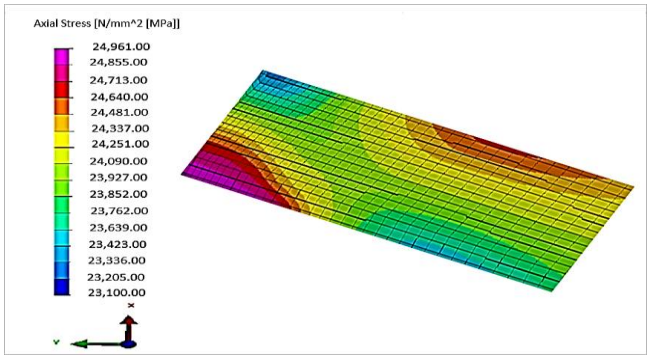

Fig. 10. Axial stress distribution Profile from ESI-Visual at 1912ºC

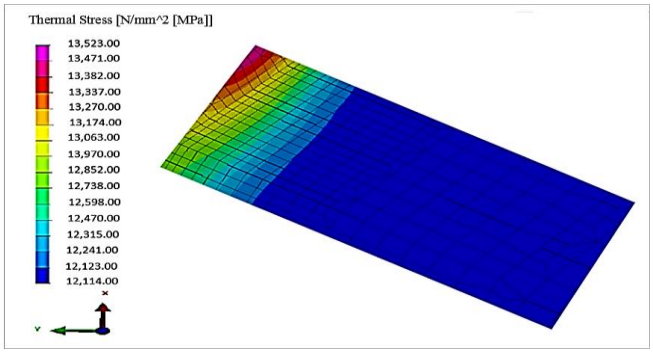

Fig. 11. Thermal stress distribution Profile from ESI-Visual at 1912ºC

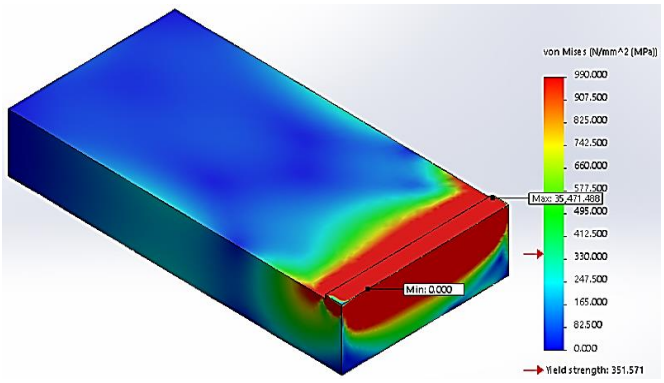

Fig. 12. Von-mises Stress Distribution Profile from Solid Works at 2100ºC

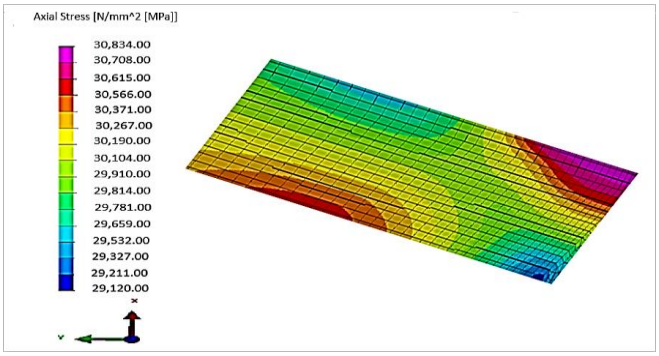

Fig. 13. Axial stress distribution Profile from ESI-Visual at 2100ºC

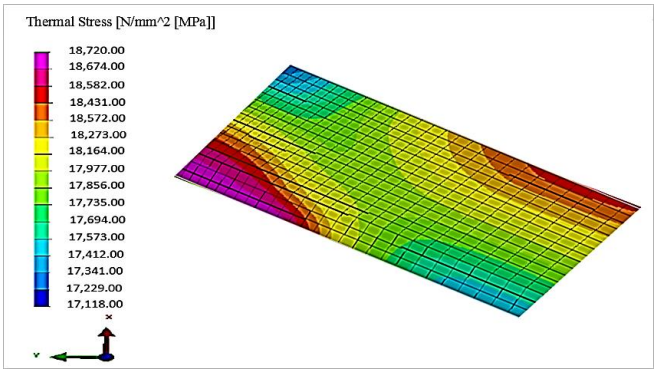

Fig. 14. Thermal stress distribution Profile from ESI-Visual at 2100°C

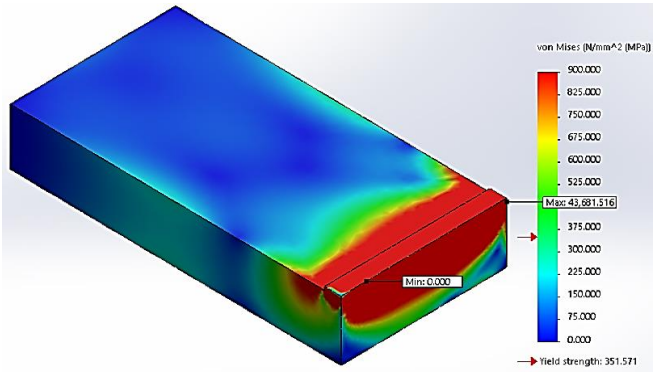

Fig. 15. Von-mises Stress Distribution Profile from Solid Works at 2410°C

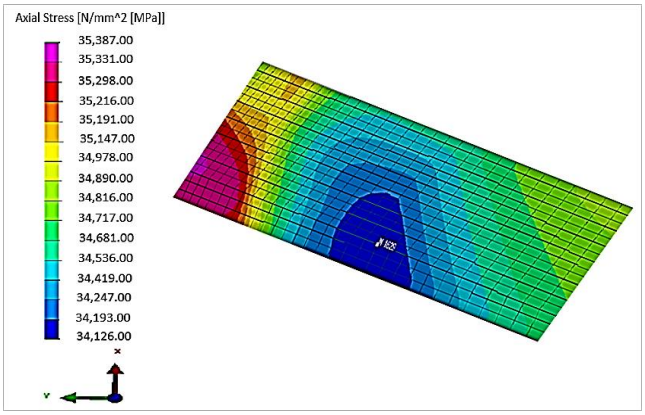

Fig. 16. Axial stress distribution Profile from ESI-Visual at 2410°C

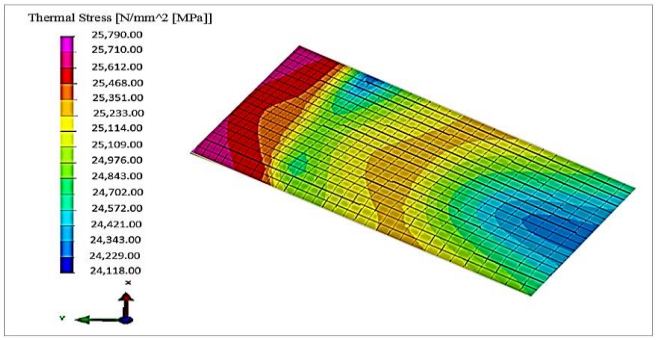

Fig. 17. Thermal stress distribution Profile from ESI-Visual at 2410°C

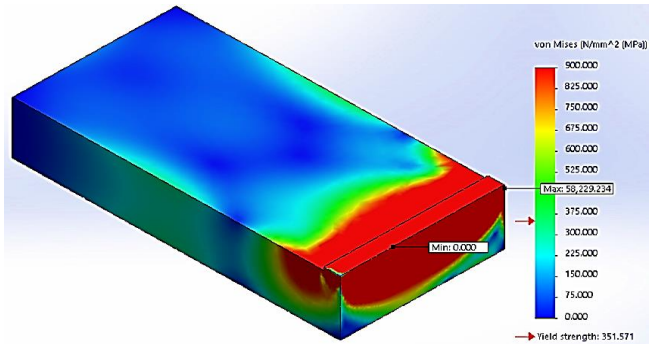

Fig. 18. Von-mises Stress Distribution Profile from Solid Works at 2800°C

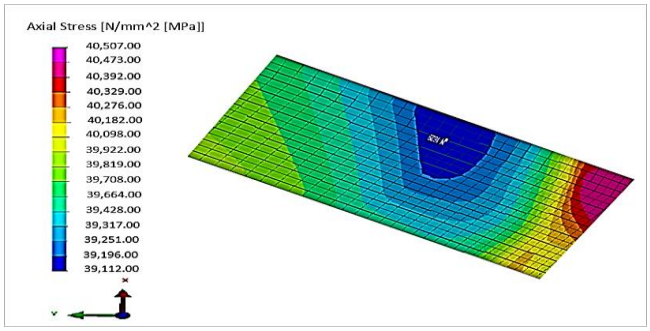

Fig. 19. Axial stress distribution Profile from ESI-Visual at 2800°C

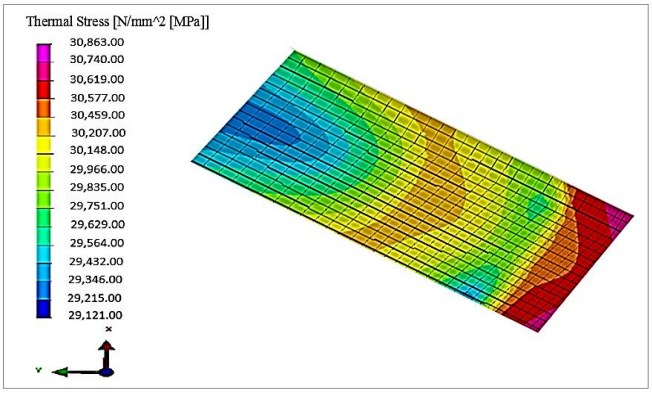

Fig. 20. Thermal stress distribution Profile from ESI-Visual at 2800°C

Table 6 best exemplify this phenomenon where welding temperature of 1746°C yielded maximum von-mises stress of 24,352.555 MPa, maximum axial stress (tensile stress) of 21,973.00 MPa and maximum thermal stress of 11,613.00 MPa. Furthermore, increasing the welding temperature to 1912°C led to increased maximum von-mises stress of 25,806.361 MPa, maximum axial stress of 24,961.00 MPa and maximum thermal stress of 13,523.00 MPa while further increase in the welding temperature to 2100°C produced increasing maximum von-mises stress of 35,471.488 MPa, maximum axial stress of 30,834.00 MPa and maximum thermal stress of 18,720.00 MPa respectively. In addition, the last two welding temperature was increased to 2410°C and 2800°C and maximum von-mises stress of 43,681.516 MPa, maximum axial stress of 35,387.00 MPa, maximum thermal

stress of 25,790.00 MPa and maximum von-mises stress of 58,229.234 MPa, maximum axial stress of 40,507.00 MPa, maximum thermal stress of 30,863.00 MPa. The Solid Works models shown in Figs. 6, 9, 12, 15 and 18 were simulated to determine the von-mises stress but visuals of the stress distributed across the welded material showed that the stress concentrated mainly on the weldment and edges of the welded metal, whereas, visuals of the stress distribution on the surface of the metal plate were more elaborate with ESI Visual-Environment as shown in Fig 7, 8, 10, 11, 13, 14, 16, 17, 19 and 20 respectively.

The high temperature around the welding pool and the existing heat dissipation through the plate and from the surface cause a severe temperature gradient across the welded material and possible stresses that may alter the microstructure of the material, as the HAZ extends from the welded joint. According to Owunna and Ikpe [20], heat distribution around the weldment usually alters the chemical and mechanical properties which depends upon the chemical composition of the bead and its geometry. This is in agreement with the studies on weld bead penetration in Tungsten TIG welding of AISI 1020 low carbon steel plate, where it was observed that higher the temperature distribution across the fusion zone, the wider the Heat Affected Zones (HAZs) which are indications of phase transformations and alterations in mechanical properties of the welded metal which may lead to induced residual stresses if the welding parameters particularly the amperage is not controlled adequately [21].

As shown in Fig. 5, the induced stresses were computed in three categories namely; Von-mises yield criterion (also referred to as maximum distortion energy criterion) which is part of plasticity theory for ductile materials, suggesting that the yielding effect of a given material commences when the second deviatoric stress invariant reaches a critical value. In other words, von-mises stress is a value that can be used to determine the rate of yield or fracture in a material. The second category of stress considered in this study is tensile stress which tends to alter the length of a body by causing the welded material to elongate in the direction of the applied welding force, whereas the third category of stress considered in this study is the thermal stress which is induced in the welded material due to temperature variation, thermal expansion or contraction and thermal shocks, and can result in fracture or plastic deformation depending on the heat constraint and other variables such as thermal conductivity of the material.

Generally, thermal stress is a constraint that significantly affect a material subjected to high temperature welding condition, and it is highly dependent on the thermal expansion coefficient of the welded material. In other words, the higher the temperature variation, the higher the stresses induced in the welded material as tabulated earlier in Table 6. This correlates with the investigation carried out by Tarak [10] on residual stresses due to circumferential girth welding of austenitic stainless steel pipes.

5. Conclusion

Based on the objective of this work, a Finite Element Method based on transient thermal elastic plastic model was developed and the effects of TIG welding cycle on AISI 1020 low carbon steel plate of 10 mm thickness was examined. The material parameters for the AISI 1020 mild steel were assumed to be temperature dependent, while other constraints such as distributed arc heat input, heat loss, welding speed, shielding gas, welding power, arc voltage, gas flow rate were considered in the model. From the stresses obtained from the thermal transient analysis of TIG welding process of mild steel in this study, it has been observed that temperature gradient in terms of heat input plays a major role in welding in which lower heat input affects the quality of the welded joints. Therefore, optimum heat input is ideal for joining of two or more metals together. In addition, comparing the results obtained for each of the three average stress (maximum von-mises stress, maximum axial stress and maximum thermal stress) categories and the maximum average stress result measured with a strain gauge indicator during the experimental exercise showed relatively less difference for von-mises stress (692 Mpa), a higher difference in terms of axial stress (7,468 MPa) and relatively high difference in thermal stress (18,099 MPa), thus, indicating that thermal induced stress which is a function of high temperature and heat input during welding operation must be prerequisite for consideration prior to commencement of any welding operation.

References

[1] K. Y. Benyounis and A. G. Olabi, “Optimization of Different Welding Process Using Statistical and Numerical Approaches: A Reference Guide”, Advanced Engineering Software, Vol. 39, pp. 483-496, 2008.

[2] K. Weman, Welding processes handbook. New York: CRC Press LLC. ISBN 0849317738, 2003.

[3] A. E. Ikpe, I. Owunna and I. Ememobong, “Effects of Arc Voltage and Welding Current on the Arc Length of Tungsten Inert Gas Welding (TIG)” International Journal of Engineering Technologies-IJET, Vol. 3, Issue 4, pp. 213-221, 2017.

[4] R. K. Jain, Production Technology, Khanna Publishers, New Delhi pp. 344-346, 2001.

[5] N. Sura, and V. Mittal, “Experimental Study on Effects of Process Parameters on HAZ of Plain Carbon Steel Using GMAW”, International Journal of Latest Research in Science and Technology, Vol. 4, Issue 2, pp. 167-170, 2015.

[6] A. G. Kamble and R. V. Rao, “Experimental Investigation on the Effects of Process Parameters of GMAW and Transient Thermal Analysis of AlSl 321 Steel”, Advances in Manufacturing, Vol. 1 Issue 4, pp. 362-377, 2013.

[7] E. Lima, J. Wagener, A. Pyzalla and T. Buslaps, "Investigations on Residual Stresses in Friction Stir

Welds", in 3nd International Symposium on Friction Stir Welding, Kobe, Japan, 2001.

[8] M. V. Dalvi, A. S. More, S. P. Joshi and V. M. Junnarkar, "Determination of Failure Strength of Flat Plate Weld Joint Using Finite Element Analysis", International Journal of Scientific & Engineering Research, Vol. 3, Issue 12, pp. 302-306, 2012.

[9] C. S. Baviskar, R. M. Tayade and V. G. Patil, "Determination of Failure Strength of Curved Plate Weld Joint Using Finite Element Analysis", International Journal of Mechanical Engineering and Robotic Research Vol. 1 Issue 3, 22-30, 2012.

[10] F. Tarak, Residual Stresses Due to Circumferential Girth Welding of Austenitic Stainless Steel Pipes, Theses and Dissertations, Paper 1649, Lehigh University, 2013.

[11] M. Law, H. Prask, V. Luzin and T. Gnaeupel-Harold, Residual stress measurements in coil, linepipe and girth welded pipe, Elsevier Science Ltd., Menai, 2006.

[12] G. Mi, C. Li, Z. Gao, D. Zhao and J. Niu, "Finite Element Analysis of Welding Residual Stress of Aluminium Plates Under Different Butt Joint Parameters" Engineering Review, Vol. 34, Issue 3, 161-166, 2014.

[13] L. Karlsson, Residual Stresses Due to Welding of a Nozzle to a Pressure Vessel, Lund University, Lund, 2005.

[14] T. D. Eastop and A. McConkey, Applied Thermodynamics for Engineering Technologist, Fourth Edition, Pearson Education Ltd. ISBN: 8178085577, 2004.

[15] R. G. Budynas and J. K. Nisbett, Shigley's Mechanical Engineering Design, 9th Edition, McGraw-Hill Higher Education: New York, 2011.

[16] B. I. Bang, Y. P. Son, K. H. Oh, Y. P. Kim and W. S. Kim, "Numerical simulation of sleeve repair welding of in-service gas pipelines", Welding Journal, Vol. 81, pp. 273-282, 2002.

[17] I. B. Owunna, and A. E. Ikpe "Effects of Parametric Variations on Bead Width of Gas Tungsten Arc Welding of AISI 1020 Low Carbon Steel Plate", International Journal of Engineering Technology and Sciences", Vol. 5, Issue 3, pp. 1-13, 2018.

[18] I. Owunna, A. E. Ikpe and J. I. Achebo, "Temperature and Time Dependent Analysis of Tungsten Inert Gas Welding of Low Carbon Steel Plate using Goldak Model Heat Source", Journal of Applied Science and Environmental Management, Vol. 22, Issue 11, pp. 1719-1725, 2018.

[19] Ikpe A. E. and I. Owunna, "Optimization of TIG Welding Input Variables for AISI 1020 Low Carbon Steel Plate Using Response Surface Methodology", International Journal of Engineering Science and Application, Vol. 2, Issue 3, pp. 113-122, 2018.

[20] I. B. Owunna and A. E. Ikpe, "Modelling and Prediction of the Mechanical Properties of TIG Welded Joint for AISI 4130 Low Carbon Steel Plates Using Artificial Neural Network (ANN) Approach", Nigerian Journal of Technology, Vol. 38, Issue 1, pp. 117-126, 2019.

[21] I. Owunna, A. E. Ikpe and J. I. Achebo, "3D Finite Element Modelling of Weld Bead Penetration in Tungsten Inert Gas (TIG) Welding of AISI 1020 Low Carbon Steel Plate", European Mechanical Science, Vol. 2, Issue 3, pp. 96-105, 2018.

Controlling A Robotic Arm Using Hand Recognition Software

Ali Cetinkaya*‡, Onur Ozturk**, Ali Okatan***

*Technology Transfer Office, Istanbul Gelisim University, Avcılar, Istanbul, Turkey.

**School of Management, Faculty of Engineering, University College London (UCL), Euston, London, UK.

***Department of Computer Engineering, Faculty of Engineering, Istanbul Gelisim University, Avcılar, Istanbul, Turkey.

(alcetinkaya@gelisim.edu.tr, onur.ozturk.16@ucl.ac.uk, aokatan@gelisim.edu.tr)

Corresponding Author: Ali Cetinkaya, Technology Transfer Office, Istanbul Gelisim University, Avcılar, Istanbul, Turkey. Tel: +90 212 422 70 00 / 7187. alcetinkaya@gelisim.edu.tr

Received: 21.09.2018 Accepted: 27.04.2019

Abstract- With the increasing need of repetitive tasks in the manufacturing industry, robotic automation is becoming a necessity. In the steel industry, workers become less efficient over time, causing interruptions during assembly. Robotic automation is capable of operating at highest efficiency therefore increasing productivity in the steel industry. The robot will be able to pick up and drop metallic object with the help of the electromagnet present on the robotic arm. The handling of the objects will be triggered by the hand gestures from the user. The image to be processed will be captured by an external camera. This robot is built as a prototype for the steel industry.

Keywords Gesture Recognition, OpenCV, Embedded System Robotic Arm Control, Embedded C.

1. Introduction

The aim of this system was to operate the robot with embedded tasks via finger recognition software coming from a video stream from the PC video output due to the reasons listen in the abstract [1]. The image recognition software was designed in OpenCV3, whereas the embedded system was designed in Arduino.

Finger recognition works by counting the empty spaces between the fingers. The finger recognition software works using convex hull algorithms and contour detection. In simpler terms, convex hull approach aims to confine a set of given points in a plane by the smallest polygon [2, 3].

OpenCV is a library designed for use in open source software and real-time image processing applications. This library, which can calculate all the moments of a polygonal and random shape, finds convexity lines through hand recognition [4, 5].

In sectors such as production, repetitive jobs are performed in most areas. There are many manpower and cost increases. An interactive design has been done by creating a robotic system to perform object recognition and operations [6].

Autonomous systems aim to control the movement of robots in robotic studies and researches. The algorithms used in such systems can make improvements by analyzing the errors that occur during the movements of the robots. These errors are calculated during the experiments on the robotic arms and in the next trials they provide the system with operational response [7].

A new algorithm for real-time and recognition is based on hand movement recognition. This algorithm is based on three main steps: hand partitioning, hand tracking and gesture recognition. Skin color, hand segmentation and monitoring based algorithm have been proposed for hand recognition. It has been investigated that it leads to good performances on the system [8].

The Kalman filter was used for the steady position of the hand movement by using convective neural networks for real-time interaction with hand movements [9]. For control of the robotic arm, control of the robotic arm is provided via the analog signals from the sensors. Wearable robotic arm is designed to simulate the natural movements of the human arm [10]. People who work in explosive and security operations are at risk and life-threatening. Therefore, we can keep the

danger away from people by the help of a robotic hand on an autonomous device [11].

Motion control can be used on heavy machines. These movements are used to control the movement of robotic arms with image processing techniques [12]. The natural hand movement recognition system is developed upon hand recognition and recognition of hand movements. Hand tracking, background cleaning, and lighting status create difficulties in motion recognition systems [13]. It is controlled by sensors and accelerometers in a system that simulates the movement of the user's arm by manual tracking. Kinect simulates the skeleton of the human body and provides its three-dimensional coordinates to its users [14].

Systems designed to work on more than one person have been designed with a finger-tipped approach to recognizing hand movements [15].

With the removal of the hand zone from the background, the data sets of the hand movements are created by detecting the palms and the fingers. With the data sets created, the accuracy of the method is controlled [16].

A robot kinematics can be examined geometrically and the position, velocity and acceleration information of all of its movement from force and torque components can be extracted [17, 18].

The robotic arm is controlled via pre-defined actions in Arduino. The four actions defined by the robotic arm are as follows: forwards arm motion, turning on the electromagnet, backwards arm motion and turning off the electromagnet. The finger count for these actions are respectively 2, 3, 4 and 5. The fingers do not have to be showed in order. For example, showing index and pinky finger would still trigger action 2.

2. System and Software Algorithm's

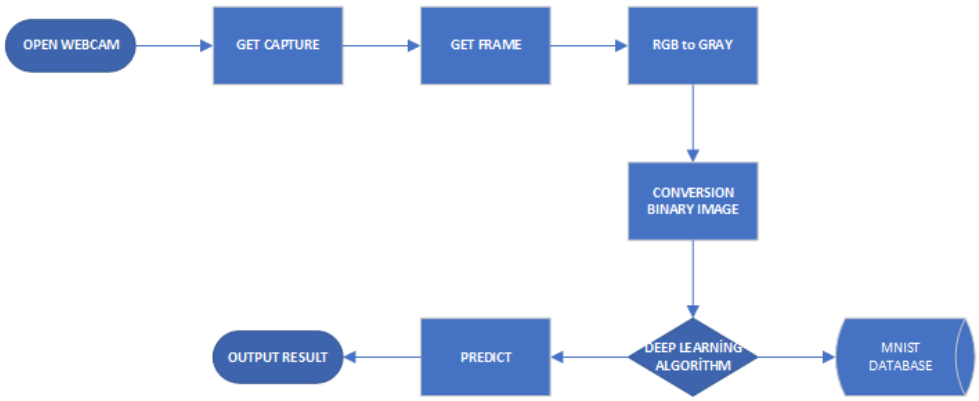

Fig. 1. Flow diagram of algorithm step.

Fig. 1 shows summaries the necessary steps in this study. In this study using the deep learning algorithm and Mnist data set consists of 3 main stages. These are: preprocessing on the image, deep learning algorithm and mnist data set.

The Arduino Mega code was produced using the Arduino IDE. Arduino is responsible for controlling the servo engines using the data received from the hand recognition software. For this purpose, the libraries used were standard to Arduino, therefore any user can duplicate the results.

Firstly, in the code, library and variable definitions were created. There are three servo definitions and three servo angle definitions.

Secondly, in the setup() section, the servos were attached to their respective pins and the initiation angles to the servos are written. The servo engines initiate at 90 degrees. There is no user input that can keep the servos at 90 degrees, therefore the once the arm stands at a 90-degree angle, the user can understand that the system has initiated. Furthermore, a three-note music is played by the system once the serial opens, to make sure that the communication pathway between the Python hand recognition software and Arduino Mega is open.

Lastly, in the loop() section, a switch case was created. This switch case operates given the user input from the Python program. According to the number of fingers received from the Python program, different cases in switch are activated, which operates the robotic arm.

The Python hand recognition software works using OpenCV and Serial Port [5]. OpenCV proves rather useful when working with computer vision and image recognition due to wide variety of supported libraries and conducted experiments. OpenCV has more than 47.000 users and more than 14 million estimated downloads. Use extends from interactive art to mine inspection, to stitch maps on the web, or to advanced robots. [5].

When the software is initiated, a video stream from the camera of the PC (or webcam, in this system) is recorded and presented on the screen. Even though the entire video stream is presented on the screen, the part of the screen which processes the information is marked with a red square. Instead of detecting the entire video stream, the red square was chosen to be area of interest due to efficiency purposes. The program works more efficiently in a smaller area. The user must present his/her hand in this square for the software to process the information. Once the hand is presented in this square, the software is responsible for counting the empty spaces between the fingers. For example, if the software is counting 3 defects, there would be 4 fingers present in the square, which would trigger an action to the servos [6, 7].

The Python code can be seen alongside the closed system can be seen in Fig. 2.

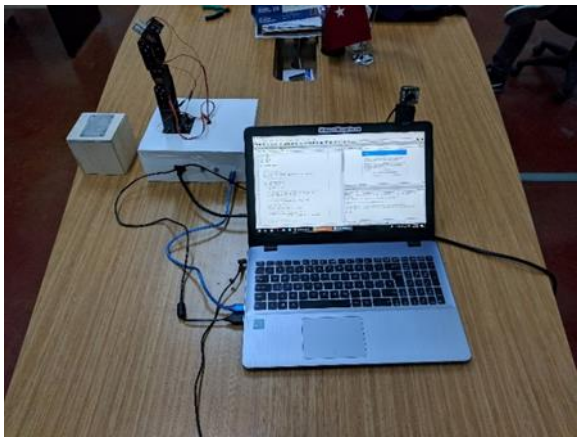

Fig. 2. Closed system along with the software.

3. Analysis Process On Image

In image processing, the thresholding method of the Otsu is used for the decision of the automatic thresholding level based on the shape of the histogram [19, 20]. The method of Otsu selects the threshold by minimizing the intra-class variation of two pixel groups separated by the thresholding operator [19, 20]. The aim is to select a point as the threshold value between two peaks representing the foreground and background pixel values [19, 20].

With the calculation below, this calculation depends on the histogram counting set [20]. Taking into account the probability $\omega 1$ on equation 1 and $\omega 1$ on equation 2;

$$\omega_0 = \sum_{i=0}^{k} Pi = \omega(k) \quad (1)$$

$$\omega_1 = \sum_{i=k+1}^{L} Pi = 1 - \omega_0(k) \quad (2)$$

Equation 3 above μ0, μ1 on Equation 4 and Equation 5 above ω (k) is calculated.

$$\mu_0 = \sum_{i=1}^{k} \frac{iPi}{\omega 0} = \frac{\mu(k)}{\omega(k)} \quad (3)$$

$$\mu_1 = \sum_{i=k+1}^{k} \frac{iPi}{\omega 1} = \frac{\mu T - \mu(k)}{1 - \omega(k)} \quad (4)$$

where

$$\omega(k) = \sum_{i-1}^{k} iPi \quad (5)$$

The average pixel value of the total image is calculated using μt equation 6.

$$\mu T = \sum_{i=1}^{L} iPi \quad (6)$$

Class variables to be used in calculations σ_0^2 ve σ_1^2 equation 7 and 8 is calculated by.

$$\sigma_0^2 = \sum_{i=1}^{k} (i - \mu 0)^2 \, pi / \omega_0 \quad (7)$$

$$\sigma_1^2 = \sum_{i=k+1}^{L} (i - \mu_1)^2 \, pi / \omega_1 \quad (8)$$

The Otsu algorithm mentions three classes significantly. These changes to the class λ, change between classes κ and total variance Ƞ with these variables are defined on equations 9, 10 and 11.

$$\lambda = \sigma_B^2 \quad (9)$$

$$\kappa = \sigma_T^2 / \sigma_W^2 \quad (10)$$

$$Ƞ = \sigma_B^2 / \sigma_T^2 \quad (11)$$

where

$$\sigma_W^2 = \omega_0 \, \sigma_0^2 + \omega_1 \, \sigma_1^2 \quad (12)$$

$$\sigma_B^2 = \omega_0 \, (\mu_0 - \mu_T)^2 + \omega_1 \, (\mu_1 - \mu_T)^2 = \omega_0 \, \omega_1 \, (\mu_1 - \mu_0)^2 \quad (13)$$

Equation 12 and 13 on σ^2 ve σ_B^2 formulas where the variables are defined are shown. Otsu states that when any of these criteria are maximized, the others are equivalent to maximizing. Equation 11 on definition Ƞ larger threshold value according to the selected equation can be re-displayed on the articles 13 σ_B^2 's is the same as maximizing.

$$\sigma_B^2(k) = \frac{[\mu T \omega(k) - \mu(k)]^2}{\omega(k)[1 - \omega(k)]} \quad (14)$$

The formula shown on Equation 14 is the most important calculation process on the Otsu algorithm. For all possible threshold values with this formula σ_B^2 calculated. And the maximum value that makes it the threshold value is selected.

The contours are described as a curve that combines all the continuous points of the same color or density along the boundary [18]. The contours are used for shape analysis and object detection and recognition [18]. The contour is the curve of two variable functions in which the function has a fixed value. A contour combines points above a certain level and an equal height [21].

Convex hull, concave polygons are traded on a defined region. The purpose is to find the smallest convex shape that surrounds the concave shape. This algorithm has been used to scan all points in the set of contour points within the system. A drawing process is performed around the contour of the hand to create a convex body by scanning all contour points [5, 21, 22].

4. Experiments

Upon completing the system, experiments were conducted in order to see the movement of the robotic arm. The system was successful when recognizing the number of fingers shown to the camera. The recognized number of fingers seen by the camera were written on the Python screen. The different results acquired from the camera image can be

seen in the pictures below. Fig. 3, 4, 5, 6 and 7 show 1, 2, 3, 4 and 5 fingers respectively.

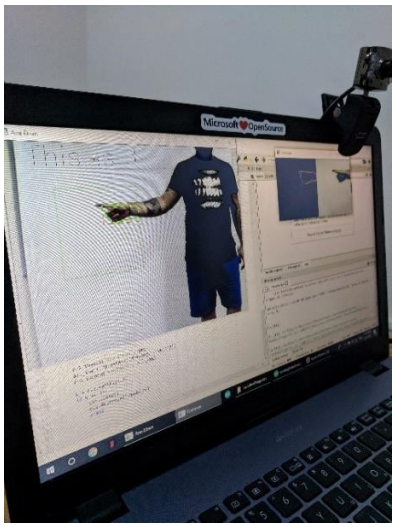

Fig. 3. Results showing 1 finger.

Fig. 4. Results showing 2 fingers.

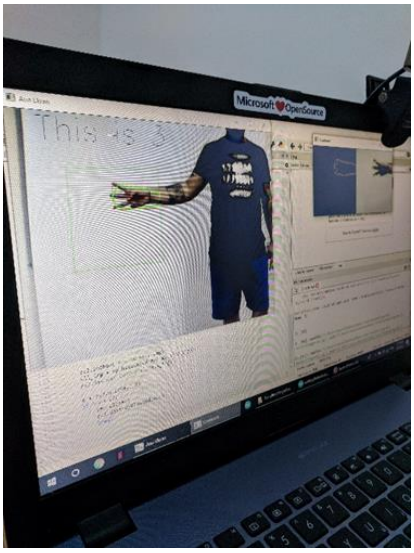

Fig. 5. Results showing 3 fingers.

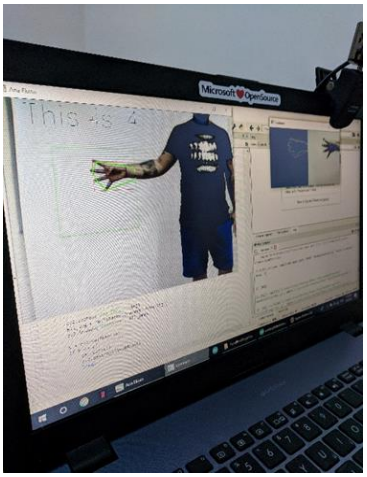

Fig. 6. Results showing 4 fingers.

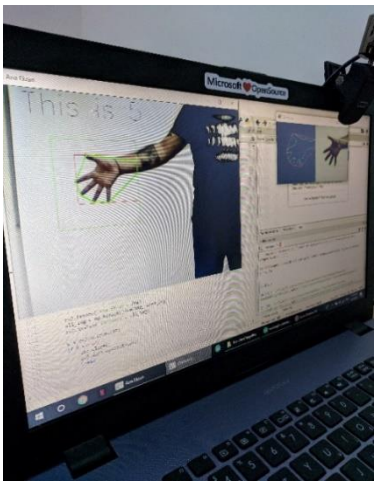

Fig. 7. Results showing 5 fingers.

During the experiments there were two potential problems that could diminish the results produced by the robot. If the background behind the red square in the software of polluted, the results were incorrect. Secondly, if the user does not leave adequate space between their fingers, the software often does not recognize the spaces between fingers. If these circumstances are satisfied, the results are successful, and the robotic arm movement is established.

5. Conclusions

As a result, as the distance between the webcam and the image increased, the hand gestures on the background could not read the software clearly, and incorrect operations were encountered. In addition, if the angle between the fingers is small, it has been seen that it defines the movement wrongly. The results are shown in Figures 3, 4, 5, 6 and 7.

6. Discussion

The aim of this study is to be able to detect finger movements of a person with instant camera images and perform defined operations on embedded systems. In the experiments, errors were detected in capturing the image depending on the distance between the background and the camera. Camera resolution is required to correct this error. The light level of the environment can be changed according to the experiment.

Acknowledgements

Many thanks to Istanbul Gelisim University and Technology Transfer Office for their support.

References

[1] E. B. Mathew, D. Khanduja, B. Sapra, B. Bhushan, Robotic arm control through human arm movement detection using potentiometers, International Conference on Recent Developments in Control, Automation and Power Engineering, 2015.

[2] B. İşçimen, H. Atasoy, Y. Kutlu, S. Yıldırım, E. Yıldırım, Smart robot arm motion using computer vision, Elektronika Ir Elektrotechnika, ISSN 1392-1215.

[3] M. A. Jayaram, H. Fleyeh, Convex hulls in image processing: a scoping review, American Journal of Intelligent Systems, 2016.

[4] OpenCV library document, https://opencv.org/

[5] Structural Analysis and Shape Descriptors, OpenCV "2.4.13.7 documentation". https://docs.opencv.org

[6] A. Dhawan, A. Bhat, S. Sharma, H. K. Kaura, Automated robot with object recognition and handling features, International Journal of Electronics and Computer Science Engineering, ISSN 2277-1956/V2N3-861-873.

[7] Abhishek Chavan, Abhishek Bhuskute, Anmol Jain, Dynamics of robotic arm, International Journal of Computer Applications (0975 – 8887), 2014.

[8] C. Manresa, J. Varona, R. Mas, F. J. Perales, ''Hand tracking and gesture recognition for human-computer interaction'', Electronic Letters on Computer Vision and Image Analysis 5(3):96-104, 2005.

[9] P. Xu, A real-time hand gesture recognition and human-computer interaction system, arXiv:1704.07296v1 [cs.CV] 24 Apr 2017.

[10] A. Soetedjo, I.K. Somawirata, A. Irawan, ''Human arm movement detection using low-cost sensors for controlling robotic arm'', Journal of Telecommunication, Electronic and Computer Engineering, e-ISSN: 2289-8131 Vol. 10 No. 2-3.

[11] A. Alam, T. Rana, M. Hashemy, An autonomous detective robotic arm, International Conference on Mechanical, Industrial and Materials Engineering 2017.

Determining the Velocity Distribution Profile of a Fluid in an Inclined Flat Surface Using the Finite Element Method and the Exact Differential Equation Method

Iredia Davis Erhunmwun*, Collins Oside**‡

*Department of Production Engineering, Faculty of Engineering, University of Benin, P.M.B. 1154, Benin City, Nigeria.

** Department of Mechanical Engineering, Faculty of Engineering, National Institute of Construction Technology, Uromi, Nigeria.

(iredia.erhunmwun@uniben.edu, osidecollins@gmail.com)

‡ I. D. Erhunmwun, Department of Production Engineering, University of Benin, P.M.B. 1154, Benin City, Nigeria, Tel: +234 807 072 8898,
Fax: +234 807 072 8898, iredia.erhunmwun@uniben.edu

Received: 27.07.2018 Accepted:25.04.2019

Abstract- An analysis has been carried out to determine the velocity profile of a fluid on an inclined plane using the Finite Element Method (FEM). The overall results from these finite elements were finally assembled to represent the velocity profile in the entire domain of the inclined plane. The results obtained from the finite element method shows that as the velocity distribution has a parabolic profile with the maximum velocity of 1109.8748m/s at open surface of the inclined plane. The fluid due to the no slip boundary condition has 0m/s at the walls of the inclined plane. Also, it was shown that the higher the angle of inclination and fluid viscosity, the lower the velocity and also the higher the fluid density, the higher the velocity. The result obtained from the FEM when compared with the result obtained from the exact differential equation method shows a strong agreement with a maximum percentage error of $2.3413x10^{-14}$.

Keywords: Finite Element Method, Inclined Plane, Incompressible Fluid, Interpolation Function, Weak Formulation

1. Introduction

Investigation of the properties of flow down an inclined plane is a subject of great theoretical and practical importance and has attracted the attention of many researchers [1-3]. Consideration has been given to a fluid constantly poured on the inclined plane from above. The fluid forms a steady stream moving downwards under the action of the gravity. Such an example is a river flow. This phenomenon also occurs in case of conveyor belts and in the lubrication theory.

Literature is not replete on the velocity profile of a flow down an inclined plane.

Bognár, et al. in 2018 investigated the velocity distributions on an inclined plane in the transport of non-Newtonian fluids [4]. The process was modelled by boundary layer flows. They considered the equations of continuity and motion boundary conditions on the plane and on the surface of the transported material. They finally examined the velocity distribution in case of different material properties, constant plane speed and different inclination angle.

The finite element method has been used to solve a problem on the velocity distribution in viscous incompressible fluid using the langrange interpolation function and compared their result with the exact differential

equation method [5]. The plain in this case was taken to be horizontal. Also, the Finite Element Method (FEM) to determine the velocity distribution in a concentric cylindrical annulus [6]. The annulus pipe in this case was taken to be horizontal.

The aim of this study is to determine at the same time the velocity profile of a fluid in inclined plane. We will be using FEM unlike other methods that need to carry out several iterations to determine the velocities at different point.

2. Finite Element Method

Consider the flow of a Newtonian viscous fluid on an inclined flat surface, as shown in "Fig. 1". Examples of such flow can be found in wetted-wall towers and the application of coatings to wallpaper rolls. The momentum equation, for a fully developed steady laminar flow along the z coordinate, is given by

$$-\mu_1 \frac{\partial^2 w_z}{\partial x^2} = \rho g \cos\beta \tag{1}$$

where $w =$ z component of the velocity
μ = Viscocity of the fluid
g = Acceleration due to gravity and
β = Angle between the inclined surface and the vertical

The boundary conditions associated with this problem are that the stresses is zero at $x = 0$ and the velocity is zero at $x = L$.

$$\left(\frac{dw_z}{dx}\right)\Big|_{x=0} = 0 \tag{2}$$

and

$$w_z(L) = 0 \tag{3}$$

The Gerlekin Finite Element Method was used to discretize the domain (inclined plane).

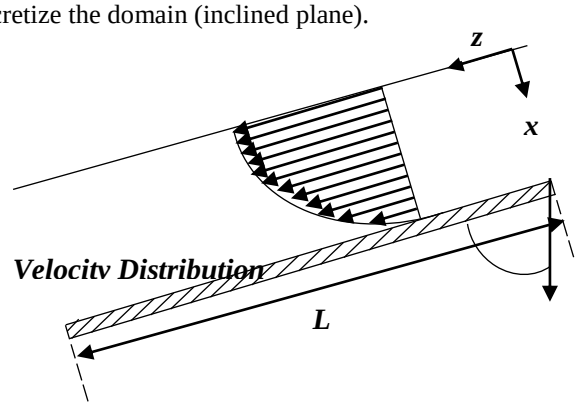

Fig. 1. Velocity Profile.

The domain of the problem consists of all points between $x = 0$ and $x = L$ i.e. $\Omega = (0, L)$. The domain was divided into a set of line elements, a typical element being of length h_e and located between two end points A and B of a typical element. The collection of such elements is called the finite element mesh of the domain. The reason for dividing the domain into finite elements was to represent the geometry of the domain and to approximate the solution over the entire domain.

2.1. Mathematical analysis

In the development of the weak form, we assumed a linear mesh and placed it over the domain. This was done by multiplying equation (1) by the weighted function (w) and integrating the final equation over the domain. This results in the mathematical expression in equation (4).

$$\int_{x_A}^{x_B} \mu \frac{\partial w}{\partial x}\frac{\partial w_z}{\partial x}\,dx - \int_{x_A}^{x_B} \rho g \cos\beta w\,dx - wQ_A - wQ_B = 0 \tag{4}$$

But $x_B = x_A + h_e$

Equation (4) is known as the weak form of the governing equation.

The weak form requires that the approximation chosen for u should be at least linear in x so that there are no terms in equation (4) that are identically zero. Since the primary variable is simply the function itself, the Lagrange family of interpolation functions is admissible. We proposed that u was the approximation over the typical finite element domain by the expression:

$$w_z = \sum_{j=1}^{n} w_j^e \psi_j^e(x) \text{ and } w = \psi_i^e(x)$$
$$i, j = 1,2,3 \tag{5}$$

where $w = \psi_i^e(x)$ is the trial function .

In Galerkin's weighted residual method, the weighting functions are chosen to be identical to the trial functions [7].

Substitute equation (5) into equation (4), we have:

$$\mu\left[K_{ij}^e\right]\left\{w_j^e\right\} = \rho g \cos\beta\left\{F_i^e\right\} + \left\{Q_i^e\right\} \tag{6}$$

where $K_{ij}^e = \int_{x_A}^{x_A+h_e} \frac{\partial \psi_i^e(x)}{\partial x}\frac{\partial \psi_j^e(x)}{\partial x}\,dx$ (7)

$$F_i^e = \int_{x_A}^{x_A+h_e} \psi_i^e(x)\,dx \tag{8}$$

$$Q_i^e = \psi_i^e(x)Q_A + \psi_i^e(x)Q_B \tag{9}$$

Equation (6) is referred to as the finite element based model while equation (7) is known as the stiffness matrix and equation (8) is referred to as the flux matrix.

Hence, the one-dimensional Lagrange quadratic interpolation function becomes

$$\psi_1 = \left(1-\frac{x}{h_e}\right)\left(1-\frac{2x}{h_e}\right) \tag{10}$$

$$\psi_2 = \frac{4x}{h_e}\left(1-\frac{x}{h_e}\right) \tag{11}$$

$$\psi_3 = -\frac{x}{h_e}\left(1-\frac{2x}{h_e}\right) \tag{12}$$

where h_e = Elemental length

2.2 Evaluating the stiffness matrix $\left[K_{ij}\right]$ *and flux matrix* $\left\{F^e\right\}$

To evaluate the K_{ij} matrix, we substitute equations 10-12 accordingly into equations (7) and (8), respectively. Then we have;

$$K^e = \frac{1}{3h_e^3}\begin{bmatrix} 7h_e^2-24h_ex_A+48x_A^2 & -8\left(h_e^2-3h_ex_A+12x_A^2\right) & h_e^2+48x_A^2 \\ -8\left(h_e^2-3h_ex_A+12x_A^2\right) & 16\left(h_e^2+12x_A^2\right) & -8\left(h_e^2+3h_ex_A+12x_A^2\right) \\ h_e^2+48x_A^2 & -8\left(h_e^2+3h_ex_A+12x_A^2\right) & 7h_e^2+24h_ex_A+48x_A^2 \end{bmatrix} \tag{13}$$

$$F^e = \begin{Bmatrix} \frac{h_e}{6}-x_A+\frac{2x_A^2}{h_e} \\ \frac{2\left(h_e^2-6x_A^2\right)}{3h_e} \\ \frac{h_e}{6}+x_A+\frac{2x_A^2}{h_e} \end{Bmatrix} \tag{14}$$

Equation (13) represents the generalized form of the stiffness matrix for the entire domain of the fluids between stationary parallel plates and equation (14) represents the generalized form of the flux matrix for the entire domain of the fluid between stationary parallel plates.

In this work, the domain of the parallel plates was divided into four quadratic elements. Therefore,

$$\left[K^e\right] = \frac{1}{3h_e}\begin{bmatrix} 7\mu_1 & -8\mu_1 & \mu_1 & 0 & 0 & 0 & 0 & 0 & 0 \\ -8\mu_1 & 16\mu_1 & -8\mu_1 & 0 & 0 & 0 & 0 & 0 & 0 \\ \mu_1 & -8\mu_1 & 14\mu_1 & -8\mu_1 & \mu_1 & 0 & 0 & 0 & 0 \\ 0 & 0 & -8\mu_1 & 16\mu_1 & -8\mu_1 & 0 & 0 & 0 & 0 \\ 0 & 0 & \mu_1 & -8\mu_1 & 7\mu_1+7\mu_2 & -8\mu_2 & \mu_2 & 0 & 0 \\ 0 & 0 & 0 & 0 & -8\mu_2 & 16\mu_2 & -8\mu_2 & 0 & 0 \\ 0 & 0 & 0 & 0 & \mu_2 & -8\mu_2 & 14\mu_2 & -8\mu_2 & \mu_2 \\ 0 & 0 & 0 & 0 & 0 & 0 & -8\mu_2 & 16\mu_2 & -8\mu_2 \\ 0 & 0 & 0 & 0 & 0 & 0 & \mu_2 & -8\mu_2 & 7\mu_2 \end{bmatrix} \tag{15}$$

$$\left\{F^e\right\} = \frac{h_e}{6}\begin{Bmatrix} 1 \\ 4 \\ 2 \\ 4 \\ 2 \\ 4 \\ 2 \\ 4 \\ 1 \end{Bmatrix} \tag{16}$$

Substitute in equation (6), equations (15) and (16) and finally, we have:

$$\begin{bmatrix} 7 & -8 & 1 & 0 & 0 & 0 & 0 & 0 & 0 \\ -8 & 16 & -8 & 0 & 0 & 0 & 0 & 0 & 0 \\ 1 & -8 & 14 & -8 & 1 & 0 & 0 & 0 & 0 \\ 0 & 0 & -8 & 16 & -8 & 0 & 0 & 0 & 0 \\ 0 & 0 & 1 & -8 & 14 & -8 & 1 & 0 & 0 \\ 0 & 0 & 0 & 0 & -8 & 16 & -8 & 0 & 0 \\ 0 & 0 & 0 & 0 & 1 & -8 & 14 & -8 & 1 \\ 0 & 0 & 0 & 0 & 0 & 0 & -8 & 16 & -8 \\ 0 & 0 & 0 & 0 & 0 & 0 & 1 & -8 & 7 \end{bmatrix}\begin{Bmatrix} u_1 \\ u_2 \\ u_3 \\ u_4 \\ u_5 \\ u_6 \\ u_7 \\ u_8 \\ u_9 \end{Bmatrix} = \frac{\rho g h_e^2 \cos\beta}{2\mu}\begin{Bmatrix} 1 \\ 4 \\ 2 \\ 4 \\ 2 \\ 4 \\ 2 \\ 4 \\ 1 \end{Bmatrix} + \begin{Bmatrix} Q_1^1 \\ Q_2^1 \\ Q_3^1+Q_1^2 \\ Q_2^2 \\ Q_3^2+Q_1^3 \\ Q_2^3 \\ Q_3^3+Q_1^4 \\ Q_2^4 \\ Q_3^4 \end{Bmatrix} \tag{17}$$

Due to balance of internal flux, $Q_2^1,\ Q_3^1+Q_1^2,\ Q_2^2,\ Q_3^2+Q_1^3,\ Q_2^3,\ Q_3^3+Q_1^4,\ Q_2^4$ are equal to zero.

Introducing the boundary conditions stated in equation (3), equation (17) reduces to

$$\begin{bmatrix} 7 & -8 & 1 & 0 & 0 & 0 & 0 & 0 \\ -8 & 16 & -8 & 0 & 0 & 0 & 0 & 0 \\ 1 & -8 & 14 & -8 & 1 & 0 & 0 & 0 \\ 0 & 0 & -8 & 16 & -8 & 0 & 0 & 0 \\ 0 & 0 & 1 & -8 & 14 & -8 & 1 & 0 \\ 0 & 0 & 0 & 0 & -8 & 16 & -8 & 0 \\ 0 & 0 & 0 & 0 & 1 & -8 & 14 & -8 \\ 0 & 0 & 0 & 0 & 0 & 0 & -8 & 16 \end{bmatrix}\begin{Bmatrix} w_1 \\ w_2 \\ w_3 \\ w_4 \\ w_5 \\ w_6 \\ w_7 \\ w_8 \end{Bmatrix} = \frac{\rho g h_e^2 \cos\beta}{2\mu}\begin{Bmatrix} 1 \\ 4 \\ 2 \\ 4 \\ 2 \\ 4 \\ 2 \\ 4 \end{Bmatrix} + \begin{Bmatrix} Q_1^1 \\ Q_2^1 \\ Q_3^1+Q_1^2 \\ Q_2^2 \\ Q_3^2+Q_1^3 \\ Q_2^3 \\ Q_3^3+Q_1^4 \\ Q_2^4 \end{Bmatrix} \tag{18}$$

3. Results and Discussion

The data used in this work are given thus:

$$\beta = 45^0,\ \rho = 2kgm^{-3},\ g = 9.81m/s,\ \mu = 0.4Pa.s,\ L = 8m$$

The exact differential equation solution of the problem is given in equation (19) [7].

$$w = \frac{\rho g L^2 \cos\beta}{2\mu}\left[1-\left(\frac{x}{L}\right)^2\right] \tag{19}$$

In this paper, the problem being analysed is the one that involves the flow of a Newtonian viscous fluid on an inclined plane. Examples of such flow can be found in wetted-wall towers and the applications to wallpaper rolls. The momentum equation, for a fully developed laminar flow along the z coordinate was used to analyse the velocity distribution of an incompressible fluid flowing down an inclined plane under the influence of a pressure gradient.

The finite element method was used to discretize the entire domain. The domain was discretized into four linear elements. In other to analyse these elements, a quadratic interpolation function was used to approximate the velocity distribution in the domain.

A graph of the velocity profile of the Newtonian viscous fluid on the inclined flat surface is as shown in "Fig. 2". The graph represents the velocity at different nodes plotted against the length of the inclined flat surface. The graph shows a parabolic relationship between the velocity and the length of the inclined flat surface. It was observed from the graph in "Fig. 2" that the velocity of the fluid at point 8m which is the boundary of the fluid and the inclined flat surface was 0m/s. This was due to the fact we applied the no slip boundary condition at the boundary (walls) of the inclined flat surface.

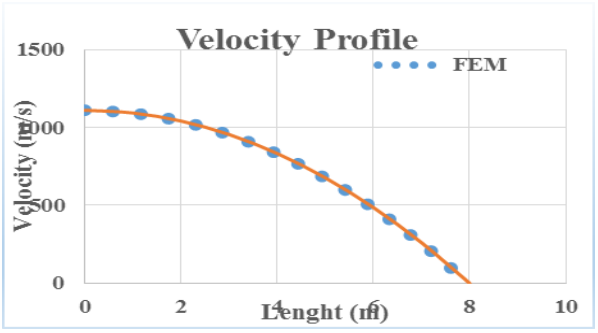

Fig. 2. A graph of velocity against length of plate.

From "Fig. 2", between 0 and 8m represents the velocity profile. Point 0m is the open surface of the inclined flat surface while point 8m in the wall of the inclined flat surface. From this analysis the maximum velocity of 1109.8748m/s was attained at the open surface of the incline plane.

To verify the accuracy of the results obtained from the Finite Element Method, the results obtained was compared with the results obtained using the exact differential equation method. It was observed from the two methods that their results were in good agreement with one another. From the results shown in Table 1, even with just four linear elements, we were able to have a very high accuracy with a maximum percentage error of 2.3413×10^{-14}. The advantage of the finite element method over the exact differential equation method is that the FEM gives results that represent the velocities at different nodes for the whole material under consideration at the same time unlike the result from the exact differential equation method that provide discrete result at a time and needs further iteration to determine the velocity values at other points of the stationary parallel plates

Table 1. Comparison between the Exact Solution and the FEM Solution

LENGTH	FEM	EXACT	% ERROR
0	1109.8748	1109.8748	0.0000
1	1092.5330	1092.5330	0.0000
2	1040.5076	1040.5076	2.1852E-14
3	953.7987	953.7987	0.0000
4	832.4061	832.4061	1.3658E-14
5	676.3300	676.3300	1.6809E-14
6	485.5702	485.5702	2.3413E-14
7	260.1269	260.1269	2.1852E-14
8	0.0000	0.0000	0.0000

3.1. Effect of change in inclination angle on the velocity profile

In this analysis, it was observed that as the angle of inclination increases, the velocity decreases as well. It is important to note that the angle of inclination was measured between the wall of the inclined material and the vertical. This is shown in "Fig. 2".

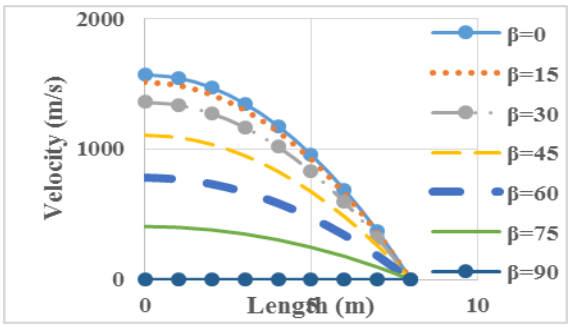

Fig. 3. A graph of velocity against length of plate at different angles of inclination

It is clear here that maximum velocity can be achieved when the angle of inclination is 0° (Zero degree). At this point, with all other parameters held constant, the maximum velocity attained was 1569.6m/s. Also, holding other parameters constant and increasing the angle of inclination, the velocity decreases until an angle of inclination of 90°. At this point, the velocity is almost zero. This can be well represented in "Fig. 4".

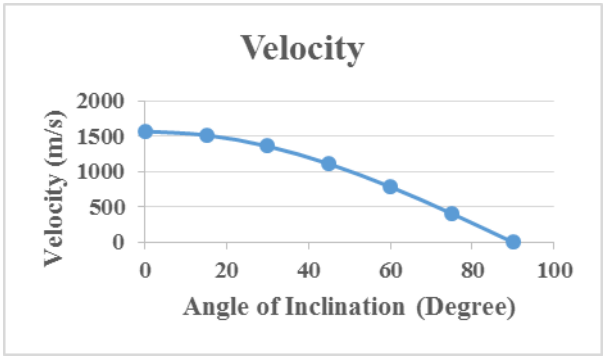

Fig. 4. A graph of velocity against angles of inclination.

In the design of a drainage system for example, the angle of inclination should be set well above 0°, else, the fluid in the drainage will not drained thereby having stagnant fluid which might have detrimental effect on the drainage.

3.2. Effect of Change in Fluid Viscosity and Density on the Velocity Profile

Examining the effect of the change in viscosity on the velocity profile, it was observed that viscosity affect the velocity profile. With an increase in the viscosity of a fluid, the velocity of the fluid was seen to decrease. This decrease in the velocity was as a result of the increase in the drag between the wall of the inclined material and the fluid. This can be shown in "Fig. 5".

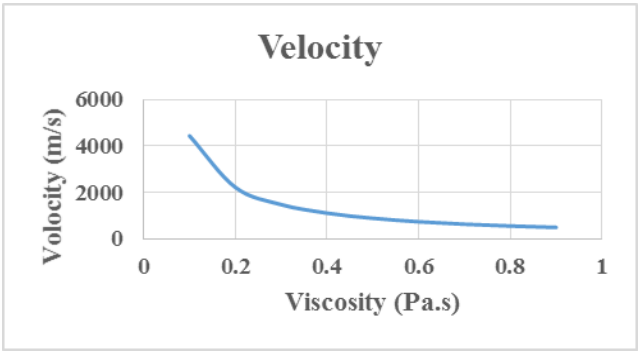

Fig. 5. A graph of velocity against change in viscosity.

Also looking at the effect of a change in the fluid density on the velocity distribution, it was observed that a change in fluid density has a linear relationship with the velocity of the fluid. This means that the higher the fluid density, the higher the velocity of the fluid. This is as shown in "Fig. 6".

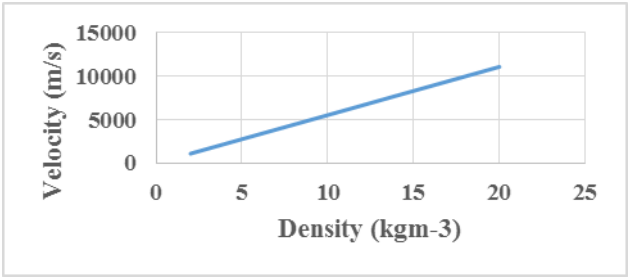

Fig. 6. A graph of velocity against change in density.

4. Conclusion

So far, the finite element method has been used to obtain the velocity profile of a fluid on an inclined plane with steady laminar flow. The results obtained from the FEM were compared with the results obtained from the exact differential equation method and it was discovered that both results agrees. It has also been shown that the higher the angle of inclination and fluid viscosity, the lower the velocity and also the higher the fluid density, the higher the velocity. The result obtained shows that the finite element method is an efficient and accurate method.

References

[1] C. Ancey, ''Flow down inclined channel as a discriminating experiment'', Research Report 2003.

[2] D. Benedetto, E. Caglioti, M. Pulvirenti, ''A kinetic equation for granular media'', RAIRO Mathematical Modeling and Numerical Analysis. Vol. 31, No. 5, pp. 615-641, 1997.

[3] D. Benedetto, M. Pulvirenti, ''On the one-domensional Boltzman equation for granular flows, Physics of Fluids, Vol. 16, No. 12, pp. 4235-4247, 2001.

[4] G. Bognár, I. Gombkötő, K. Hriczó, ''Non-Newtonian Fluid Flow down an Inclined Plane'', Recent Advances in Fluid Mechanics, Heat & Mass Transfer, pp. 129-134, 2018.

[5] J. A. Akpobi, E. D. Akpobi, ''A finite element analysis of the distribution velocity in viscous incompressible fluids using the Lagrange interpolation function'', Journal of Applied Science and Environmental Management, Vol. 11, pp. 31–38, 2007.

[6] I. D. Erhunmwun, M. H. Oladeinde, ''Analysis of flow in a concentric annulus using finite element method'', Nigeria Journal of Technology, Vol. 35, pp. 344-348, 2016.

[7] J. N. Reddy, ''Introduction to the Finite Element Method'', Second edition, McGraw-Hill series in Mechanical Engineering. 1993. Ch. 3.

One–Dimensional Solute Transport for an Input against the Flow in a Homogeneous Finite Porous Media

Raja Ram Yadav *‡, Joy Roy *, Dilip Kumar Jaiswal**

*Department of Mathematics &Astronomy,University of Lucknow, Lucknow-226007, India

**Faculty of Mathematical & Statistical Sciences, Shri Ramswaroop Memorial University, Lucknow, U.P., India.

(yadav_rr2@yahoo.co.in,joyroy2904@gmail.com, dilip3jais@gmail.com)

‡ Corresponding Author:R.R.Yadav, Department of Mathematics & Astronomy,

University of Lucknow, Lucknow-226007, India, Tel: +91 945 065 48 20, yadav_rr2@yahoo.co.in

Received: 02.12.2017 Accepted:20.04.2019

Abstract-A theoretical model comprising advection-dispersion equation with temporal seepage velocity, dispersion coefficient and time dependent pulse type input of uniform nature applied against the flow is studied in a finite porous domain. Input concentration is any continuous smooth function of time acts up to some finite time and then eliminated. Concentration gradient at other boundary is proportional to concentration. Dispersion is proportional to seepage velocity. Interpolation method is applied to reduce the input function into a polynomial. Certain transformations are utilized to reduce the variable coefficient advection-dispersion equation into constant coefficient. The Laplace Transform Technique is applied to get the solution of advection dispersion equation. Two different functions of input are discussed to understand the utility of the present study. Obtained result is demonstrated graphically with the help of numerical example.

Keywords Advection, Dispersion, Porous Medium, Interpolation, Laplace Transformation Technique.

1. Introduction

The advection-dispersion equation (ADE) commonly used for transport of solute in porous media comprises advection and hydrodynamic dispersion where former is controlled by the Darcy's law and later by the combination of mechanical and molecular diffusion which accounts for contaminant arising/spreading stimulated by velocity variations. Advection-dispersion equation may be defined for scale or time or both dependent dispersion/seepage velocity, homogeneous/heterogeneous medium including presence of decay and production of solute depending upon geological formation. Solutions of the ADEs can be obtained analytically or numerically using various methods. Analytical solutions are usually applicable for ideal geometrical conditions while numerical solutions are more flexible comparison to analytical solution to deal with real life problems consisting of non- ideal geometric conditions. On the other hand, analytical solutions is far accurate and dependable comparison to numerical solutions those hardly free from errors. A plenty of analytical solutions comprising various initial boundary and geometrical conditions through one/two/three-dimensional transport problem in porous formation which may be finite /infinite are published in literature up to the date. In the study of solute transport phenomena [1] explained that conductivity is not only responsible for spatial variation in groundwater velocity. An analytical solution was proposed for a solute transport problem with scale dependent dispersion in a heterogeneous porous media [2]. An aspect of solute transport phenomena was established with the fact that hydrodynamic dispersion coefficients are non-linear function of the seepage velocity [3]. Analytical solutions may be obtained by using several techniques according to the nature of the problem. A two dimensional analytical solution was evaluated considering the solute transport for a bounded aquifer by adopting Fourier analysis and Laplace Transform [4]. [5] conceptualized an overlapping control volume method for transient solute transport problems in groundwater to obtain the numerical solution of transport problems. Streamline method was applied in solving the solute transport problem in a single

fracture and the method was validated with experimental data [6]. Some analytical solutions were derived for the ADE in cylindrical coordinates by using a Bessel function expansion [7]. Laplace Transformation Technique (LTT) was explored to evaluate analytical solutions of transport problems [8] [9] [10]. First two obtained solutions for pulse type input in one-dimensional transport while last one addressed the problem consisting of space dependent dispersion, velocity and retardation. An analytical result for solute transport problem in a heterogeneous porous medium was proposed to analyze scale dependent dispersion with linear isotherm [11]. By using generalized integral transform technique (GITT) [12] obtained solution for finite one-dimensional domain for dispersion coefficient and velocity which are proportional to non-homogeneous linear expression in position variable while in another study an analytical solution of ADE was evaluated in multi-layer porous media [13]. Two–dimensional solution is obtained for a finite domain porous medium with pulse type input by considering it at the top layer of the outer boundary and at the intermediate portion in the aquifer [14]. Using Green's function an analytical solution of one dimensional porous medium for instantaneous and continuous point source taking dispersion and velocity mutually proportional was developed in groundwater and riverine flow [15]. In numerical solutions, a two-dimensional model based on numerical simulations, equi-concentration lines presented approximate description of time-dependent transport [16]. Finite-volume method has been used for solving the advection and dispersion processes of the virus transport equation describing the movement of virus in one-dimensional unsaturated porous media [17]. The aquifers are always of finite length and therefore the study of solute transport phenomena in finite domain has been much valuable to deal with real world problem. Solute transport phenomena for finite domain was studied to understand the effect of periodic dispersion, velocity along with periodic input [18] [19].

In present paper, interpolation method is used for reducing generalize input into a polynomial for a finite domain study. Laplace transformation Technique is used to get solution of solute transport phenomena with temporal dispersion and for the input which is poised against the flow.

2. Mathematical Formulation and Solution of the Problem

In the present study, solute transport is assumed as one-dimensional on a horizontal plane in a saturated finite length porous medium domain. The governing equation of solute transport in porous media which is a parabolic type partial differential equation is derived on basis of mass conservation and Fick's law of diffusion may be written as follows [20],

$$R\frac{\partial c}{\partial t}=\frac{\partial}{\partial x}\left(D(x,t)\frac{\partial c}{\partial x}-u(x,t)\ c\right) \quad (1)$$

where $c\left[ML^{-3}\right]$, $u\left[LT^{-1}\right]$, $D\left[L^2T^{-1}\right]$ and R are representing solute concentration, seepage velocity, dispersion coefficient and retardation factor respectively at position $x[L]$ and at time $t[T]$. The dispersion coefficient, combined effect of molecular diffusion and mixing in the axial direction, is assumed to be proportional to seepage velocity u (Yim and Mohsen,1992). The dispersion coefficient and seepage velocity both are time dependent and defined as $u(x,t)=u_0(1+mt)^{-1}$, $D=D_0(1+mt)^{-1}$. Retardation R is R_0 and where $D_0\left[L^2T^{-1}\right], u_0\left[LT^{-1}\right]$ and R_0 are constants. Here unsteady parameter $m\left[T^{-1}\right]$ regulates the dependency of the dispersion and seepage velocity on time .Therefore, Eq.(1) may be re-written as;

$$R_0\frac{\partial c}{\partial t}=\frac{\partial}{\partial x}\left(D_0(1+mt)^{-1}\frac{\partial c}{\partial x}-u_0(1+mt)^{-1}c\right) \quad (2)$$

The geological formation which is assumed to be of finite length along horizontal direction is initially polluted and its dependency may be defined as sine hyperbolic function of space. Input at one end is considered against the flow and may be defined as any continuous smooth function of time while concentration gradient at other end of finite domain is supposed proportional to concentration. In order to formulate the proposed problem mathematically, the initial and boundary condition may be written as;

$$c(x,t)=c_i\sinh(\alpha x);\ L_1\le x\le L,\ t=0 \quad (3)$$

$$c(x,t)=,\begin{cases} c_0F(m't);\ 0<t\le t_0 & \text{(4a)}\\ x=L & \\ 0\ ;\ t>t_0 & \text{(4b)}\end{cases}$$

$$\frac{\partial c(x,t)}{\partial x}=\frac{u_0}{2D_0}c\ ;\text{as } x=L_1 \quad (5)$$

where, c_0 and c_i are the reference and resident concentrations respectively. $m'[T^{-1}]$ is an unsteady parameter and $\alpha[L^{-1}]$ is a constant on which initial concentration depends. Dimensionless $F(m't)(\ge 0)$ is continuous , smooth (differentiable) and bounded function in a time domain $[0,t_0]$. Weirstrass approximation theorem says that any continuous function on a bounded interval can be uniformly approximated by polynomial function. Since $F(m't)$ is continuous and bounded in domain $[0,t_0]$, following Weirstrass approximation theorem, $F(m't)$ may be written as interpolation polynomial in t of degree n. Hence Eqs. (3-5) may be written as;

$$c(x,t)=c_i\sinh(\alpha x);\ L_1\le x\le L,\ t=0 \quad (6)$$

$$c(x,t)=,\begin{cases} c_0G_n(t);\ 0<t\le t_0 & \text{(7a)}\\ x=L & \\ 0\ ;\ t>t_0 & \text{(7b)}\end{cases}$$

$$\frac{\partial c(x,t)}{\partial x}=\frac{u_0}{2D_0}c\ ;\text{at } x=L_1\ ,\ t\ge 0 \quad (8)$$

where, dimensionless quantity $G_n(t)$ which is interpolation polynomial may be defined as;

$$G_n(t) = a_0 + a_1 t + a_2 t^2 + \ldots\ldots\ldots + a_n t^n \quad (9)$$

and a_i's are constants. For reducing the Eq.(2) into a constant coefficient, a new time variable T is introduced with following transformation [21]

$$T = \int_0^t (1+mt)^{-1} dt \quad \text{or} \quad T = \frac{1}{m}\log(1+mt)$$

and $t = \frac{1}{m}\left(e^{mT} - 1\right)$ (10)

With transformation Eq. (10), Eq. (2) and Eqs. (6-8) are reduced into following form:

$$R_0 \frac{\partial c}{\partial T} = D_0 \frac{\partial^2 c}{\partial x^2} - u_0 \frac{\partial c}{\partial x} \quad (11)$$

$$c(x,T) = c_i \sinh(\alpha x)\,; L_1 \le x \le L,\ T = 0 \quad (12)$$

$$c(x,T) = \begin{cases} H(T); 0 < T \le T_0 & (13a) \\ x = L & \\ 0\,; T > T_0 & (13b) \end{cases}$$

$$\frac{\partial c(x,T)}{\partial x} = \frac{u_0}{2D_0} c\,; \text{at } x = L_1,\ T \ge 0 \quad (14)$$

where,

$$H(T) = c_0 G_n\left(\frac{e^{mT}-1}{m}\right) = b_0 + b_1 e^{mT} + b_2 e^{2mT} + \ldots.. + b_n e^{nmT}$$

& $T_0 = \frac{1}{m}\log(1+mt_0)$ and b_i's are having dimension $\left[ML^{-3}\right]$.

A new transformation is introduced so as to convective term in advection-dispersion equation Eq. (11) may be removed. The transformation follows as [19]:

$$c(x,T) = k(x,T)\exp\left[\frac{u_0}{2D_0}x - \frac{u_0^{\,2}}{4D_0R_0}T\right] \quad (15)$$

Therefore Eqs. (11-14) are reduced into:

$$R_0 \frac{\partial k}{\partial T} = D_0 \frac{\partial^2 k}{\partial x^2} \quad (16)$$

$$k(x,T) = \frac{1}{2} c_i \begin{bmatrix} \exp\{(\alpha-\beta)x\} - \\ \exp\{-(\alpha+\beta)x\} \end{bmatrix};\ L_1 \le x \le L,\ T = 0 \quad (17)$$

$$k(x,T) = \begin{cases} \{H(T)\}\exp\left(-\beta x + \eta^2 T\right); 0 < T \le T_0 & (18a) \\ x = L & \\ 0\,; T > T_0 & (18b) \end{cases}$$

$$\frac{\partial k(x,T)}{\partial x} = 0\,; \text{at } x = L_1, T \ge 0 \quad (19)$$

where $\beta = \frac{u_0}{2D_0}$ and $\eta = \sqrt{\frac{u_0^{\,2}}{4D_0R_0}}$

Applying Laplace transformation on Eqs. (16–19) to reduce Eq. (16) into ordinary differential equation.

$$\frac{d^2\bar{k}}{dx^2} - \frac{pR}{D_0}\bar{k} = -\frac{R_0}{D_0}\left[\frac{1}{2}c_i\begin{bmatrix}\exp\{(\alpha-\beta)x\} - \\ \exp\{-(\alpha+\beta)x\}\end{bmatrix}\right] \quad (20)$$

$$\bar{k}(x,p) = \exp(-\beta L)\sum_{r=0}^{n} b_r \frac{\left[1 - \exp-\left\{p - \left(\eta^2 + rm\right)\right\}T_0\right]}{\left\{p - \left(\eta^2 + rm\right)\right\}};$$

$$x = L \quad (21)$$

$$\frac{d\bar{k}}{dx} = 0\,; \text{as } x = L_1, T > 0 \quad (22)$$

The general solution of Eq. (20) may be written as;

$$\bar{k}(x,p) = c_1\cosh(Mx) + c_2\sinh(Mx) + \frac{c_i}{2} \times \left[\frac{\exp\{(\alpha-\beta)x\}}{\left\{p - \frac{D_0}{R_0}(\alpha-\beta)^2\right\}} - \frac{\exp\{-(\alpha+\beta)x\}}{\left\{p - \frac{D_0}{R_0}(\alpha+\beta)^2\right\}}\right] \quad (23)$$

where, $M = \sqrt{\frac{R_0 p}{D_0}}$

Solution of the present problem may be obtained by using Eq.(21) and Eq.(22)in Eq.(23). So coefficient may be written as;

$$c_1 = \exp(-\beta L)\sum_{r=0}^{n} b_r \frac{\left[1 - \exp-\left\{p - \left(\eta^2 + rm\right)\right\}T_0\right]}{\left\{p - \left(\eta^2 + rm\right)\right\}} \times$$

$$\frac{\cosh(ML_1)}{\cosh(ML - ML_1)} - \frac{c_i}{2}\left[\frac{1}{\left\{p - \frac{D_0}{R_0}(\alpha-\beta)^2\right\}} \times \right.$$

$$\left\{\frac{\exp\{(\alpha-\beta)L\}\cosh ML_1}{\cosh(ML - ML_1)} - \frac{(\alpha-\beta)\exp\{(\alpha-\beta)L_1\}\sinh ML}{M\cosh(ML - ML_1)}\right\}$$

$$- \frac{1}{\left\{p - \frac{D_0}{R_0}(\alpha+\beta)^2\right\}} \times$$

$$\left.\left\{\frac{\exp\{-(\alpha+\beta)L\}\cosh ML_1}{\cosh(ML - ML_1)} - \frac{-(\alpha+\beta)\exp\{-(\alpha+\beta)L_1\}\sinh ML}{M\cosh(ML - ML_1)}\right\}\right] \quad (24)$$

and

$$c_2 = -\exp(-\beta L)\sum_{r=0}^{n} b_r \frac{\left[1-\exp-\{p-(\eta^2+rm)\}T_0\right]}{\{p-(\eta^2+rm)\}} \frac{\sinh(ML_1)}{\cosh(ML-ML_1)} -$$
$$\frac{c_i}{2}\left[\frac{1}{\left\{p-\frac{D_0}{R_0}(\alpha-\beta)^2\right\}}\times\left\{\frac{(\alpha-\beta)\exp\{(\alpha-\beta)L_1\}\cosh ML}{M\cosh(ML-ML_1)} - \frac{\exp\{(\alpha-\beta)L\}\sinh ML_1}{\cosh(ML-ML_1)}\right\} - \right.$$
$$\left.\frac{1}{\left\{p-\frac{D_0}{R_0}(\alpha+\beta)^2\right\}}\times\left\{\frac{-(\alpha+\beta)\exp\{-(\alpha+\beta)L_1\}\cosh ML}{M\cosh(ML-ML_1)} - \frac{\exp\{-(\alpha+\beta)L\}\sinh ML_1}{\cosh(ML-ML_1)}\right\}\right] \quad (25)$$

Therefore putting the value of c_1 and $c_2$from Eq. (24&25) , Eq.(23)may be written as:

$$\bar{k}(x,p) = \left[\exp(-\beta L)\sum_{r=0}^{n} b_r \frac{\left[1-\exp-\{p-(\eta^2+rm)\}T_0\right]}{\{p-(\eta^2+rm)\}} \frac{\cosh(ML_1)}{\cosh(ML-ML_1)} -\right.$$
$$\frac{c_i}{2}\left[\frac{1}{\left\{p-\frac{D_0}{R_0}(\alpha-\beta)^2\right\}}\times\left\{\frac{\exp\{(\alpha-\beta)L\}\cosh ML_1}{\cosh(ML-ML_1)} - \frac{(\alpha-\beta)\exp\{(\alpha-\beta)L_1\}\sinh ML}{M\cosh(ML-ML_1)}\right\} - \right.$$
$$\left.\left.\frac{1}{\left\{p-\frac{D_0}{R_0}(\alpha+\beta)^2\right\}}\times\left\{\frac{\exp\{-(\alpha+\beta)L\}\cosh ML_1}{\cosh(ML-ML_1)} - \frac{-(\alpha+\beta)\exp\{-(\alpha+\beta)L_1\}\sinh ML}{M\cosh(ML-ML_1)}\right\}\right]\right]\times$$
$$\cosh(Mx)+\left[-\exp(-\beta L)\sum_{r=0}^{n} b_r \frac{\left[1-\exp-\{p-(\eta^2+rm)\}T_0\right]}{\{p-(\eta^2+rm)\}} \frac{\sinh(ML_1)}{\cosh(ML-ML_1)} -\right.$$
$$\frac{c_i}{2}\left[\frac{1}{\left\{p-\frac{D_0}{R_0}(\alpha-\beta)^2\right\}}\times\left\{\frac{(\alpha-\beta)\exp\{(\alpha-\beta)L_1\}\cosh ML}{M\cosh(ML-ML_1)} - \frac{\exp\{(\alpha-\beta)L\}\sinh ML_1}{\cosh(ML-ML_1)}\right\}\right.$$
$$\left.\left.-\frac{1}{\left\{p-\frac{D_0}{R_0}(\alpha+\beta)^2\right\}}\times\left\{\frac{-(\alpha+\beta)\exp\{-(\alpha+\beta)L_1\}\cosh ML}{M\cosh(ML-ML_1)} - \frac{\exp\{-(\alpha+\beta)L\}\sinh ML_1}{\cosh(ML-ML_1)}\right\}\right]\right]\times$$
$$\sinh(Mx)+\frac{c_i}{2}\left[\frac{\exp\{(\alpha-\beta)x\}}{\left\{p-\frac{D_0}{R_0}(\alpha-\beta)^2\right\}} - \frac{\exp\{-(\alpha+\beta)x\}}{\left\{p-\frac{D_0}{R_0}(\alpha+\beta)^2\right\}}\right] \quad (26)$$

Or

$$\bar{k}(x,p) = \left[\left\{\exp(-\beta L)\sum_{r=0}^{n} b_r \frac{\left[1-\exp-\{p-(\eta^2+rm)\}T_0\right]}{\{p-(\eta^2+rm)\}}\right\} \frac{\cosh(Mx-ML_1)}{\cosh(ML-ML_1)} -\right.$$
$$\frac{c_i}{2}\left[\frac{1}{\left\{p-\frac{D_0}{R_0}(\alpha-\beta)^2\right\}}\left\{\frac{\exp\{(\alpha-\beta)L\}\cosh(Mx-ML_1)}{\cosh(ML-ML_1)} + \frac{(\alpha-\beta)\exp\{(\alpha-\beta)L_1\}\sinh(Mx-ML)}{M\cosh(ML-ML_1)}\right\} - \right.$$
$$\left.\frac{1}{\left\{p-\frac{D_0}{R_0}(\alpha+\beta)^2\right\}}\left\{\frac{\exp\{-(\alpha+\beta)L\}\cosh(Mx-ML_1)}{\cosh(ML-ML_1)} + \frac{-(\alpha+\beta)\exp\{-(\alpha+\beta)L_1\}\sinh(Mx-ML)}{M\cosh(ML-ML_1)}\right\}\right] +$$
$$\frac{c_i}{2}\left[\frac{\exp\{(\alpha-\beta)x\}}{\left\{p-\frac{D_0}{R_0}(\alpha-\beta)^2\right\}} - \frac{\exp\{-(\alpha+\beta)x\}}{\left\{p-\frac{D_0}{R_0}(\alpha+\beta)^2\right\}}\right] \quad (27)$$

Taking inverse Laplace transform of equation (27), the solution of advection-dispersion equation may be obtained as;

$$c(x,T) = \left[\exp(-\beta L)\sum_{r=0}^{n} b_r F_r(x,T) + \frac{c_i}{2}\{I_\alpha(x,T) - I_{-\alpha}(x,T)\}\right] \times \exp\left[\frac{u_0}{2D_0}x - \frac{{u_0}^2}{4D_0R_0}T\right]$$
$$; \ 0 \le T \le T_0 \quad (28a)$$

and

$$c(x,T) = \left[\exp(-\beta L)\sum_{r=0}^{n} b_r \left[F_r(x,T) - F_r(x,T-T_0)\exp\{{\eta_r}^2 T_0\}\right] + \frac{c_i}{2}\{I_\alpha(x,T) - I_{-\alpha}(x,T)\}\right] \times \exp\left[\frac{u_0}{2D_0}x - \frac{{u_0}^2}{4D_0R_0}T\right]$$
$$; \ T_0 \le T \quad (28b)$$

where,

$$I_\phi(x,T) = \exp\{\phi x - \beta x + q_\phi T\} - \exp(\phi L - \beta L)\times$$
$$\left[e^{q_\phi T}\frac{\cosh\{(x-L_1)\sqrt{q_\phi R_0/D_0}\}}{\cosh\{(L-L_1)\sqrt{q_\phi R_0/D_0}\}} - 2\pi D_0(L-L_1)^2\right.$$
$$\sum_{s=0}^{\infty}\left\{\frac{(-1)^s(s+1/2)\cos\left\{(s+1/2)\pi\frac{(x-L_1)}{(L-L_1)}\right\}}{\{(s+1/2)^2\pi^2 D_0 + q_\phi R_0(L-L_1)^2\}}\times\right.$$
$$\left.\left.exp\left\{\frac{-(s+1/2)^2\pi^2 D_0}{R_0(L-L_1)^2}T\right\}\right\}\right] - (\phi-\beta)\exp(\phi L_1 - \beta L_1)\times$$
$$\left[e^{q_\phi T}\frac{\sinh(x-L)\sqrt{q_\phi R_0/D_0}}{\cosh(L-L_1)\sqrt{q_\phi R_0/D_0}} - 2D_0(L-L_1)\times\right.$$
$$\sum_{s=0}^{\infty}\left\{\frac{(-1)^s\sin\left\{(s+1/2)\pi\frac{(x-L)}{(L-L_1)}\right\}}{\{(s+1/2)^2\pi^2 D_0 + q_\phi R_0(L-L_1)^2\}}\times\right.$$
$$\left.\left.exp\left\{\frac{-(s+1/2)^2\pi^2 D_0}{R_0(L-L_1)^2}T\right\}\right\}\right]$$

$$F_r(x,T) = \exp\{{\eta_r}^2 T\}\frac{\cosh\left\{(x-L_1)\eta_r\sqrt{\frac{R_0}{D_0}}\right\}}{\cosh\left\{(L-L_1)\eta_r\sqrt{\frac{R}{D_0}}\right\}} -$$
$$2\pi D_0(L-L_1)^2\times\sum_{s=0}^{\infty}\left[\frac{(-1)^s(s+1/2)\cos\left\{(s+1/2)\pi\frac{(x-L_1)}{(L-L_1)}\right\}}{\{(s+1/2)^2\pi^2 D_0 + {\eta_r}^2 R_0(L-L_1)^2\}}\times\right.$$
$$\left.\exp\left\{\frac{-(s+1/2)^2\pi^2 D_0}{R_0(L-L_1)^2}T\right\}\right]$$

$\eta_r = \sqrt{\eta^2 + rm}$ and $q_\phi = \dfrac{D_0(\phi-\beta)^2}{R_0}$

3. Result and Discussion

The obtained solution Eqs. (28a, b) is discussed for two form of input functions, namely $F(m't) = c_0\{l + \sin(m't)\}$ and $F(m't) = c_0 \exp(m't)$ in a finite domain $0 \le x(m) \le 4$ along longitudinal direction for a chosen set of data taken from the experimental and theoretical published literatures are illustrated graphically. For both cases, the concentration values c/c_0 are evaluated assuming reference concentrations as $c_0 = 1.0, c_i = 0.01$. Source is applied up to time $t_0(day) = 9$. Other values of common parameters seepage velocity, dispersion coefficient are taken as $u_0 = 1.32(m\ day^{-1})$, $D_0 = 1.66(m^2 day^{-1})$, and $R_0 = 1.45$ respectively. The range of groundwater velocity is taken from $2\,m/day$ to $2\,m/year$ depending upon geometrical conditions of porous medium [22].

3.1. Case I-When input is of the form $F(m't) = c_0\{l + \sin(m't)\}$

For the present case, the value of frequency $m'(day^{-1})$, $m(day^{-1})$ and parameter l are taken 0.8, 0.8 and 2 respectively. Concentration value in the time domain $0 \le t(day) \le 9$ are computed at times $t(day) = 2,5$ and 8 while for $t(day) > 9 (= t_0)$ the same is computed at times $t(day) = 10,12$ and 14.

Figure 1(a) and 1(b) demonstrate the concentration pattern of solute transport for line graph at times $t(day) = 2,5,8$ and surface plot (c-x-t) respectively. As time elapses, concentration at $x(m) = 4$ fluctuates due to sinusoidal nature of input. Input concentration is shown fluctuating nearly between 1 and 3 value of c/c_0 which is in good agreement with periodic nature input. Surface plot helps us gauge the concentration pattern for any combination time and space. It may be observed that concentration reduces to its lowest on proceeding from $x(m) = 4$ to $x(m) = 0$ for each time in the time domain $(0 \le t(day) \le 9)$.

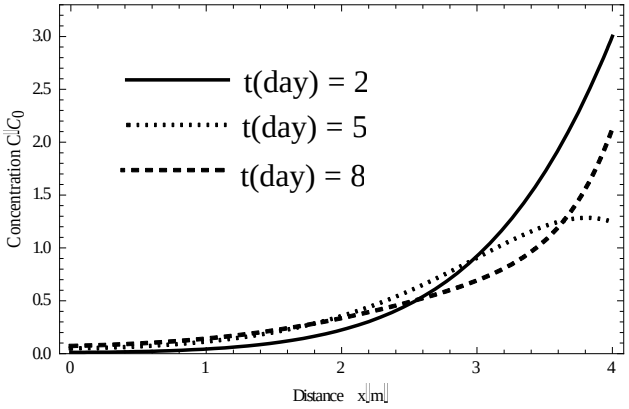

Fig.1(a). Distribution of dimensionless concentration for various time $(0 \le t \le t_0)$

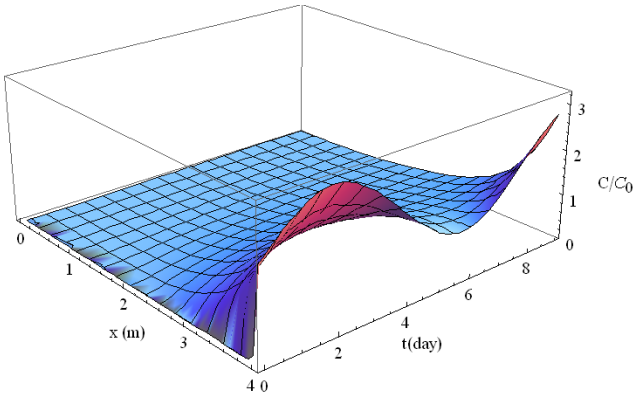

Fig.1(b). Surface plot of Distribution of dimensionless concentration for time $(0 \le t \le t_0)$.

Figure 2(a) and 2(b) are drawn to study the concentration pattern in absence of solute at times $t(day) = 10,12,14$ and surface plot (c-x-t) respectively. On elimination of the source acting against the flow at far end boundary of the domain i.e., $x(m) = 4$ the concentration at this end is measured zero. From Fig. 2(a) it is depicted that maximum concentration is lower is for higher time and higher for lower. Since there is no source of contaminant for time $t(day) > 9$, from the Fig. 2(b) it may be observed that concentration gradually attenuates with time throughout the domain.

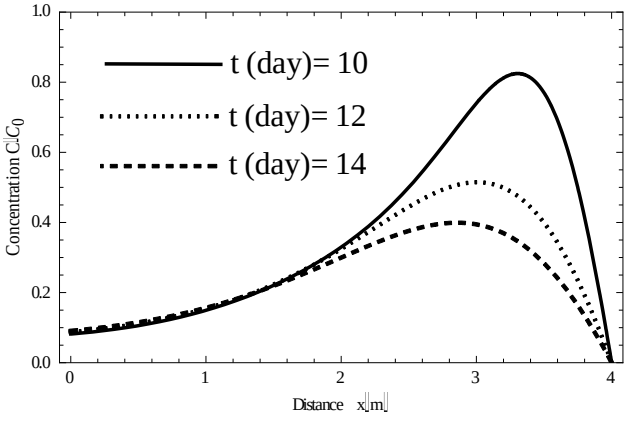

Fig. 2(a). Distribution of dimensionless concentration for various time $(t_0 < t)$

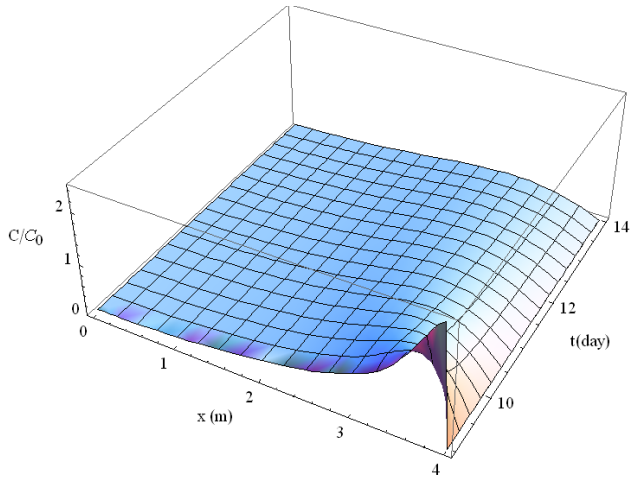

Fig. 2(b). Surface plot of Distribution of dimensionless concentration for time $(t_0 < t)$

3.2. Case II-When input is of the form $F(m't) = c_0 \exp(m't)$

For the present case, the value of unsteady parameters is $m'(day^{-1}) = 0.2$ and $m(day^{-1}) = 0.1$. Concentration values in the time domain $0 \le t(day) \le 9$ are computed at times $t(day) = 2,5$ and 8 while for $t > 9 (= t_0)$ the same is computed at times $t(day) = 10,12$ and 14.

Figure 3(a) and 3(b) explore the concentration pattern of solute transport with line graph at times $t(day) = 2,5,8$ and surface plot (c-x-t) respectively in presence of input source. With increase of time, concentration at $x(m) = 4$ increases because input is increasing exponentially with time. Figure 3(a) exhibits that rate of concentration increment is rapid from time $5(day)$ to $8(day)$ throughout the domain in comparison to same duration from time $2(day)$ to $5(day)$. From Fig. 3(b) concentration pattern for any combination time and space can be analyzed when the source is present. It is recorded that concentration c/c_0 is nearly 1 at time $t(day) = 0$ at far end i.e., $x(m) = 4$ which is in accordance of our input for this case.

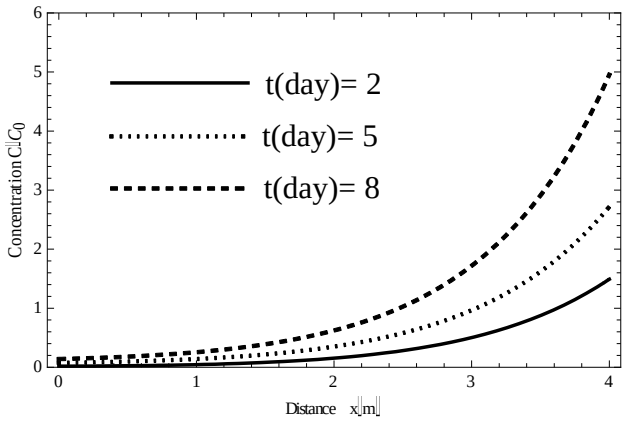

Fig. 3(a). Distribution of dimensionless concentration for various time $(0 \le t \le t_0)$

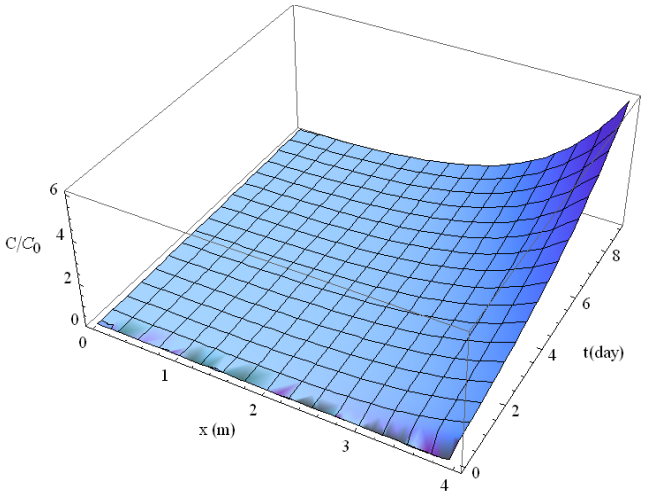

Fig. 3(b). Surface plot ofDistribution of dimensionless concentration for time $(0 \le t \le t_0)$.

Figure 4(a) and 4(b) are plotted to examine concentration pattern in absence of source with concentration-space graph at times $t(day) = 10,12,14$ and c-x-t graph respectively. Like Fig. 2(b) the solute concentration at the far end reduce to zero as the source eliminated. From the Fig. 4(a) it recorded concentration peak drops sharp with increase of time. It is revealed fromFig. 4(b) that concentration attenuated very fast as the source is eliminated.

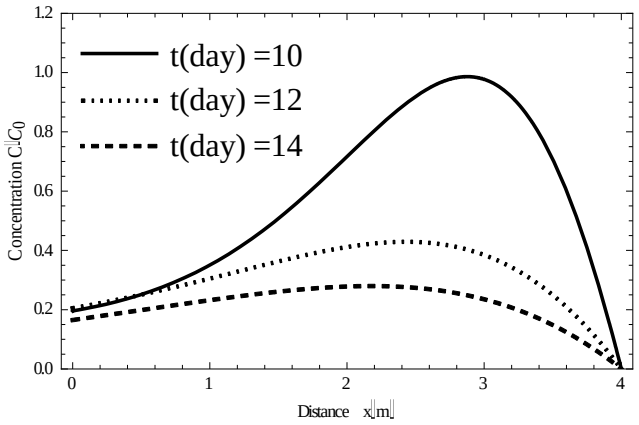

Fig. 4(a). Distribution of dimensionless concentration for various time $(t_0 < t)$

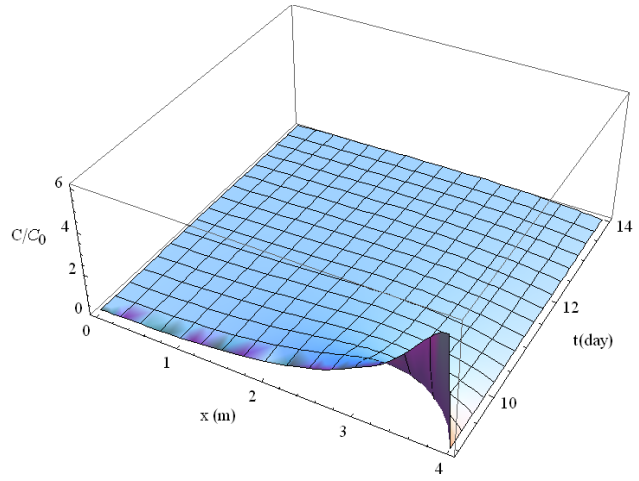

Fig. 4(b). Surface plot of distribution of dimensionless concentration for $(t > t_0)$

4. Verification of Solution

Consider the case where input for $F(m't) = 1/(1+m't)$ and $m' = m$ the solution (A7&A8) is obtained the way given in appendix. For a chosen set of data taken from the experimental and theoretical published literatures described as $c_0 = 1.0$, $c_i = 0.01\ u_0 = 1.32(m\ day^{-1})$ and $D_0 = 1.66(m^2 day^{-1})$, $R = 1.45, \alpha = 0.032$ and $m = m' = 0.2$ respectively and with time of elimination of source $t_0(day) = 9$, concentration- space graphs Figs. 5(a)and 5(b) are plotted from solution Eqs. (24&24b) and Eqs. (A7andA8) in appendix in domain $0 \le x(m) \le 4$ times $t(day) = 1,5 and 9$ in presence of source, while at times $t(day) = 10,12$ and 14 in absence of source.

The Figs. 5(a) and 5(b) are drawn to compare the solution Eqs. (28a&28b) and solution Eqs. (A7andA8) in presence and absence of source respectively. The Figs. 5(a) and 5(b) show good agreement in the both of the solutions. In further above result verifies the solution Eqs.(28aand28b) at some extent.

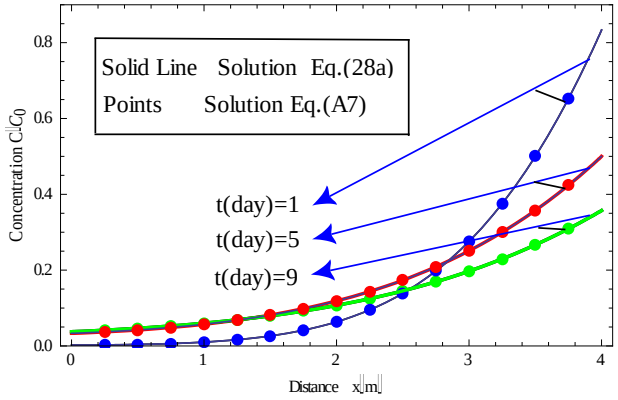

Fig. 5(a). Distribution of dimensionless concentration for various times $(0 \le t \le t_0)$

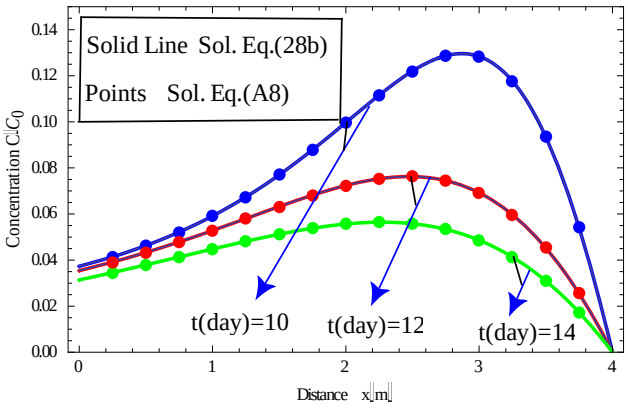

Fig. 5(b). Distribution of dimensionless concentration for various time $(t_0 < t)$

5. Conclusion

Solution of finite domain theoretical model comprising temporal dispersion and seepage velocity with any time dependent smoothly varying input of pulse type applied against the flow has been obtained. Such solution is well applicable for real world finite domain aquifers for predicting contaminant variations in presence and in absence i.e. in other word during rehabilitation process when source is eliminated. The generalization of the input source added the worth of solution. Laplace Transformation Technique and interpolation method are applied to obtained the solution. The Accuracy of solution enhances with optimum selection of interpolation polynomial method.

Acknowledgements

This research did not receive any specific grant from funding agencies in public, commercial or non-profit sectors.

References

[1] L. F. Konikow, D. J. Goode, "Apparent dispersion in transient groundwater flow", Water Resources Research, vol. 26 (10), pp. 2339–2351, 1990.

[2] K. Huang, M. Th. van Genuchten, and R. Zhang, "Exact solutions for one dimensional transport with asymptotic scale-dependent dispersion", Appl. Math .Model., vol. 20, pp. 298-308, 1996.

[3] S. J. Watson, D.A. Barry, R.J. Schotting, S.M. Hassanizadeh,"Validation of classical density-dependent solute transport theory for stable, high-concentration-gradient brine displacements in coarse and medium sands", Advances in Water Resources, vol. 25 (6), pp. 611–635,2002.

[4] V. Batu, "A generalized two-dimensional analytical solution for hydrodynamic dispersion in bounded media with the first-type boundary condition at the source", Water Resour. Res., vol. 25, pp. 1125-1132, 1989.

[5] A. K. Verma, S. M. Bhallamudi and V. Eswaran , "Overlapping Control Volume Method for Solute Transport.", J. Hydrol. Eng., vol. 5(3), pp. 308-316, 2000.

[6] M. Jang, J. Lee, J. Choe, and J. M. Kang, "Modeling of solute transport in a single fracture using streamline simulation and experimental validation.", J.Hydrol., vol. 261, pp.74-85, 2002.

[7] M. Massabo, R. Cianci, and O. Paladino, "Some analytical solutions for two dimensional convection-dispersion equation in cylindrical geometry", Environ. Modell. Softw., vol. 21 (5), 681-688, 2006.

[8] D. K. Jaiswal, A. Kumar, N. Kumar, R. R. Yadav, "Analytical solutions for temporally and spatially dependent solute dispersion of pulse type input concentration in one-dimensional semi-infinite media", Journal of Hydro–environment Research, vol. 2, 254–263, 2009.

[9] D. K. Jaiswal, A. Kumar, "Analytical solutions of advection-dispersion equation for varying pulse type input point source in one-dimension" , International Journal of Engineering, Science and Technology , vol. 3(1), pp. 22-29, 2011.

[10] R. R. Yadav and L. K. Kumar, "One-dimensional spatially dependent solute transport in semi-infinite porous media: an analytical solution", International Journal of Engineering, Science and Technology, vol. 9, (4), pp. 20-27, 2017.

[11] M. K. Singh and P. Das, "Scale Dependent Solute Dispersion with Linear Isotherm in Heterogeneous Medium", J. Hydrology (Elsevier) , vol. 520, pp. 289-299, 2015.

[12] V. K. Bharati, A. Sanskrityayn, N. Kumar, "Analytical Solution of ADE with Linear Spatial Dependence of Dispersion Coefficient and Velocity using GITT", Journal of Groundwater Research, vol. 3, 4/1, 2015.

[13] C. Liu, W. P. Ball and J. HughEllis. "An Analytical Solution to the One-Dimensional Solute Advection-Dispersion Equation in Multi-Layer Porous Media", Transp.in Porous Med., vol. 30, pp. 25-43, 1998.

[14] N. K. Mahato, S. Begam, P. Das, and M. K.Singh, "Two-dimensional Solute Dispersion Along and Against the Unsteady Groundwater Flow in Aquifer" ,Journal of Groundwater Research, vol.3, 4/1, 2015,.

[15] A. Sanskrityayn, H. Suk, N. Kumar, "Analytical solutions for solute transport in groundwater and riverine flow using Green's Function Method and pertinent coordinate transformation method",Journal of Hydrology, vol. 547, pp. 517-533, 2017.

[16] K. I. Hamz, "Numerical Solution of the Two-Dimensional Time-Dependent Transport Equation,Second International Conference on Saltwater Intrusion and Coastal Aquifers— Monitoring, Modeling, and Management", Mérida, México, March 30-April 2, 2003.

[17] K. Rajsekhar, P. K. Sharma and S. K. Shukla "Numerical modeling of virus transport through unsaturated porous media", Cogent Geosciences, vol. 2, 2016.

[18] R. R. Yadav, D. K. Jaiswal and and Gulrana, "Analytical Solution for Solute Transport in One-Dimensional Porous Media with a Periodic Boundary Condition" International Journal of Pure and Applied Mathematical Sciences, vol. 5 (1-2), pp. 1-13, 2011.

[19] D. K. Jaiswal, R. R. Yadav, and Gulrana, "Solute-Transport under Fluctuating Groundwater Flow in Homogeneous Finite Porous Domain", J Hydrogeology Hydrologic Engineering , vol. 2:1, 2013.

[20] J. Bear, "Dynamics of fluids in porous media", American Elsevier, New York, 1972.

[21] J. Crank, "The Mathematics of Diffusion", Oxford Univ. Press, London, 2nd ed. ,1975

[22] D. K. Todd, "Groundwater Hydrology", John Wiley, New York, USA, 1980.

Appendix:

The input boundary conditions with $F(m't)=1/(1+m't)$ may be described as;

Assuming $m'=m$ in particular, we have following initial and boundary condition:

$$c(x,t)=c_i\sinh(\alpha x);\ L_1\le x\le L,\ t=0 \quad \text{(A1)}$$

$$c(x,t)=\begin{cases} c_0/(1+mt);\ 0<t\le t_0 & \text{(A2a)} \\ \qquad\qquad ;\ x=L & \\ 0\ ;\ t>t_0\,, & \text{(A2b)} \end{cases}$$

$$\frac{\partial c(x,t)}{\partial x}=\frac{u_0}{2D_0}c \text{ at } x=L_1,\ t\ge 0 \quad \text{(A3)}$$

With transformation Eq. (10) may written as:

$$c(x,T)=c_i\sinh(\alpha x);\ L_1\le x\le L,\ T=0 \quad \text{(A4)}$$

$$\begin{cases} c_0\exp(-mT)\ ;\ 0<T\le T_0 & \text{(A5a)} \end{cases}$$

$$c(x,T) = \qquad x = L$$

$$0 \;;\; T > T_0 \qquad \text{(A5b)}$$

$$\frac{\partial c(x,T)}{\partial x} = \frac{u_0}{2D_0} c \text{ at } x = L_1,\ T \geq 0 \text{ (A6)}$$

Now, performing same steps as Eq.(15) to Eq.(27) then taking inverse laplace transform , solution may be written as:

$$c(x,T) = \left[\exp(-\beta L) F_{-1}(x,T) + \frac{c_i}{2} \{ I_\alpha(x,T) - I_{-\alpha}(x,T) \} \right]$$

$$\times \exp\left[\frac{u_0}{2D_0} x - \frac{{u_0}^2}{4D_0 R_0} T \right]$$

$$;\ 0 < T \leq T_0 \text{ (A7)}$$

$$c(x,T) = \left[\exp(-\beta L) \left[\begin{matrix} F_{-1}(x,T) - F_{-1}(x,T-T_0) \times \\ \exp\{(\eta^2 - m) T_0\} \end{matrix} \right] + \right.$$

and

$$\left. \frac{c_i}{2} \{ I_\alpha(x,T) - I_{-\alpha}(x,T) \} \right] \times \exp\left[\frac{u_0}{2D_0} x - \frac{{u_0}^2}{4D_0 R_0} T \right]$$

$$;\ T_0 \leq T \text{ (A8)}$$

where,

$$\eta_{-1} = \sqrt{\eta^2 - m}$$

***

Mathematical Model of the Traveling Salesman Problem with Delivery and Draft Limit

Kadir Mersin*, Cemile Nur**

International Logistics and Transportation, Faculty Of Economics, Administrative And Social Sciences

Istanbul Gelisim University 34315 Avcilar, Istanbul, Turkey

**Computer Engineering, Engineering Faculty, Yalova University,

(kmersin@gelisim.edu.tr, cemile_nur@yahoo.com)

‡ Corresponding Author; Kadir Mersin Istanbul Gelisim University 34315 Avcilar, Istanbul, Turkey

+90 212 422 7000

kmersin@gelisim.edu.tr

Received: 07.05.2019 Accepted:26.05.2019

Abstract-In this paper, we determine the order of the ports to be reached with the help of graph theory and establish Hamilton cycles. We obtain sub-solutions and solution sets with the help of these cycles. Moreover, we prove some relations about the draft limit and the demand of the port. Finally we present some examples**.**

Keywords Traveling Salesman Problem, Draft Limit, Maritime Transportation.

1. Introduction

In maritime transportation, to determine the optimal route has a crucial importance. Many constraints affect the optimal route. Therefore, there are many works about determining the most optimal route in maritime transportation. One of the most interesting approaches is to transform the ship routing problem into the traveling salesman problem. Maritime routing and scheduling, draft limits have been considered in a lot of papers. For example Hennig [6], Song and Furman [10], Christiansen et al.(2011) but draft limit was not the main subject. The other area is vehicle routing problem. Several problems was described by combining routing and loading problems. Petersen and Madsen [8], Felipe et al.[5], Erdogan et al.[4] Cordeau et al.[2], Iori and Martello [7], Fagerholt and Christiansen [3] but none of them considered draft limit as a constraint. Finally Rakke J. et al.[9] approached this situation from a different perspective and transform this problem into travelling salesman problem. They built a model by accepting the ports as vertices.

The draft of a vessel is the distance between the water level and the base of the vessel. The draft limit is the height from the seabed to the water level. Each port has a draft limit. This means that vessels with values above a certain draft cannot enter the port. Some ports have low draft limits, causing the arriving vessels to run aground. For example, since the Kota Kinabalu bulk freight port in Malaysia has a draft limit of 9.2 meters, it is impossible for a fully loaded Panamax to reach the port with draft of about 12 meters. In this paper, we further develop a model and obtain sub-solution sets. We find the number of Hamilton cycles to be generated and in this way we obtain solution sets and develop a new approach. Moreover, we prove some relations about the draft limit and the demand of the port. (See Proposition 1, Proposition 2, Proposition 3, Corollary 1 and Corollary 2) Finally we present some examples. We are interested only in the delivery case of the vessels.

2. Graph Theory

A graph G is an ordered pair (V,E), where V is some set and E is a set of 2-point subsets of V. The elements of the set V are called vertices of the graph G and the elements of E edges of G. The number of edges of G containing the vertex v is denoted by the symbol deg(v) or |v|. The number deg(v) is called the degree of v in the graph G. A graph G is connected if there is a path between any two of its vertices. A graph G is said to be complete if every vertex in G is connected to every other vertex in G. Thus a complete graph G must be connected. The complete graph with n vertices is denoted by Kn. G and G' are called subgraph of K_n , If K_n=G∪G' . And G' is called complement of G.

A graph is said to be traversable if it can be drawn without any breaks in the curve and without repeating any edges, that

is, if there is a path which includes all vertices and uses each edge exactly once. Such a path must be a trail (since no edge is used twice) and will be called a traversable trail. A Hamiltonian circuit in a graph G is a closed path that visits every vertex in G exactly once. (Such a closed path must be a cycle.) A graph G is called an Eulerian graph if there exists a closed traversable trail, called an Eulerian trail. If G does admit a Hamiltonian circuit, then G is called a Hamiltonian graph. There is no sufficent and necessery condition to have Hamilton circuit for any graph.

3. Draft Limit

Draft of a ship is the vertical distance between waterline and the bottom of the hull or keel. Every ports have a draft limit. It means, the vessels which has greater draft than the draft of a port, is not able to berth. The draft of a ship is depend on the weight on board so we can assume that draft limit is a function of the weight.

Let l_i, m_{l_i} and n_{l_i} be the port to be visited, the draft of the vessel at l_i port (when entering) and the draft limit of l_i port, respectively, where i=1…k We can write the draft as a function of the load, since the draft of the vessel is related to the load it carries. Based on the assumption that the amount of water sinking is 1 cm per TEU, we define the draft of the vessel (in terms of meters) as follows:

$$m_{l_i} = m_{l_i}(x_{l_i}) = m_0 + \frac{x_{l_i}}{100} \quad \forall i = 1 \dots k$$

where m_0 is the initial draft of the vessel without any load but with full fuel and x_{l_i} is the amount of load (in terms of TEU) on the vessel when entering l_i, port.

It is clear that the draft limit of the port should be greater than the draft of the vessel, i. e.,

$$m_{l_i} \geq n_{l_i} \forall i = 1 \dots k$$

Note that, since the fuel of the vessel decreases as it moves, there will be a small reduction in the initial draft of the vessel m_0. Therefore, the draft of the vessel m_{l_i} at l_i port also decreases in small amounts as it moves. Without loss of generality we assume that

$n_{l_i} \geq n_{l_{i+1}} \forall i = 1 \dots k$ if $\{l_1, l_2, \dots . l_k\}$ is the set of ports. For convenience, we use the pair $< n_{l_i}, d_{l_i} >$ where d_{l_i} is the draft effect of the demand of l_i port (in terms of meters). Since there is no delivery at the initial port l_1, we have $d_{l_1} = 0$. It is clear that, in order for the ship to be able to enter the port, the draft limit of the port should be greater than the draft effect of the total load onboard. In other words,

$$\exists n_{i_0} \ni \sum_{i=0}^{k} d_{l_i} \leq n_{l_{i_0}} \quad , i_0 \in \{1,2, \dots , k\}$$

where d_{l_0} is the draft effect of the empty ship with full fuel.

Our aim is to establish an appropriate Hamilton cycle, considering each port as a vertex, according to the draft limits and demands of the ports for the amount of cargo loaded on the vessel. A Hamilton cycle is a path through a graph that starts and ends at the same vertex and visits every other vertex exactly once. If there is a Hamilton cycle containing all the ports $\{l_1, l_2, \dots . l_k\}$, then we say that this set is a solution set. If there is no Hamilton cycle containing all ports, then we break down the graph into the subgraphs containing Hamilton cycles and we say that each subgraph forming a Hamilton cycle is a sub-solution set. For every partition i we denote this sub-solution set by S_i. If there are t partitions then we have

$$S = \bigcup_{i=1}^{t} S_i$$

and the most appropriate partition is the chain $|S_1| \geq |S_2| \geq \cdots \geq |S_t|$ where $|S_i|$ denotes the number of elements of the set S_i. The number of partitions gives us the number of vessels we need for shipment.

Let W_{l_i} be the draft effect of the load on the vessel when entering l_i port. Clearly, if S=$\{l_1,l_2,\dots .l_k\}$ is a solution then

$$W_{l_1} = \sum_{i=1}^{k} d_{l_i}$$

$$W_{l_{i+1}} = W_{l_i} - d_{l_i} \forall i = 1 \dots k-1$$

If $\hat{S} = \{l_1, l_2, \dots . l_r\}$ is a subsolution then

$$W_{l_{i+1}} = W_{l_i} - d_{l_i} \forall i = 1 \dots r-1$$

where r≤k. If r=k then $\widehat{(\hat{S})} = \dot{S}$

Now we state some of our main results. From now on, we assume that the draft effects of the empty vessel and fuel are included in the draft effect of the total load onboard.

Proposition 3.1. Let Wi be the amount of the cargo on board while berthing the port of i. If $W_1 = \sum_{i=1}^{k} n_i$ and $W_i = W_{i-1} - n_{i-1}$; ∀i∈{2,3,…,r} then

$\tilde{S}=\{p_1, p_2, p_3, \dots p_r\}$ is a sub-solution. Moreover, if r=k, then S= $\tilde{S}$

Proposition 3.2. S= $\tilde{S}$ holds if and only if $L_i \leq m_i$

Proof: Straight forward.

Proposition 3.3. Number of port which has same demand and draft limit is at most 1.

Proof: Let ⟨m | m⟩ and ⟨n | n⟩ are two ports in solution set. So, amount of the cargo on board is n+m+k (k>0). In this condition vessel can not berth these two ports. The ship has to transport n+m+k+1 cargo to berth ⟨m | m⟩ and ⟨n | n⟩ but this is contradiction. Because we assume that the amount of the cargo is m+n+k.

Definition 3.5. Let x be a real number then [x] is the maximum integer which is less than x. We will define a function which is called nearest integer function;

f(x):R→Z

f(x)=[x]

Proposition 3.6. Let ⟨m | n⟩ be the draft limit-demand pair. Then the number of the port which has the same draft limit-demand pair is less than [m/n].

Proof: Let number of ⟨m | n⟩ pair is "k" in the solution set. Then, amount of the cargo on board is at least k.n pieces and k.n can not be greater than draft limit because ports belong to solution set. So k.n<m is hold.

Then $k \leq \frac{m}{n}$ and the greatest integer is $\left[\frac{m}{n}\right]$ which holds the inequality.

Proposition 3.7. Let ⟨m | n⟩ be the draft limit-demand pair. Then the maximum number of the port which has the same demand is $\left[\frac{\max\{m_i\}}{n}\right]$.

Proof: Straightforward.

Corollary 3.4. The graph does not have Hamilton circuit if the number of ports which have same draft limit-demand pair is more than one. Than, the number of sub-solutions are equal the number of ports which have this property.

Corollary 3.5. If the number of ports which have same draft limit-demand pair ⟨m | n⟩ is greater than [m/n], corollary 2.9 is provided.

4. Mathematical Modelling

First we should assign a decision parameter ε_{ij} to form the modelling. This parameter will show that which two elements of the set consisting of the ports as vertices are in the solution set. The decision parameter is defined as follows:

$$\varepsilon_{l_i l_j} = \begin{cases} 1, & if\ there\ is\ a\ path\ connecting\ l_i\ and\ l_j\ ports \\ 0, & otherwise \end{cases}$$

If there are t Hamilton cycles that are formed to find the solution set, then our modelling is as follows:

$$\sum_{l_i \in S_r} \varepsilon_{l_i l_j} = 1\,;\ l_j \in S_r \quad (1)$$

$$\sum_{l_j \in S_r} \varepsilon_{l_i l_j} = 1\,;\ l_i \in S_r \quad (2)$$

$$\sum_{l_i \in S_r} W_{l_i l_1} = 0\ ;\ \sum_{l_j \in S_r} W_{l_1 l_j} = \sum_{l_i \in S_r} d_{l_i} \quad (3)$$

$$0 \leq W_{l_i l_j} \leq n_{l_j} . \varepsilon_{l_i l_j} \quad (4)$$

$$\sum_{j=1}^{i-1} \varepsilon_{l_j l_i} = \sum_{j=i+1}^{k} \varepsilon_{l_i l_j}\ ; \quad (5)$$

$$l_i, l_j \in S_r\ ; |S_r| \leq k\ , \varepsilon_{l_i l_j} = \varepsilon_{l_j l_i} = 0\,;$$

$$(l_i, l_j) \notin S_r \times S_r \quad (6)$$

$$\bigcup_{r=1}^{t} S_r = S \quad (7)$$

$$\bigcap_{r=1}^{t} S_r = \{l_1\} \quad (8)$$

where r = 1,2,… t and $W\_(l_i l_j)$ denotes the draft effect of the total load onboard when the vessel goes from $l_i\ to\ l_j$. In this modelling (1) and (2) express that the degree of each port is 1 in the cycle created .The condition (3) states that the ship returns to the initial port l_1 empty and has enough load to reach all the ports in the solution set at the initial port l_1. (4) indicates that the load onboard is suitable for the draft limit of the arrival port. (5) means that the ship visits again none of the visited ports from sub-solutions. Finally, (6), (7), and (8) indicate that the initial port is common to all sub-solutions and that the union of all sub-solutions is equal to the solution set.

Example 1 Let us consider the following table.

Table 1. Ports with draft limits

Port	Demand (TEU)	Draft Limit (meters)
X	0	16
A	300	11
B	300	11
C	400	13
D	200	18
E	300	10

In the table 1 above, for a ship with the initial port X, the demands and the draft limits of the ports to be visited are given. Let us create a Hamilton cycle containing these ports based on the assumption that the amount of sinking water per TEU is 1 cm.

First we need to create the draft limit-the draft effect of the demand pairs, i.e. $\langle l_i \mid d_j \rangle$ pairs.

X: $\langle 16 \mid 0 \rangle$

A: $\langle 11 \mid 3 \rangle$

B: $\langle 11 \mid 3 \rangle$

C: $\langle 13 \mid 4 \rangle$

D: $\langle 18 \mid 2 \rangle$

E: $\langle 10 \mid 3 \rangle$

In accordance with our acceptance, the ship has to return to its starting port empty only by delivering. First of all, if we examine the draft limit-the draft effect of the demand pairs, we see that the ports A and B have the same pair. If there is a solution set, then the number of the ports with the pair $\langle 11 \mid 3 \rangle$ will be at most 3 according to Proposition 2. There is therefore a possibility that there exists a Hamilton cycle. In other words, there is a possibility that our solution set is unique. When we look at our example, the only port is D which the ship can go from the X port. Then the second vertex of the Hamilton cycle will be the port D. When leaving the port D, the total amount of demand on the ship will be 1300 TEU. In this case, the only port to go is the port C. Since the draft limit is equal to the draft effect of the total demand, there is a possibility that the ship may run aground, but the amount of fuel consumed on the road will reduce the draft of the ship so that the ship will be able to enter the port easily. We can take the port C as the third vertex of the Hamilton cycle. The total demand on the ship when leaving the port C is 9000 TEU. This means that the ship will be able to enter every port with a draft limit of more than 9 meters. Since the draft limits of all ports in the table are greater than 9 meters deep, there is no obstacle to establish the Hamilton cycle. In total 3! = 6 solution sets (Hamilton cycles) can be established for the 3 ports left. One of the solution sets is

X →D→ C→ A→ B

Thus, only one ship will be sufficient for delivery. The matrix representation of this graph is given in Figure 1.

$$\begin{bmatrix} 0 & 1 & 0 & 0 & 0 & 0 \\ 0 & 0 & 1 & 0 & 0 & 0 \\ 0 & 0 & 0 & 1 & 0 & 0 \\ 0 & 0 & 0 & 0 & 1 & 0 \\ 0 & 0 & 0 & 0 & 0 & 1 \\ 1 & 0 & 0 & 0 & 0 & 0 \end{bmatrix}.$$

Figure1. Matrix representation of example 1

Note that, if $\{l_1, l_2, \ldots . l_k\}$ is a solution set, then the matrix representation of the graph $l_1 \rightarrow l_2 \rightarrow \cdots \rightarrow l_k \rightarrow l_1$ is given in Figure 2.

$$A_{k\times k} = \begin{bmatrix} 0 & 1 & 0 & 0 & \cdots & 0 \\ 0 & 0 & 1 & 0 & \cdots & 0 \\ \vdots & \vdots & \ddots & \ddots & \ddots & \vdots \\ 0 & 0 & \cdots & 0 & 1 & 0 \\ 0 & 0 & 0 & \cdots & 0 & 1 \\ 1 & 0 & 0 & 0 & \cdots & 0 \end{bmatrix}.$$

Figure 2. Matrix representation of solution set.

It is clear from this matrix that $a_{j,j+1} = a_{k,1} = 1$ and the other components of the matrix are zero, for j=1,2,…k+1

Example 2 Let the following table be given in Table 2.

Table 2. Ports with draft limits-2

Port	Demand(TEU)	Draft Limit (meters)
X	0	25
A	200	9
B	300	14
C	200	9
D	200	9
E	300	17
F	800	8
G	200	11
H	200	9

In the table 2, there are 5 ports with the same demand, 200 TEU, and also there are 4 ports with the same $\langle n_{l_i} \mid d_{l_i} \rangle$ pair, $\langle 9 \mid 2 \rangle$ Moreover, there is a port such that $n_{l_i} = d_{l_i}$. Clearly, there is no Hamilton cycle containing all ports according to the draft limits. For this reason, we need more than one ship. First, we sort the ports according to the draft limits as follows:

$$X : l_1;\ E : l_2;\ B : l_3;\ G : l_4;$$

$$A : l_5;\ C : l_6;\ D : l_7;\ H : l_8;\ F : l_9$$

Let us consider the partitions

$$S_1 = \{l_1, l_2, l_3 l_4 l_9\}$$

$$S_2 = \{l_1, l_5, l_6 l_7 l_8\}$$

It is clear that, there are Hamilton cycles for both S_1 and S_2 and therefore S_1 and S_2 are sub-solution sets. Hence it is necessary two ships for delivery. Another possible partitions are given in Table 3

Table 3. Sub-solutions sets

$S_1 = \{l_1, l_2, l_3 l_4 l_9\}$ $S_2 = \{l_1, l_5, l_6 l_7 l_8\}$ (we built)	$S_1 = \{l_1, l_4, l_5 l_6 l_7 l_8\}$ $S_2 = \{l_1, l_2, l_3 l_9\}$
$S_1 = \{l_1, l_3, l_5, l_6, l_7, l_8\}$ $S_2 = \{l_1, l_2, l_4, l_9\}$	$S_1 = \{l_1, l_2, l_4, l_5, l_6, l_7, l_8\}$ $S_2 = \{l_1, l_3, l_9\}$
$S_1 = \{l_1, l_2, l_5, l_6, l_7, l_8\}$ $S_2 = \{l_1, l_3, l_4, l_9\}$	$S_1 = \{l_1, l_2, l_3, , l_5, l_6, l_7, l_8\}$ $S_2 = \{l_1, l_4, l_9\}$
$S_1 = \{l_1, l_3, l_4, l_5, l_6, l_7, l_8\}$ $S_2 = \{l_1, l_2, l_9\}$	$S_1 = \{l_1, l_2, l_3, l_4, l_5, l_6, l_7, l_8\}$ $S_2 = \{l_1, l_9\}$

Since there are many route options, the most optimal route can be selected by considering the distance. Note that, for each partition including the ports A, C, D and H, there are 4! = 24 route options since they have the same $\langle 9 \mid 2 \rangle$ pair. In total, there are 24x8 = 192 route options according to the draft limits.

5. An algorithm for the optimal route

It can be seen from Example 2 that there are many route options according to the draft limits. Now we give an algorithm for the optimal route in terms of the cost of the route and draft limit. For this, we use the nearest neighborhood algorithm. (Anderson, 2000)

Step1. Sort the ports according to the draft limits from large to small. The initial port will be l_1 and $n_{l_i} \geq n_{l_{i+1}}$ ∀i=1,2,…k-1, for the set of ports $\{l_1, l_2 \ldots l_k\}$

Step2. For t Hamilton cycles, in other words, for t ships for delivery, each ship goes to the nearest convenient (according to the draft limits) port which has the lowest cost from the initial port l_1.

Step3. Each ship goes to another convenient port which has the lowest cost from the second port if any, otherwise the ship returns to the initial port l_1.

Step4. Repeat Step3 until there are no ports left.

In this paper, we have determined the order of the ports to be reached with the help of graph theory and have established Hamilton cycles. We have obtained sub-solutions and solution sets with the help of these cycles and have developed a new approach. Also, we have developed a modelling by the traveling salesman problem with draft limits. We have found the number of Hamilton cycles to be generated and in this way we have determined the number of vessels we need for shipment. Moreover, we have proved some relations about the draft limit and the demand of the port which gives an idea for the optimal route of the ship. Finally we have presented some examples.

References

[1] Battara, M. Erdogan, G., Laporte G., jestvang, Vigo, D. “The Traveling Salesman Problem with Pickups, Deliveries, and Handling Costs Transportation Science, 44(3): 383-99 2010

[2] Cordeau, J-F, Iori, M., Laporte, G., Salazar Gonzalez, JJ. “A branch and cut algorithm for the pickup and delivery traveling salesman problem with LIFO loading.” Networks ; 55(1):46-59, 2010

[3] Fagerholt, K. and Christiansen, M. “A traveling salesman problem with allocation, time window and precedence constraints - an application to ship scheduling.” International Transactions in Operational Research, 7 , 231-244., 2000

[4] Erdogan, G., Cordeau, J-F., Laporte G. “The pickup and delivery traveling salesman problem with firs in first out loading.” Computers & Operations Research,; 36(6):1800-8, 2009

[5] Felipe, A., Ortuno, MT., Tirado, G. “The double traveling salesman problem with multiple stacks: a variable neighborhood search approach.” Computers & Operations Research,; 36(11):2983-93, 2009

[6] Henning, F. “Optimization in maritime transportation: crude oil tanker routing and scheduling.” PhD thesis. Norwegian University of Science and Technology, 2010

[7] Iori, M., Martello, S. "Routing problems with loading constraints." TOP; 18(1):4-27, 2010

[8] Petersen, HL., Madsen OBG. "The double traveling salesman problem with multiple stacks-formulation and heuristic solution approaches." European Journal of Operational Research ;198(1):139-47, 2009

[9] Rakke, J. G., Christiansen, M., Fagerholt, K. and Laporte, G. "The traveling salesman problem with draft limits." Computers & Operations Research, 39 (9) , 2161-2167., 2012

[10] Song J-H, Furman, KC. "A maritime inventory routing problem: practical approach." Computers& Operations Research, doi: 10.1016/j.cor.2010.10.031

INTERNATIONAL JOURNAL of ENGINEERING TECHNOLOGIES-IJET
Niş, Vol.5, No.2, 2019

The Compressive Strength Development of Alkali Activated Fly Ash/Slag Concretes with Different Alkali Activator Ratios

Anıl Niş* ‡

* Department of Civil Engineering, Faculty of Engineering and Architecture, Istanbul Gelisim University, Istanbul, Turkey (anis@gelisim.edu.tr)

‡ Corresponding Author, Anıl Niş, Department of Civil Engineering, Istanbul Gelisim University, Istanbul, Turkey

Tel: +90 212 422 7020, Fax: +90 212 422 7401, anis@gelisim.edu.tr

Received: 14.05.2019 Accepted:24.06.2019

Abstract- Recently, geopolymer or alkali-activated concrete takes great attention due to low carbon footprint since fly ash and ground granulated blast furnace slag (industrial by-product materials) has been utilized as binder materials in the alkali-activated concrete. In this research, the compressive strength (CS) development of the alkali-activated fly ash/slag (AAFAS) concrete was investigated in an ambient environment at 7., 14., 28., and 56. days using alkali activator (sodium silicate to sodium hydroxide) ratios of 1, 1.5, 2, and 2.5 with 6M SH (low) concentration. In addition, the effect of delayed oven-curing condition was also studied at 56.day. The results indicated that for the ambient-cured specimens with 6M SH concentration, the maximum and minimum CS were reached in the AAFSS concrete with alkali activator (SS/SH) ratios of 2 and 1, respectively. The AAFAS concrete with an alkali activator ratio of 2.5 showed the lowest CS enhancement after 7.day and 14.day, while the AAFAS specimens with an alkali activator ratio of 1.5 performed the least CS improvement at 28.day in the ambient environment. Meanwhile, the highest CS enhancement was observed in the specimens with an alkali activator ratio of 2 for all ages. Due to the delayed oven-curing, the least and the highest CS enhancements were observed in the AAFAS specimens with alkali activator ratios of 2 and 1.5, respectively. The results pointed out that AAFAS concrete with a higher alkali activator ratio (≥2) should be used for structural applications in the ambient environment.

Keywords Alkali activated fly ash/slag concrete, alkali activator, delayed oven-curing, compressive strength, sodium silicate to sodium hydroxide ratio.

1. Introduction

Due to the increasing population, novel eco-friendly materials are required in order to build sustainable structural applications. Nowadays, ordinary Portland cement (OPC) has been widely utilized as a binder material for the construction of structural elements. However, due to the hazardous influence of the cement material to the environment and high energy demand during cement production [1], alternative binder materials or different concrete types become necessary for the green and sustainable environment and global economy. Generally, fly ash (FA), ground granulated blast furnace slag (GGBS) and silica fume have been partially utilized instead of OPC as binder materials and their favorable effects on the mechanical strength and durability properties of the OPC concrete were reported in the earlier investigation [2]. Recently, geopolymer concrete or alkali-activated concrete, a new type of cementless free concrete, has been emerged into the concrete industry and numerous researches have been conducted in order to use geopolymer or alkali-activated concrete instead of OPC concrete in structural applications [3-7]. A novel cement-free alkali-activated concrete needs less energy during its production [8] and releases approximately 6 times less CO2 than the OPC concrete [9, 10]. Alkali activated concretes includes FA, GGBS, metakaolin, silica fume as binder materials [11] and generally SS and SH were utilized as alkali activators for the geopolymerization reactions [12, 13].

The alkali-activated concretes with FA show slow geopolymerization reactions at the ambient environment and generally requires elevated temperature curing above 60°C for the fast geopolymerization reactions and early strength gain [14]. Therefore, the FA utilization alone can be limited in the precast concrete industry due to the heat-curing requirement. Meanwhile, GGBS consists of a high amount of

CaO that responsible for the strength gain at ambient environment. Therefore, GGBS utilization in the AAFAS concrete becomes significant for the structural applications. However, researchers reported that GGBS utilization alone causes high shrinkage and rapid setting [15, 16], hence combined utilization of the FA and GGBS should be better in terms of structural utilization of the AAFAS concrete specimens.

Alkali activators are responsible for the initiation of the geopolymerization reactions. A strong alkaline medium is required for the surface hydrolysis and molarity concentration of the alkali activator determines the mechanical properties of the AAFAS materials [17]. In an earlier investigation [18], the effect of three different SH molarity (3M, 6M, 9M) was investigated on the FA based geopolymer concrete when the alkali activator ratio (SS/SH ratio) was kept constant and it was reported that the highest CS was obtained on the specimens with 6M SH concentration. The researchers also added that geopolymerization reaction was not strong due to the low SH concentration (3M) and premature coagulation of silica, which causes low CS for the AAFAS concrete specimens with a high molarity concentration (9M). The 6M SH was found as the optimum molarity concentration for the FA based geopolymer concrete.

The inclusion of the SS to the SH solution improved the mechanical strength of the alkali-activated materials since SS increases the silicate content and SiO2/Na2O ratio in the alkali activator [19]. It was reported that the CS of the alkali-activated materials depends on the SH molarity, SS/SH, SiO2/Na2O, and Na2O/Al2O3 ratios [20]. In this study, the effect of various SS/SH ratios under 6M SH concentration on the CS development of the AAFAS concrete was investigated. Moreover, the effect of the delayed oven-curing condition on the CS of the AAFAS concrete was examined.

2. Materials and Test Methods

2.1. *Alkali Activated Concrete Materials*

The AAFAS concrete consisted of 50% GGBS and 50% F-type FA. The GGBS and FA materials were taken from Iskenderun iron and steel power plant and Çatalağzı thermal power plant, respectively. For the geopolymerization process, combined use of SS and SH solutions were utilized with alkali activator ratios of 2.5, 2, 1.5, and 1 with the 6M SH concentration. The SH pellets and SS liquid with an alkaline modulus of 2 and a specific gravity of 1.39 g/cm3 were taken from a local market. The 6M SH solution and different alkali activator ratios were prepared in the laboratory environment just before the AAFAS concrete production. The sudden heat release emerged during mixing of the SH solution, hence SH solution was waited approximately 15 minutes in order to cool down. A naphthalene based superplasticizer was utilized to reach S4 slump class concrete for structural utilization. For the aggregates, coarse aggregates (5mm – 22mm) and fine aggregates (<4 mm) were used and the aggregate sieve result was given in Fig. 1. The chemical composition and physical properties of the used binder materials were also presented in Table 1.

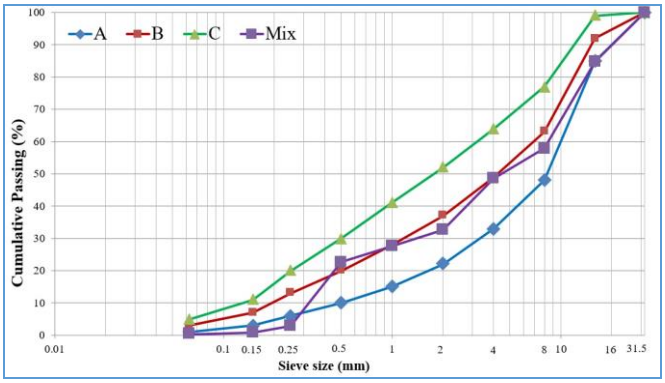

Fig. 1. Aggregate sieve analysis

Table 1. The physical properties and chemical composition of the slag and fly ash

Chemical Composition	Slag	F-type Fly Ash
SiO_2 (%)	37.97	56.15
Al_2O_3 (%)	13.27	26.37
CaO (%)	37.92	1.79
Fe_2O_3 (%)	1.16	6.44
MgO (%)	5.64	2.35
SO_3 (%)	0.23	0.056
Na_2O (%)	0.84	1.1
K_2O (%)	0.56	3.8
Cl (%)	0.015	0.09
Loss on ignition (%)	0.01	2.2
Specific Gravity (g/cm^3)	2.95	2.05
Specific Surface (cm^2/g)	5131	3870

2.2. *Mixture Composition*

Table 2 indicates the mixture composition of the AAFAS concrete with various alkali activator ratios. For the production of the AAFAS concrete, 180 kg/m3 slag (half of the binder) and 180 kg/m3 F-type FA materials were utilized. The used alkali activator ratios were 1, 1.5, 2, and 2.5 and the concentration of the SS was 6M, which was considered to be low molarity concentration. The compressive strength development of the AAFAS concrete under low SH molarity was investigated in this research. For enhanced geopolymerization and workability, and especially cheaper alkali activated concrete productions, water addition into the alkali-activated concrete mixes was reported in the earlier investigations [21, 22]. The used water amount was kept constant for the all AAFAS concrete mixtures, and the superplasticizer amount was changed in order to obtain S4 slump class concrete. It should be noted that the used superplasticizer (SP) amount in the AAFAS specimens decreased as the alkali activator (SS/SH) ratio increased as shown in Table 2.

Table 2. Mixture composition of the AAFAS concrete with different SS/SH ratios

Mixture	SS/SH ratios			
	1	1.5	2	2.5
6M SH	81	64.8	54	46.3
SS	81	97.2	108	115.7
Fly ash	180	180	180	180
Slag	180	180	180	180
No I	560	560	560	560
No II	560	560	560	560
Crushed Sand	373	373	373	373
Sand	373	373	373	373
Superplasticizer	11.56	10.00	8.44	6.88
Water	43.75	43.75	43.75	43.75

During mixing procedure, dry materials (aggregates, FA and GGBS) were included into the mixer and the dry mixture mixed for 2 min. The SS, SH and half of the SP were mixed before in a container and included into the mixer and then mixed for additional 2 min. Finally, water and the remaining SP were also mixed before in a container and the liquid solution was added into the mixer and mixed for additional 2 min. The duration of the total mixing procedure was 6 min.

2.3. *Curing of specimens and compressive strength tests*

The prepared different AAFAS mixes were poured into the 150x150x150 mm cube molds and the required compaction was realized. Then the top surfaces of the cube AAFAS concretes were covered with plastic sheets to prevent the evaporation of the alkaline solutions. After 3 days later, molds were demolded and AAFAS concretes were left in the ambient environment at 6 ± 4°C to investigate the CS development of the AAFAS concretes in winter conditions. The CS tests were performed according to ASTM C39 standard at the ages of 7., 14., 28., and 56. days in order to observe the CS enhancement of the ambient-cured AAFAS concrete specimens with curing time. Three identical AAFAS samples were utilized for each AAFAS specimen in order to calculate average CS of the AAFAS specimens.

In addition to ambient-curing, the delayed oven-curing was also applied to the AAFAS concrete specimens in order to investigate the influence of delayed oven-curing condition on the AAFAS concrete specimens with various SS/SH ratios. In the delayed oven-curing conditions, the AAFAS concretes were waited in the ambient environment for 54 days and then the AAFAS concretes were put in an oven at 70°C for 48 hours (first 56 days for ambient curing condition and the last 2 days for oven-curing condition). The delayed oven-cured AAFAS concretes were tested only at the age of 56. days and three identical AAFAS concrete samples were used to calculate average CS values of the AAFAS concrete specimens at the age of 56.day.

3. Results and Discussions

3.1. *Ambient-cured Specimens*

Fig. 2 shows the CS development of the AAFAS concretes with various alkali activator ratios and 6M SH concentration in the ambient environment. The ambient-cured AAFAS concretes were tested at the ages of 7., 14., 28., and 56. days. As in the case of OPC concrete, the CS of the AAFAS concretes increased with time and the highest CS was attained on the AAFAS concretes at the age of 56. day.

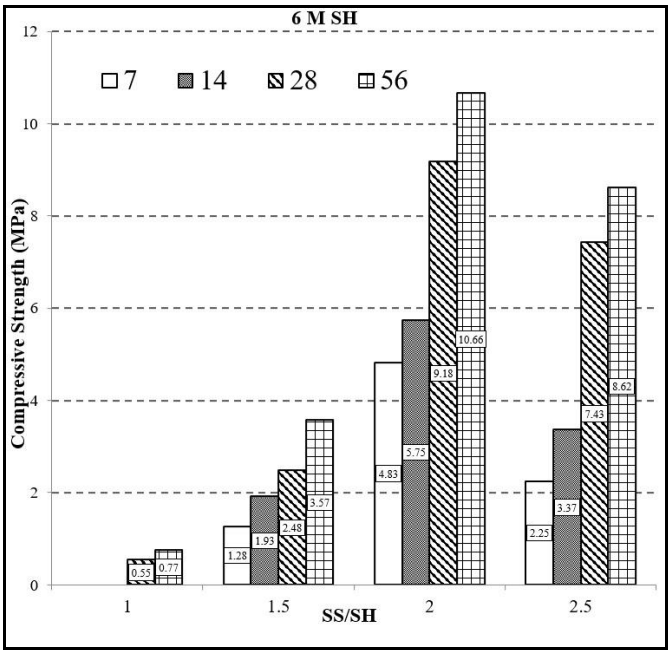

Fig. 2. Compressive strength development of the AAFAS specimens with various SS/SH ratios

The compressive strength (CS) test results indicated that the CS of the AAFAS concretes increased with an increasing alkali activator ratios up to the value of 2, and the CS of the AAFAS concretes started to be decreased after the further alkali activator ratio (2.5). The maximum and minimum CS were obtained in the AAFAS concretes with alkali activator ratios of 2 and 1, respectively. The CS could not be attained for the AAFAS concretes with an alkali activator ratio of 1. When the alkali activator ratio of the AAFAS specimens was 1.5, the average CS of the AAFAS concretes were 1.28 MPa, 1.93 MPa, 2.48 MPa, and 3.57 MPa at the ages of 7.day, 14.day, 28.day, and 56.day, respectively. For the AAFAS concretes with an alkali activator ratio of 2, the mean CS of the AAFAS specimens were found to be 4.83 MPa, 5.75 MPa, 9.18 MPa, and 10.66 MPa for 7.day, 14.day, 28.day,

and 56.day, respectively. For the AAFAS specimens with an alkali activator ratio of 2.5, the mean CS of the AAFAS specimens were obtained as 2.25 MPa, 3.37 MPa, 7.43 MPa, and 8.62 MPa at the ages of 7.day, 14.day, 28.day, and 56.day, respectively. The results indicated that ongoing geopolymerization reactions take place with time in the AAFAS concretes.

Table 3. Compressive strength changes of the AAFAS samples with respect to 56.day compressive strength (%)

Day	SS/SH ratios			
	1	1.5	2	2.5
7	-	36	45	26
14	-	54	54	39
28	71	69	86	86
56	100	100	100	100

Table 3 indicates the CS changes of the AAFAS concretes with respect to 56.day CS values. As stated earlier, there was no CS gain at 7.day and 14.day for the AAFAS concretes with an alkali activator ratio of 1. The CS development became 71% at 28.day with respect to 56.day CS for the AAFAS specimens with an alkali activator ratio of 1. For the AAFAS specimens with an alkali activator ratio of 1.5, the CS enhancements became 36%, 54%, and 69% at the ages of 7.day, 14.day, and 28.day, respectively. For the AAFAS concretes with an alkali activator ratio of 2, the CS enhancements at 7.day, 14.day, and 28.day were 45%, 54%, and 86%, respectively. For the AAFAS concretes with an alkali activator ratio of 2.5, the CS improvements were 26%, 39%, and 86% for 7.day, 14.day. and 28.day, respectively. The CS test results indicated that the lowest CS gain was observed on AAFAS concretes with an alkali activator ratio of 2.5 at the ages of 7.day (26%) and 14.day (39%), while the lowest CS gain at the age of 28.day was observed on the AAFAS concretes with an alkali activator ratio of 1.5 (69%). Meanwhile, the highest CS gain was observed on the AAFAS concretes with an alkali activator ratio of 2 at the ages of 7.day (45%), 14.day (54%) and 28.day (86%). For the AAFAS concretes with an alkali activator ratio of 2.5, approximately 60% CS enhancement was observed between 14.day and 28.day. For the AAFAS specimens with alkali activator ratios of 1 and 1.5, approximately 30% CS increase was observed after 28.day, while for the AAFAS specimens with alkali activator ratios of 2 and 2.5, the CS development became only 14% after 28.day.

3.2. *Delayed oven-cured Specimens*

Figure 3 shows the effect of the delayed oven-curing on the CS of the AAFAS concretes at 56.day. The delayed oven-cured AAFAS concretes indicated as 56-OC in Figure 3. Results indicated that at the end of the 56.day curing period, delayed oven-cured AAFAS concretes yielded higher CS values than the ambient-cured AAFAS concretes. The CS of the AAFAS concrete with alkali activator ratios of 1, 1.5, 2 and 2.5 were increased as 9%, 36%, 8%, and 33%, respectively due to the delayed oven-curing. Results indicated that the lowest CS enhancement was observed on the AAFAS specimens with an alkali activator ratio of 2, while the highest CS enhancement was noticed on the AAFAS concretes with an alkali activator ratio of 1.5. In addition, after the delayed oven-curing procedure, AAFAS concrete with an alkali activator ratio of 2 yielded similar CS values with the AAFAS concretes with an alkali activator ratio of 2.5.

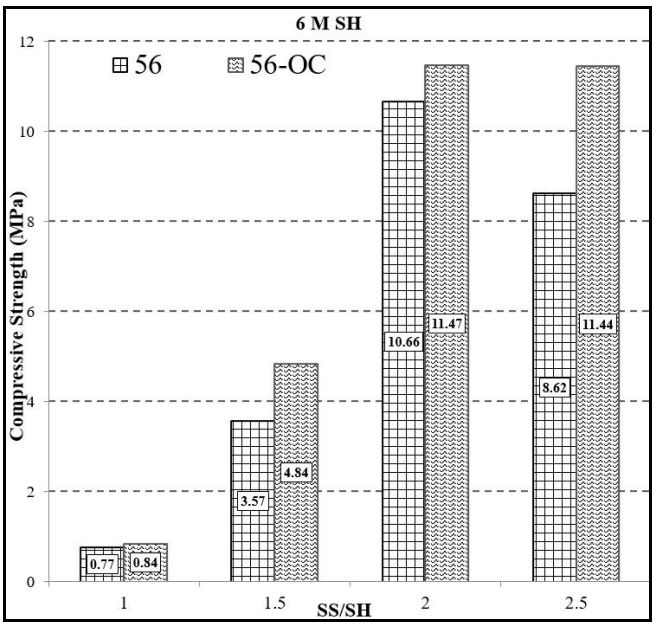

Fig. 3. Compressive strengths of the ambient cured and delayed oven-cured AAFAS specimens

4. Conclusions

In this study, the effect of various alkali activator ratios on the CS development of the AAFAS concretes was investigated using 6M SH concentration at the ages of 7.day, 14.day, 28.day, and 56.day. In addition, the effect of delayed oven-curing on the CS of the AAFAS concretes was also investigated and the results were summarized below;

- The results showed that the CS of the AAFAS concrete specimens increased with time similar to OPC concrete. The CS test results indicated that ongoing geopolymerization reactions take place in the AAFAS concretes up to the 56.day.

- The CS of the AAFAS samples with 6M SH concentrations enhanced with an increase in the alkali activator ratio up to the alkali activator ratio of 2, then the CS of the AAFAS samples were found to be decreased for the increased alkali activator ratio of 2.5.

- For the ambient-cured AAFAS concretes, the highest and the lowest CS were obtained in the AAFAS concrete specimens with alkali activator ratios of 2 and 1, respectively.

- The AAFAS concrete specimens with an alkali activator ratio of 1 showed very low CS (<1 MPa), which can be attributed to the low SH concentration in the used alkali activator.

- The ambient-cured CS test results of the AAFAS specimens also revealed that the lowest CS enhancement was obtained in the AAFAS specimens with an alkali activator ratio of 2.5 at the ages of both 7.day and 14.day, while the lowest CS improvement was observed in the AAFAS concretes with an alkali activator ratio of 1.5 at 28.day. In addition, the highest CS enhancement was reached in the AAFAS concretes with an alkali activator ratio of 2 for all the tested ages.

- The ambient-cured AAFAS specimens with alkali activator ratios of 1 and 1.5 showed approximately 30% CS increase between 28.day and 56.day, whereas for the AAFAS specimens with alkali activator ratios of 2 and 2.5, the CS enhancement became around 14% between 28.day and 56.day. Therefore, AAFAS concrete with a higher alkali activator ratio (≥2) should be utilized in the structural applications in ambient environments.

- The delayed oven-cured AAFAS specimens yielded higher CS values than the ambient-cured AAFAS specimens. The lowest CS enhancement was obtained in the AAFAS specimens with an alkali activator ratio of 2, while the highest CS improvement was achieved in the AAFAS specimens with an alkali activator ratio of 1.5 due to the delayed oven-curing at 56.day.

Acknowledgements

The author would like to express special thanks to Istanbul Gelisim University and Akcansa Company for material contributions. This study is a part of a term project of the Istanbul Gelisim University Civil Engineering students. Therefore, the author would like to express his gratitude to the students who in one way or another contributed to the realize the concrete production and the experiments of the study.

References

[1] S. A. Hasanein, H. M. Khate, S. A. A. El-Enein, and H. A. El-Sayed, “Resistance of alkali activated water-cooled slag geopolymer to sulphate attack”, Ceramics-Silikáty, vol. 55, no. 2, pp. 153–160, 2011.

[2] A. Niş, ‘‘Mineral katkılı betonların kimyasal durabilitesinin toplam bağlayıcı miktarı ve eşdeğer su/çimento parametreleriyle beraber incelenmesi’’, Balıkesir Üniversitesi Fen Bilimleri Enstitüsü Dergisi, vol. 21, no. 1, pp. 459-473, 2019.

[3] A. E. Kurtoglu, R. Alzeebaree, O. Aljumaili, A. Nis, M. E. Gulsan, G. Humur, and A. Cevik, ‘‘Mechanical and durability properties of fly ash and slag based geopolymer concrete’’, Advances in Concrete Construction, vol. 6, no. 4, pp. 345–362, 2018.

[4] A. Çevik, R. Alzeebaree, G. Humur, A. Niş, and M. E. Gülşan, ‘‘Effect of nano-silica on the chemical durability and mechanical performance of fly ash based geopolymer concrete’’, Ceramics International, vol. 44, no. 11, pp. 12253-12264, 2018.

[5] R. Alzeebaree, M.E Gulsan, A. Nis, A. Mohammedameen, and A. Cevik, ‘‘Performance of FRP confined and unconfined geopolymer concrete exposed to sulfate attacks’’, Steel and Composite Structures, vol. 29, no. 2, pp. 201-218, 2018.

[6] R. Alzeebaree, A. Çevik, B. Nematollahi, J. Sanjayan, A. Mohammedameen, and M.E. Gülşan, ‘‘Mechanical properties and durability of unconfined and confined geopolymer concrete with fiber reinforced polymers exposed to sulfuric acid’’, Construction and Building Materials, vol. 215, pp. 1015-1032, 2019.

[7] M. E. Gülşan, R. Alzeebaree, A. A. Rasheed, A. Niş, and A.E. Kurtoğlu, ‘‘Development of fly ash/slag based self-compacting geopolymer concrete using nano-silica and steel fiber’’, Construction and Building Materials, vol. 211, pp. 271-283, 2019.

[8] F. N. Okoye, S. Prakash, and N. B. Singh, ‘‘Durability of fly ash based geopolymer concrete in the presence of silica fume’’, Journal of Cleaner Production, vol. 149, pp. 1062-1067, 2017.

[9] J. Davidovits, Geopolymer Chemistry and Applications., 2nd Edn., Inst. Geopolymer, SaintQuentin, France, 2008.

[10] J. Davidovits, ‘‘Geopolymer cement to minimize carbon-dioxde greenhouse-warming’’, Ceram. Trans., vol. 37, pp. 165–182, 1993.

[11] S. Saha and C. Rajasekaran, ‘‘Enhancement of the properties of fly ash based geopolymer paste by incorporating ground granulated blast furnace slag’’, Construction and Building Materials, vol. 146, pp. 615-620, 2017.

[12] A. Fernández-Jiménez, J. G. Palomo, and F. Puertas, ‘‘Alkali-activated slag mortars: mechanical strength behaviour’’, Cement and Concrete Research, vol. 29, no. 8, pp. 1313-1321, 1999.

[13] K. Somna, C. Jaturapitakkul, P. Kajitvichyanukul, and P. Chindaprasirt, ‘‘NaOH-activated ground fly ash

geopolymer cured at ambient temperature'', Fuel, vol. 90, no. 6, pp. 2118-2124, 2011.

[14] T. Bakharev, ''Durability of geopolymer materials in sodium and magnesium sulfate solutions'', Cement and Concrete Research, vol. 35, no.6, 1233-1246, 2005.

[15] C. B. Cheah, M. H. Samsudin, M. Ramli, W.K. Part, and L.E. Tan, L. E. ''The use of high calcium wood ash in the preparation of Ground Granulated Blast Furnace Slag and Pulverized Fly Ash geopolymers: A complete microstructural and mechanical characterization'', Journal of Cleaner Production, vol. 156, pp. 114-123, 2017.

[16] N. K. Lee, J. G. Jang, and H.K. Lee, ''Shrinkage characteristics of alkali-activated fly ash/slag paste and mortar at early ages'', Cement and Concrete Composites, vol. 53, pp. 239-248, 2014.

[17] M. Hu, X. Zhu, and F. Long, ''Alkali-activated fly ash-based geopolymers with zeolite or bentonite as additives'', Cement and Concrete Composites, vol. 31, no. 10, pp. 762-768, 2009.

[18] G. Görhan, and G. Kürklü, ''The influence of the NaOH solution on the properties of the fly ash-based geopolymer mortar cured at different temperatures'', Composites part b: engineering, vol. 58, pp. 371-377, 2014.

[19] P. Duxson, , J. L. Provis, G. C. Lukey, S. W. Mallicoat, W. M. Kriven, and J. S. Van Deventer, ''Understanding the relationship between geopolymer composition, microstructure and mechanical properties'', Colloids and Surfaces A: Physicochemical and Engineering Aspects, vol. 269, no. 1-3, pp. 47-58, 2005.

[20] G.B. Singh, and K. V. Subramaniam, ''Evaluation of sodium content and sodium hydroxide molarity on compressive strength of alkali activated low-calcium fly ash'', Cement and Concrete Composites, vol. 81, pp. 122-132, 2017.

[21] M. Albitar, M. M. Ali, P. Visintin, and M. Drechsler, ''Durability evaluation of geopolymer and conventional concretes'', Construction and Building Materials, vol. 136, pp. 374-385, 2017.

[22] M. Soutsos, A. P. Boyle, R. Vinai, A. Hadjierakleous, and S. J. Barnett, ''Factors influencing the compressive strength of fly ash based geopolymers'', Construction and Building Materials, vol. 110, pp. 355-368, 2016.

Numerical Data Modelling and Classification in Marine Geology by the SPSS Statistics

Polina Lemenkova*‡

*College of Marine Geo-sciences, Ocean University of China, 238 Songling Rd., 266100, Qingdao, China

(pauline.lemenkova@gmail.com)

‡ Corresponding Author: Polina Lemenkova, 238 Songling Rd., 266100, Qingdao, China, Tel: +86-1768-554-1605, lemenkovapolina@stu.ouc.edu.cn or pauline.lemenkova@gmail.com

Received: 01.05.2019 Accepted:29.06.2019

Abstract- The paper focuses on the geostatistical analysis of the data set on the Philippine archipelago. The research question is understanding variability in several geospatial parameters (geology, geomorphology, tectonics and bathymetry) in different segments of the study area. The initial data set was generated in QGIS by digitizing 25 cross-sectioning profiles. The data set contained information on the geospatial parameters in the samples by profiles. Modelling and statistical analysis were performed in SPSS IBM Statistics software. The analysis of the topography shows strong variability of the elevations in the samples with the extreme depths in the central part of the study area (profile 13 with -9,400 m) and highest elevations in its south-western part (profile 17 with 1950 m). The analysis of the geological classes and lithology shows maximal samples of the basic volcanic rocks (40,40%) followed by mixed sedimentary consolidated rocks (31,90 %). Pairwise analysis of the sediment thickness and slope aspect demonstrates correlation between these two variables with the maximal sediment layer in the profiles 1-4 crossing the Philippines. The hierarchical dendrogram clustering of the bathymetry by three approaches shown maximal correlation of 5 clusters containing profile groups: 12-18 (centre), 22-25 (south-west), 1-2 (north), 7-8 (north-east), 19-21 (south-west). Other profiles show lesser similarities in the bathymetric patterns. The forecasting models were computed for the geospatial variables showing gradual increase in the gradient angles southwards and increased values for the sediment thickness in the north. Technically, the results proved effectiveness of the SPSS application of the geological data modelling.

Keywords Geological Modelling; SPSS Statistics; Data Analysis; Philippines; Marine Geology.

1. Introduction

Modelling geological data requires a multi-disciplinary approach to finding and analysing patterns in the categorical geospatial data. Understanding complex relationships between the variables constituting geospatial data set requires thorough analysis of the properties and features of the study area: geology, bathymetry, tectonics, geomorphology. A fusion of the different approaches and analytical methods and algorithms proposed by the existing statistical software and tools enables to solve such research problems and operate with the multi-source data.

Application of the data mining and machine learning algorithms for the geological domain is of particular interest nowadays, because the geospatial data are almost always include multidimensional data arrays collected through the geological expeditions as large data sets. Statistical analysis of the large data sets by various methods enables to perform precise and accurate data analysis, as well as perform predictive modelling, and visualize descriptive statistics on the raw data. Various approaches exist in data analysis and machine learning both covering general aspects of the data mining [1], [2], [3], [4], [5], as well as particular tasks of the geological modelling and data analysis in geosciences [6], [7], [8], [9], [10], [11].

The particular problem of the geoscience data modelling consists in traditional use of GIS and geoinformatics for the data analysis with significantly lesser usage of data analysis by the statistical algorithms and specific software (SPSS) or programming packages of R [12], [13], [14] or Python [15], [16], [17].

The data analysis in the geological marine mapping domains is traditionally based on the geoinformatics and embedded plugins of the GIS software [18], [19], [20]. Therefore, the statistical data analysis is often less

representative in the geosciences, comparing to the computer sciences, IT and finances. The statistical data analysis is widely used in other domain. These include, as mentioned before, such branches as economics, IT, finance and social studies where various algorithms and approaches are being developed, tested and improved. To fill in the gap between the geoscience and statistical data analysis, this research aims at the particular approach of the geodata modelling by means of the software SPSS IBM Statistics.

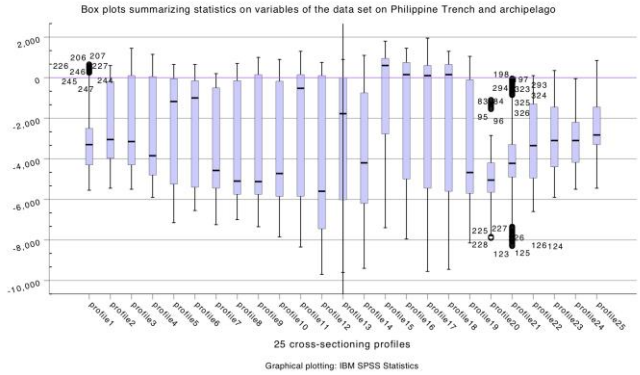

Fig. 1. Statistical box plots on the bathymetry: min-max values, 1st and 3rd quartiles, median.

The geological focus of the current research is analysis of the geological interrelationship between the variables (geomorphology, geology, tectonic plates, topography and bathymetry) of the study area: the Philippines islands and Philippine Trench located in the west Pacific Ocean, between the South China Sea and the Philippine Sea.

2. Methods

2.1. *Initializing GIS project and generating data set*

The first part of the research was performed in the Quantum GIS where the GIS project was initiated. The project contained vector thematic GIS layers with following

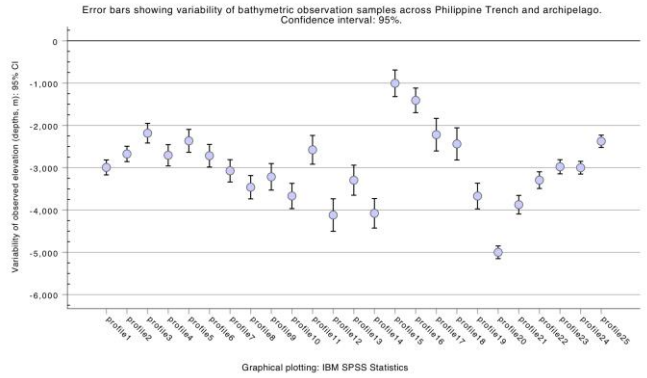

data: tectonics, geology, geomorphology, bathymetry.

Fig. 2. Error bar of variability (25 profiles) with a 5% confidence interval of the standard deviation.

The layers were processed, combined and re-projected in common coordinate system (UTM). Thereafter, the 25 cross-sectioning profiles were digitized across the Philippine archipelago and adjacent hadal trench crossing two tectonic plates: the Philippine Sea Plate and Sunda Plate. The information from all thematic layers where the digitized lines crossed the layers were recorded in the GIS attribute table which was then stored as a .csv table. At the next step, the table was imported int the IBM SPSS Statistics software as a working data set. All further research steps and graphical plotting were performed in the IBM SPSS Statistics.

2.2. *Analysis of the bathymetric ranges: variability of the samples by box plots and error bars*

Statistical analysis of the observations from the geospatial data set by visualizing box plots allows to distinguish concentration of the data showing the extreme values in the bathymetric and topographic elevations (Figure 1) across the Philippine Trench and archipelago. Plotted 25 box plots are constructed from five values each: minimum and maximum values, the first and third quartiles, and the median (Figure 1). The error bars for the bathymetric analysis were plotted using Graphs/Legacy Dialog menu from the SPSS. They show summaries for the separate

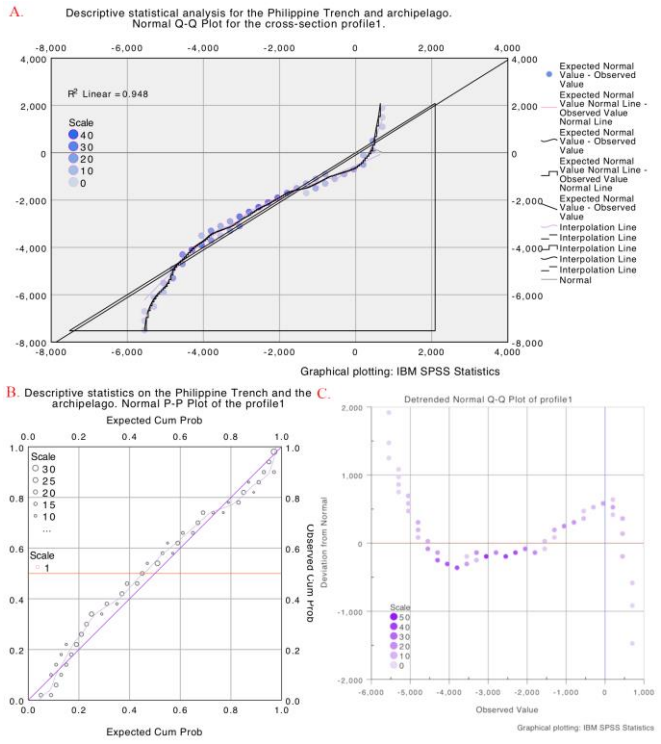

variables of 25 cross-sectioning profiles (Figure 2).

Fig. 3. Descriptive statistical analysis of the bathymetry by cross-sectioning profile 1. A) Normal QQ plot; B) Normal PP plot; C) Detrended normal QQ profile.

Each bar represents the confidence interval for the recorded means with excluded missing values showing the percentage value of 5% of the standard deviation. Descriptive statistical analysis on the bathymetry was performed by plotting the probability of the elevation data distribution by quantiles (QQ) and point-point (PP) plots. These methods show analysis of the normality of the

topographic data distribution. The PP plot shows a scatter diagram comparing two bathymetric samples of the same profile (Figure 3). The next step of the topographic analysis was performed by plotting statistical data description by the high-low charts for the analysis of the depths ranges showing summaries of the separate variables by the 25 profiles (Figure 4).

2.3. *Multi-variance analysis of the geospatial variables: geology, tectonics and geomorphology*

The analysis of the geological classes and lithology of the study area was performed by two approaches. First, qualitative analysis of the geological classes by the multi-plot visualization for comparative analysis (Figure 5). The chart shows mean values of the observation samples by separate variables (cross-sectioning profiles, 1:25 crossing the Philippine archipelago and trench. Second, the quantitative analysis of the geologic data (Figure 6) was performed using pie charts showing visual data distribution

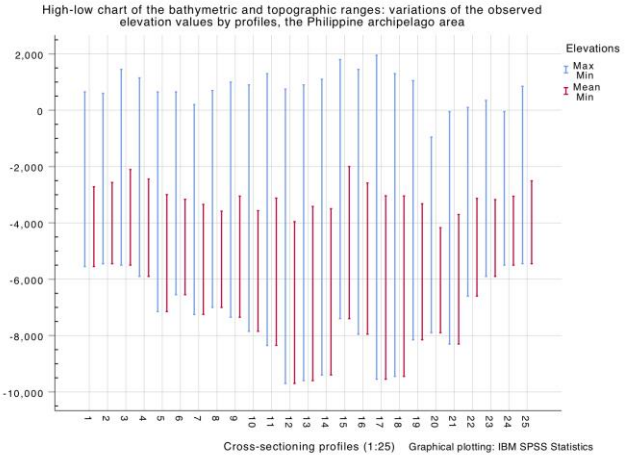

across the Philippines.

Fig. 4. Statistical analysis by high-low charts for bathymetry and topography, the Philippines

Quantitative analysis of the tectonic values by the cross-sectioning profiles was performed by means of the drop line chart plotting aimed at the pairwise comparative analysis of the two tectonics plate: Sunda Plate and the Philippine Sea Plate (Figure 7).

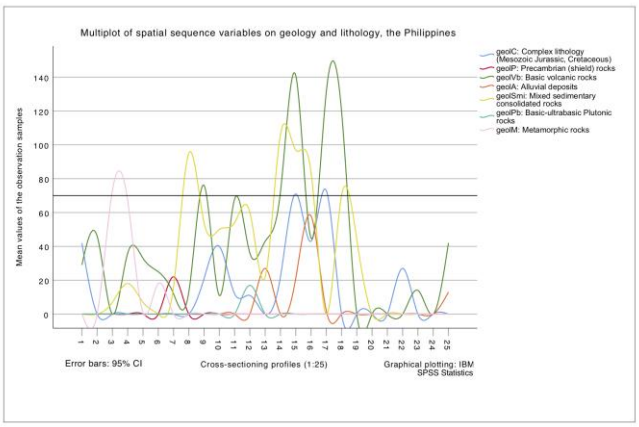

Fig. 5. Variation of the data distribution for the geologic classes across the 25 profiles

Pairwise correlation of the geology (sedimentation thickness layer) and geomorphology was done using method of the stacked area charts where two variables were visualized in a combined plot using relative y-scale factor (Figure 8).

2.4. *Hierarchical cluster analysis and modelling*

Visualizing data by the hierarchical cluster analysis and plotting dendrograms (tree diagrams) is an effective method reviewed and discussed in various existing research works [21], [22], [23]. Hierarchical clustering aims at grouping data by the attribute similarities (Figure 8 and Figure 9). The hierarchical cluster analysis was performed using 'Analyse / Classify / Hierarchical Cluster' module by the SPSS Statistics. The statistical methods included agglomeration schedule of the variables and computing proximity matrix

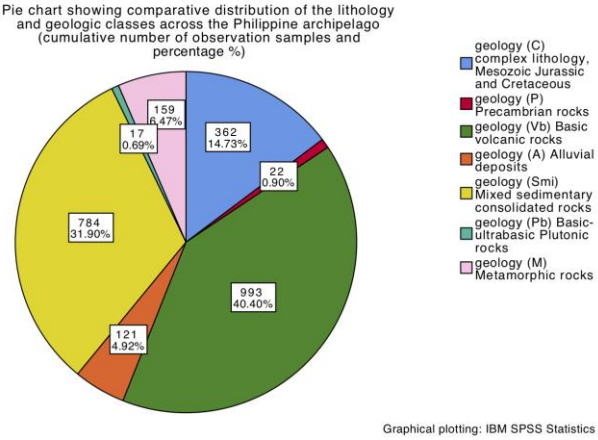

(Table 2).

Fig. 6. Quantitative data distribution on lithology and geology across the Philippine Islands

Table 1. Descriptive Statistics for the recorded geological classes across 25 profiles, Philippines

Class name	Maximum	Mean	Std. Deviation
geolC	73	14.48	22.602
geolP	22	.88	4.400
geolVb	141	39.72	41.390
geolA	58	4.84	13.104
geolSmi	106	31.36	36.555
geolPb	17	.68	3.400
geolM	73	6.36	19.506

Three methods of the data grouping were tested to achieve optimal results: Ward's method, Centroid clustering and Average linkage between groups. The best solution was proposed by the Ward's criterion method, a general agglomerative hierarchical clustering procedure, initially suggested by J. H. Ward [24] and developed in further studies [25], [26].

The particularity of this method consists in its approach towards data grouping: the criterion for choosing pair of clusters to merge at each step is based on the optimal value of an objective function. Modelling forecasts for the geological and geomorphic variables enables to asses the possible variations of the data using existing condition by given condition (Figure 11).

Table 2. Proximity Dissimilarity Matrix by Euclidean Distance. Geological variables: C, P, Vb, A, Smi, Pb, M

Geol.	geolC	geolP	geolVb	geolA	geolSmi	geolPb	geol M
C	.000	134.112	207.222	118.097	199.028	131.973	166.268
P	134.112	.000	283.748	72.049	237.563	27.803	103.087
Vb	207.222	283.748	.000	264.923	206.782	282.174	291.393
A	118.097	72.049	264.923	.000	215.307	70.682	121.861
Smi	199.028	237.563	206.782	215.307	.000	234.318	251.696
Pb	131.973	27.803	282.174	70.682	234.318	.000	102.137
M	166.268	103.087	291.393	121.861	251.696	102.137	.000

3. Results

The first part of the research (Figures 1-4) aims at the analysis of the bathymetry and topography. In this part the elevations across the study area were tested by various statistical approaches.

The results on the bathymetric analysis show following findings. As can be seen from the Figure 1, the greatest depths in bathymetry of the Philippine archipelago from the whole data set is noted by the profiles 12 and 13 where the values are reaching -9,150 and -9,400 meters, respectively. On the contrary, the highest elevation values are detected by the profiles Nr. 17 (1950 meters).

Error bars (Figure 2) demonstrate variability of the data (cross-sectioning 25 bathymetric profiles) with a 5% confidence interval of the standard deviation. As can be concluded by the Figure 2, the minimal error bars are recorded by the profile 20 with depth of -5,000m followed by the profile 24 and 25 with depths ranges of -3,000 and -2,400 meters, respectively. The PP plot (Figure 3) shows a scatter diagram comparing two bathymetric samples of the same profile. As can be seen from the Figure 3 B (lower left), the profiles Nr. 1 shows similar underlying distributions by the points with the line representing real data almost approaching modelled one, as shown by X axe (expected cumulative probability).

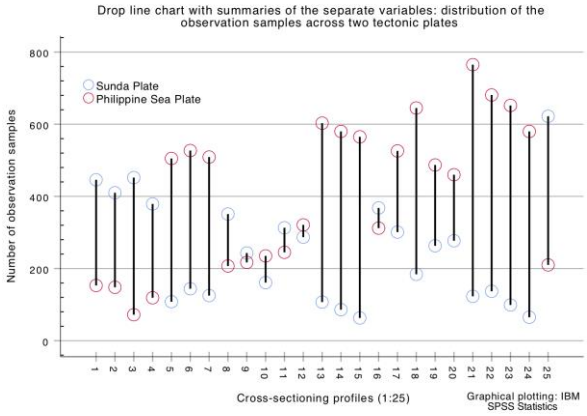

Fig. 7. Pairwise comparative analysis of the samples distribution across two tectonic plates

The probability of the sample points is visually expressed by the point size (Figure 3 B). Figure 3A shows example of the normal quantile-quantile (QQ) plot for the case of profile 1.

Table 3. ANOVA One-Way computing results for the geological variables

Geological variables		Sum of Squares	df	Mean Square
geolC	Between Groups, Total	12260.240	24	510.843
geolP	Between Groups, Tot.	464.640	24	19.360
geolVb	Between Groups, Tot.	41115.040	24	1713.127
geolA	Between Groups, Tot.	4121.360	24	171.723
geolSmi	Between Groups, Tot.	32069.760	24	1336.240
geolPb	Between Groups, Tot	277.440	24	11.560
geolM	Between Groups, Tot.	9131.760	24	380.490

The same data modelling was modelled for the 25 profiles of the data set. The data demonstrated normal

distribution. Figure 3C (lower right) shows a scatter diagram comparing a distribution of samples of the profile 1 by detrended normal QQ plot for this profile. Central part of the Philippine Trench (profiles Nr. 12-14) and south-eastern segment (profiles Nr. 17-19) are notable for the increased depth ranges, as can be seen from the Figure 4.

Table 4. Statistics on the frequencies in data records: sediment thickness and slope aspect (a). Calculated from grouped data. b). Multiple modes exist. The smallest value is shown. c). Percentiles are calculated from the grouped data.

Statistical values	Sediment thickness	Slope aspect
Mean	824.20	133.36
Std. Error of Mean	127.171	16.988
Median	629.00[a]	114.00[a]
Mode	402[b]	229
Std. Deviation	635.856	84.940
Variance	404312.250	7214.823
Skewness	2.946	.222
Std. Error Skewness	.464	.464
Kurtosis	8.088	-1.252
Std. Error of Kurtosis	.902	.902
Range	2504	277
Minimum	402	14
Maximum	2906	291
Sum	20605	3334

The depth variations in the bathymetric patterns are caused by the specific geomorphic conditions of the Philippine archipelago that crosses two tectonic plates and submarine volcanic areas.

Table 5. Model Statistics

Model	Model Fit statistics	Ljung-Box Q(18)		
	Stationary R-squared	Statistics	DF	Sig.
sedim_thickness-Model_1	.390	3.650	17	1.000
slope_aspect-Model_2	.251	12.269	17	.784
tan_angle-Model_3	.808	11.868	16	.753

The collision of the tectonic slabs directly affects the topography. Other factors include submarine erosions and geology (sedimentation and physical properties of rocks). On the contrary, the elevations are notable (Figure 4) for the profiles 15, 17 and 3 where the profiles cross the selected small islands from the Philippine archipelago.

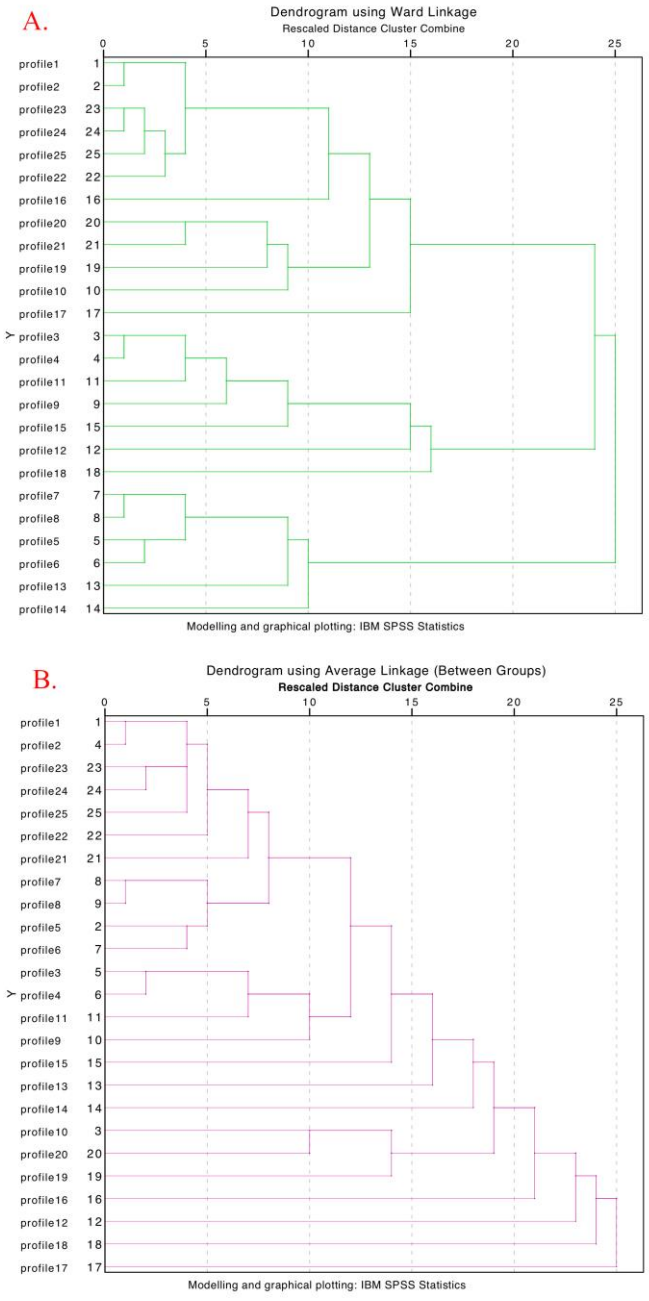

Fig. 8. Hierarchical cluster analysis with dendrogram visualization by two approaches: Ward Linkage and Average Linkage, for the set of cross-section profiles 1:25.

Analysis of the distribution of the lithologic classes by samples shows (Figure 5) the significant predominance of the 'Basic volcanic rocks' followed by the 'Mixed sedimentary consolidated rocks' formed by accumulating of the sediment particles, as the most representative of two classes recorded across the Philippine archipelago by cross-sectioning profiles.

The mixed sedimentary consolidated rocks were formed by the submarine erosion from the abyssal plain area located near the Philippine Trench and transported to the trench, as well as submarine canyons followed by the water currents. Metamorphic rocks formed as a result of the transformation of various types of the existing rocks created third large group of the lithological rock types on the Philippine archipelago.

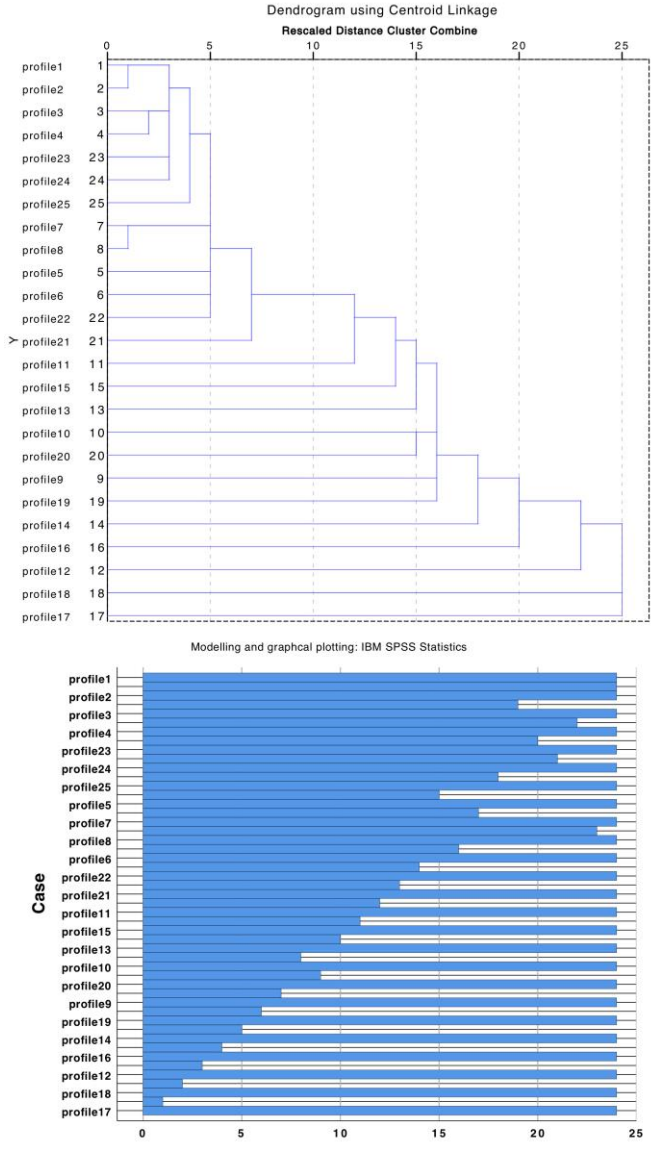

Fig. 9. Hierarchical cluster analysis with dendrogram visualization by Centroid Linkage approach and cases.

The analysis of the geological classes and lithology show maximal samples of the Basic volcanic rocks, Vb (40,40%) followed by Mixed sedimentary consolidated rocks, Smi (31,90 %) across the study area (Figure 6). On the contrary, Basic-ultrabasic plutonic rocks (Pb) are the least represented rock types among other lithological groups with the least samples recorded (0.69%).

This type of the rocks is presented by the igneous and meta-igneous rocks with a very low silica content, which constitute the lowerst part of oceanic crust of the Philippine Trench, generated at the mid-ocean or back-arc ridges in the area nearby. Precambrian rocks (P) are the second underrepresented rock type across the Philippines, as can be noticed on the Figure 6 (0.90%).

The Precambrian rocks are exceptionally rare since they are formed during the earliest geologic period of the Earth formation, and in most cases they are formed further to the metamorphic rocks. With 4,92 % and 6,47 % of the detected data samples, the Alluvial deposits (A) of the coastal area of the Philippines and the Metamorphic rocks (M) show the moderate part in the patters of the data distribution, respectively.

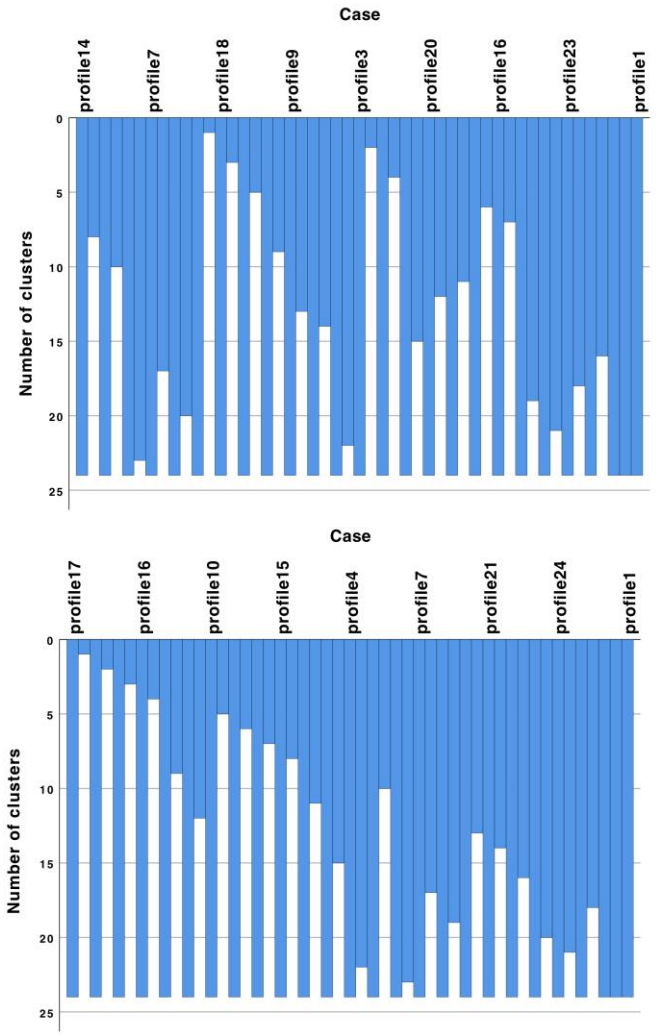

Fig. 10. Hierarchical cluster analysis: cluster cases.

Complex lithology of the Mesozoic, Jurassic and Cretaceous rocks is covered by the 14,73% of the total records in the observation samples.

The variations in the lithological patters of the Philippines may reflect the restricted geological and oceanographic conditions of the rocks formation, as well as the specific stratigraphy and sedimentary ocean environment of the Jurassic, Mesozoic and Cretaceous strata around the Philippines.

4. Results

The computation of the descriptive statistical parameters (standard deviation, maximal and mean values) is shown on the Table 1. The computation of the proximity dissimilarity matrix by Euclidean distance method is presented on the Table 2. It shows the two-dimensional square array containing the distances between the geological values across the seven recorded groups taken pairwise, between the

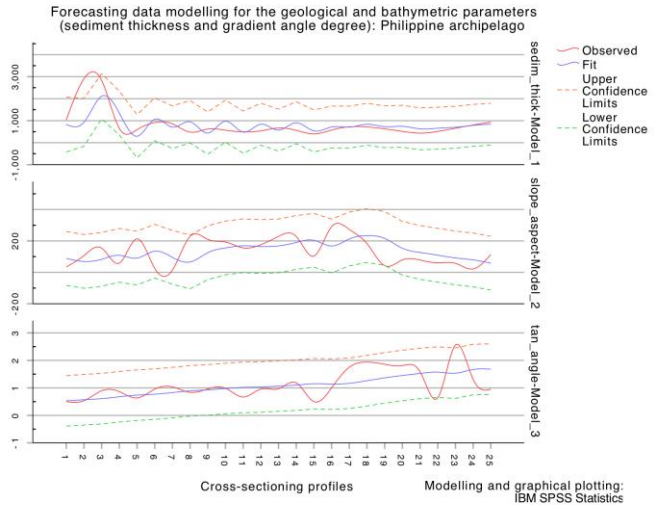

elements of the each set of the geological classes.

Fig. 11. Forecasting data modelling for the geospatial parameters: A) sediment thickness, slope aspect and gradient angles

The computations of the One-Way ANOVA for the geological modelling are shown on the Table 3 to performed to compare means of the seven geological samples. The graphical results of the drop line chart visualization, one of the experimental statistical methods, can be used to determine pairs of the factors that should be analysed comparatively. Two tectonic plates that cross the study area, Philippine Sea Plate and Sunda Plate, influence the geomorphology of the Philippines by the slab collision. The characteristics of the data distribution by two plates, respectively, can be used for the analysis of the spread of the tectonic plates in the study area. Thus, Figure 7 illustrates the maximal samples located on the Philippine Sea plate for the profiles 21, 22 and 23 (765, 681 and 652 samples, respectively), that is south-west location of the Philippines. Sunda Plate, a minor tectonic plate located mostly in the South-China Sea, has significantly lesser influence on the Philippine Trench bathymetry comparing to the Philippine Sea Plate. Thus, it shows much lesser observation samples with the maximal records for the profile 25 (622 samples).

The hierarchical dendrogram clustering of the bathymetry by three approaches shown maximal correlation of 5 clusters containing profile groups across the Philippines: 12-18 (centre), 22-25 (south-west), 1-2 (north), 7-8 (north-east), 19-21 (south-west). Other profiles show lesser similarities in the bathymetric patterns. Grouping bathymetric data by classes using hierarchical clustering (Figure 8) aimed at building agglomerative hierarchy of the bathymetric ranges divided by clusters according to the similarities in depths or topographic elevations for the segments located on the land areas (Philippine islands).

By comparing three types of the clustering, Ward, Average Linkage (Figure 8) and Centroid Linkage (Figure 9) for several cluster cases of the 25 profiles (Figure 10), the Ward approach demonstrates the most effective results of clustering approach dividing the data set into distinct three groups that are in turn subdivided into small groups of the profiles. The first class comprises profiles 1-2, 10, 16-17, 19-25 with similarities in the elevation ranges. The majority of the profiles of this class are located in the southern part of the tench (starting from 16th to 25th), and two profiles belongs to the northern part of the trench. The second class includes profiles 3-4, 9, 11-12, 15 and 18, mostly located in the central part of the crossing Philippine Trench. Finally, the third class includes the group of profiles 5-8 (north-eastern part of the area) and profiles 13-14 located in the central part of the trench. The division of the profiles is performed by the topographic similarity of the depth values, both in the absolute values and in their repeatability showing character

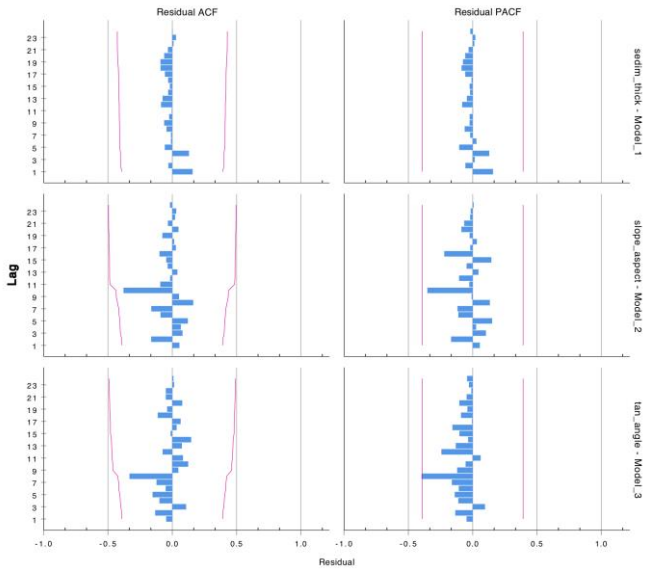

of the geomorphic patterns.

Fig. 12. Forecasting data modelling for the geospatial parameters: B) Residuals for the autocorrelation (ACF) and partial autocorrelation (PACF)

Final part of the research included forecasting models computed for the geospatial variables showing gradual increase in the gradient angles (in tangent) by 25 profiles in the southward direction and increased values for the sediment thickness for the profiles 1-4 (north). The computational part of this methodology is shown on the Table 5 (Statistical computations), Table 6 (Model fit) and Table 7 (Model fit: Percentile), respectively.

The forecasting data modelling shows following geospatial parameters: sediment thickness, slope aspect and gradient angles (Figure 11), residuals for the autocorrelation (ACF) and partial autocorrelation (PACF) (Figure 12). The autocorrelation of a geological parameters as a function of delay in the observation samples across the data samples (profiles 1:25). It shows similarity between the geologic observations as a function of the spatial lag between the samples in a range from 1 to 25 (Figure 12).

Table 6. Model fit

Fit Statistics	Mean	SE	Min	Max
Stationary R-squared	.483	.290	.251	.808
R-squared	.249	.179	.048	.390
RMSE	196.836	271.913	.444	507.186
MAPE	58.569	45.000	30.448	110.470
MaxAPE	278.281	264.341	106.147	582.646
MAE	120.275	151.231	.309	290.153
MaxAE	717.296	1095.299	1.021	1978.148
Normalized BIC	6.771	7.292	-1.365	12.715

In this way it is aimed to show repeating patterns and frequency in the geospatial observations of three types: sediment thickness layer, slope aspect, gradient angle degree.

Table 7. Model fit: Percentile

5	10	25	50	75	90	95
.251	.251	.251	.390	.808	.808	.808
.048	.048	.048	.307	.390	.390	.390
.444	.444	.444	82.878	507.186	507.186	507.186
30.448	30.448	30.448	34.790	110.470	110.470	110.470
106.147	106.147	106.147	146.050	582.646	582.646	582.646
.309	.309	.309	70.363	290.153	290.153	290.153
1.021	1.021	1.021	172.720	1978.148	1978.148	1978.148

General correlation between the sediment thickness and the slope gradient can be explained by the geomorphic properties of the hadal trench affecting the patterns of the sediment accumulation. Instability can be noticed by the profiles 1-4 where the correlation is not direct due to the geospatial location (crossing Philippine archipelago), followed by the stable pattern for the rest of the profiles. The increase in the sediment noticed for the profiles 1-4 shows the Philippine archipelago. The computations are presented on the Table 4.

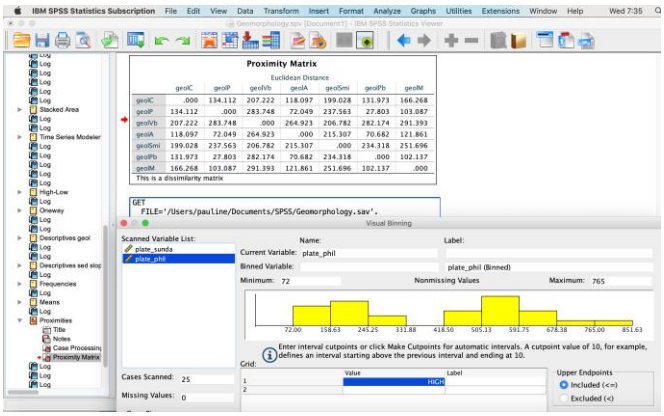

Fig. 13. Graphical User Interface of the project in IBM SPSS Statistics

5. Conclusion

The presented results show variations in the geomorphic, bathymetric and geological settings of the Philippine archipelago. The computations, modelling and visualization of the data was performed by the SPSS IBM Statistics software. Methodologically, the research demonstrated high effectiveness of the SPSS application towards the geological data modelling. Demonstrated multi-functional approach for the data processing is one of the defining tools in the geological data assessment. Compared to other tools, programs and methods, e.g. statistical libraries of R or Python programming languages, the SPSS IBM Statistics demonstrated more straightforwardness due to the GUI (graphical user interface), Figure 13. However, compared to the popular and widely used MS Excel, the SPSS IBM Statistics proposes much more functionalities for the advanced statistical modelling.

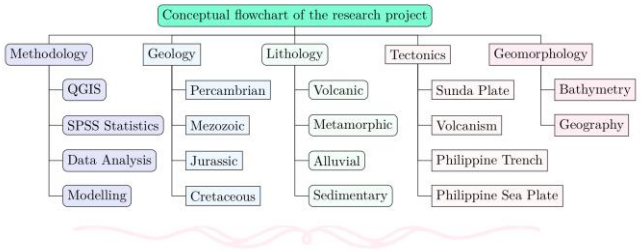

Fig. 14. Schematic methodological flowchart of the current research

Various statistical approaches have been tested to quantify the geological differences of the Philippine archipelago, as well as trends and variability in its bathymetric patterns and correlation between the geomorphic landforms and geological features (layers of slope aspect and sediment thickness). The use of different modelling algorithms, as well as the choice of the variables within the dataset to be modelled and used for numerical simulations can are important in the geological investigations [27], [28], [29]. Therefore, selecting statistical algorithms for the data processing is of high importance. The schematic research flowchart used in this research includes thematic clusters, such as geology, tectonics, geomorphology of the study area, as well as methodological approaches (GIS and statistical analysis), Figure 14.

This research is focused on the application of the existing tools, approaches and statistical modelling algorithms provided by IBM SPSS Statistics software towards geological modelling. Finding revealed how well tested variables (geomorphology, lithology, bathymetry) agree upon the geomorphic variations within the selected study area of the Philippines. The study furthermore demonstrated spatial variability of the geomorphology of the Philippine trench and adjusting archipelago. The consistent combination in various statistical metrics of the SPSS IBM Statistics shown a multi-factor analysis of the study area from different approaches (Figure 14): 1) bathymetry (assessment of variations in depth and elevations); 2) geology (assessment of various geologic classes of the Philippine islands); 3) geomorphology (assessment of the slope degree); 4) sedimentation (assessment of the variation in sediment thickness layer); 4) geometric variations of the hadal trench (assessment of the slope degree and aspect); 5) lithology (assessment of the properties and origin of the rocks); 6) tectonics (assessment of the distribution of the observation samples across two tectonic plates: Sunda Plate and the Philippine Sea Plate). All tested modelling and classification approaches performed by the SPSS on the data set and observation samples proved spatial variability in the geologic and geomorphic structure of the Philippine archipelago and hadal trench.

Acknowledgements

This research was funded by the China Scholarship Council (CSC), State Oceanic Administration (SOA), Marine Scholarship of China, Grant Nr. 2016SOA002, Beijing, People's Republic of China.

References

[1] A. S. Sidhu, C.Y. Cho, J.A. Leong, R.K.J. Tan, "Large Scale Data Analytics". Studies in Computational Intelligence Data, Semantics and Cloud Computing, vol. 806, pp. 89. Springer, Australia. doi: 10.1007/978-3-030-03892-2

[2] H. Cuesta, and S. Kumar. 2016. Practical Data Analysis, 2nd Edition. A practical guide to obtaining, transforming, exploring, and analyzing data using Python, MongoDB, and Apache Spark. pp. 360. ISBN-10: 1785289713. Packt Publishing Ltd. Livery Place, Birmingham, UK.

[3] P. Lemenkova. "R scripting libraries for comparative analysis of the correlation methods to identify factors affecting Mariana Trench formation". Journal of Marine Technolology and Environment, vol. 2, pp. 35-42, 2018. arXiv: 1812.01099, doi: 10.6084/m9.figshare.7434167

[4] C.D. Manning, P. Raghavan, and H. Schuetze, An introduction to information retrieval. Cambridge: Cambridge University Press, 2009.

[5] Y. Demchenko, P. Grosso, C. de Laat, P. Membrey, "Addressing big data issues in scientific data infrastructure," 2013 International Conference on Collaboration Technologies and Systems (CTS), San Diego, CA, 2013, pp. 48–55.

[6] J. Davis, Statistics and Data Analysis in Geology. Kansas Geological Survey John Wiley and Sons, 1990.

[7] F. Politz, B. Kazimi, and M. Sester, "Classification of Laser Scanning Data Using Deep Learning", vol. 38. Wissenschaftlich-Technische Jahrestagung der DGPF und PFGK18 Tagung in München – Publikationen der DGPF, Band 27, 2018.

[8] C. S. Campbell, P. W. Cleary, and M. Hopkins, "Large-scale landslide simulations: Global deformation, velocities and basal friction", Journal of Geophysical Research: Solid Earth, vol. 100(B5): pp. 8267–8283.

[9] P. Lemenkova, "Processing Oceanographic Data by Python Libraries Numpy, SciPy And Pandas", Aquatic Research, vol. 2(2), pp. 73-91, 2019, doi: 10.3153/AR19009

[10] S. H., Cannon, and W. Z. Savage, "A mass-change model for the estimation of debris-flow runout". The Journal of Geology, vol. 96(2), pp. 221–227, 1988.

[11] P. Lemenkova, 2018. "Factor Analysis by R Programming to Assess Variability Among Environmental Determinants of the Mariana Trench". Turkish Journal of Maritime and Marine Sciences, 4(2), pp. 146-155, doi: 10.6084/m9.figshare.7358207, 2018.

[12] R Development Core Team (2012). R: A Language and Environment for Statistical Computing. R Foundation for Statistical Computing, Vienna, Austria. ISBN 3-900051-07-0, [Online] url: http://www.R-project.org/

[13] D. Sarkar, Lattice: Multivariate data visualization with R. pp.25, New York: Springer, 2008.

[14] P. Lemenkova, 2019. "An empirical study of R applications for data analysis in marine geology". Marine Science and Technology Bulletin, vol. 8(1): pp. 1–9, 2019. doi: 10.33714/masteb.486678

[15] G. van Rossum. Python Programming Language. 2011. [Online] url: https://www.python.org/

[16] I. Idris Python Data Analysis Learn how to apply powerful data analysis techniques with popular open source Python modules. 348 pp. Packt Publishing. Birmingham, UK, 2014. ISBN 978-1-78355-335-8.

[17] R. Johansson, Numerical Python. A Practical Techniques Approach for Industry. Urayasu, Chiba, Japan, 2015. doi: 10.1007/978-1-4842-0553-2

[18] L. Ferranti, S. Passaro, and G. de Alteriis. "Morphotectonics of the Gorringe Bank summit, eastern Atlantic Ocean, based on high-resolution multibeam bathymetry". Quaternary International, 332, 99-114, 2014. doi: 10.1016/j.quaint.2013.11.011

[19] J.T. Vázquez, B. Alonso, M.C. Fernández-Puga, M. Gómez-Ballesteros, J. Iglesias, D. Palomino, C. Roque, G. Ercilla, and V. Díaz-del-Río. "Seamounts along the Iberian Continental Margins". Boletín Geológico y Minero, vol. 126 (2-3), pp. 483-514, 2015.

[20] C. Yesson, R. C. Malcolm, M. L. Taylor, A. D. Rogers. 2011. "The global distribution of seamounts based on 30 arc seconds bathymetry data". Deep-Sea Research Part I: Oceanographic Research Papers, vol. 58, pp. 442-453. doi: 10.1016/j.dsr.2011.02.004

[21] Jain, A.K., and Dubes, R.C., Algorithms for Clustering Data, Englewood Cliffs NJ: Prentice-Hall, 1988.

[22] Meila, M., "Comparing clusterings – An information based distance". Journal of Multivariate Analysis, vol. 98(5), pp. 873–895, 2007.

[23] Kumaran, G., Allan, J., and McCallum, "A. Classification models for new event detection", International conference on information and knowledge management (CIKM2004). ACM, 2004.

[24] J.H. Ward, "Hierarchical Grouping to Optimize an Objective Function", Journal of the American Statistical Association, vol. 58, pp. 236–244, 1963.

[25] P. Lemenkova. "Hierarchical Cluster Analysis by R language for Pattern Recognition in the Bathymetric Data Frame: a Case Study of the Mariana Trench, Pacific Ocean", 5th International Conference Virtual Simulation, Prototyping and Industrial Design. Proceedings, Ed. M. N. Krasnyansky. Tambov, vol. 2 (5), pp. 147–152, Nov. 14–16, 2018., doi: 10.6084/m9.figshare.7531550

[26] Murtagh, F. "Ward's Hierarchical Agglomerative Clustering Method: Which Algorithms Implement Ward's Criterion?" Journal of Classification, vol. 31, pp. 274-295, 2014. doi: 10.1007/s00357-014-9161-z

[27] Gauer, P., A. Elverhoi, D. Issler, and F. V. De Blasio. 2006. On numerical simulations of subaqueous slides: back-calculations of laboratory experiments of clay-rich slides. Norsk Geologisk Tidsskrift, vol. 86(3), pp. 295.

[28] A. Cerioli, F. Torti, M. Riani. 2013. Algorithms from and for Nature and Life. Studies in Classification, Data Analysis, and Knowledge Organization. Eds: B. Lausen, D. V. d Poel, A. Ultsch. 547 pp. ISBN-10: 978-3-319-00034-3. Springer, doi: 10.1007/978-3-319-00035-0

[29] N. Boylan, C. Gaudin, D.J. White, and M.F. Randolph. "Modelling of submarine slides in the geotechnical centrifuge", 7th International Conference on Physical Modelling in Geotechnics (ICPMG), pp. 1095–1100. Zurich, Switzerland: ICPMG, 2010.

[30] J.M. Chambers. Software for Data Analysis Programming with R. Springer, pp. 237-288, 2008. doi: 10.1007/978-0-387-75936-4

INTERNATIONAL JOURNAL OF ENGINEERING TECHNOLOGIES-IJET

Guide for Authors

The **International Journal of Engineering Technologies (IJET)** seeks to promote and disseminate knowledge of the various topics of engineering technologies. The journal aims to present to the international community important results of work in the fields of engineering such as imagining, researching, planning, creating, testing, improving, implementing, using and asking. The journal also aims to help researchers, scientists, manufacturers, institutions, world agencies, societies, etc. to keep up with new developments in theory and applications and to provide alternative engineering solutions to current.

The *International Journal of Engineering Technologies* is a quarterly published journal and operates an online submission and peer review system allowing authors to submit articles online and track their progress via its web interface. The journal aims for a publication speed of **60 days** from submission until final publication.

The coverage of IJET includes the following engineering areas, but not limited to:

All filed of engineering such as;

Chemical engineering

- Biomolecular engineering
- Materials engineering
- Molecular engineering
- Process engineering

Civil engineering

- Environmental engineering
- Geotechnical engineering
- Structural engineering
- Transport engineering
- Water resources engineering

Electrical engineering

- Computer engineering
- Electronic engineering
- Optical engineering
- Power engineering

Mechanical engineering

- Acoustical engineering
- Manufacturing engineering
- Thermal engineering
- Vehicle engineering

Systems (interdisciplinary) engineering

- Aerospace engineering
- Agricultural engineering
- Applied engineering
- Biological engineering
- Building services engineering
- Energy engineering
- Railway engineering
- Industrial engineering
- Mechatronics
- Military engineering
- Nano engineering
- Nuclear engineering
- Petroleum engineering

Types of Articles submitted should be original research papers, not previously published, in one of the following categories,

- Applicational and design studies.
- Technology development,

– Comparative case studies.

– Reviews of special topics.

– Reviews of work in progress and facilities development.

– Survey articles.

– Guest editorials for special issues.

Ethic Responsibilities

The publication of an article in peer-reviewed *"International Journal of Engineering Technologies"* is an essential building block in the development of a coherent and respected network of knowledge. It is a direct reflection of the quality of the work. Peer-reviewed articles support and embody the scientific method. It is therefore important to agree upon standards of expected ethical behavior for all parties involved in the act of publishing: the author, the journal editor, the peer reviewer, the publisher and the society of society-owned or sponsored journals.

All authors are requested to disclose any actual or potential conflict of interest including any financial, personal or other relationships with other people or organizations within three years of beginning the submitted work that could inappropriately influence, or be perceived to influence, their work.

Submission of an article implies that the work described has not been published previously that it is not under consideration for publication elsewhere. The submission should be approved by all authors and tacitly or explicitly by the responsible authorities where the work was carried out, and that, if accepted, it will not be published elsewhere in the same form, in English or in any other language, including electronically without the written consent of the copyright-holder.

Upon acceptance of an article, authors will be asked to complete a "Copyright Form". Acceptance of the agreement will ensure the widest possible dissemination of information. An e-mail will be sent to the corresponding author confirming receipt of the manuscript together with a "Copyright Form" form or a link to the online version of this agreement.

Author Rights

As a journal author, you retain rights for a large number of author uses, including use by your employing institute or company. These rights are retained and permitted without the need to obtain specific permission from *IJET.* These include:

- The right to make copies (print or electronic) of the journal article for your own personal use, including for your own classroom teaching use;
- The right to make copies and distribute copies (including via e-mail) of the journal article to research colleagues, for personal use by such colleagues for scholarly purposes;
- The right to post a pre-print version of the journal article on internet web sites including electronic pre-print servers, and to retain indefinitely such version on such servers or sites for scholarly purposes
- the right to post a revised personal version of the text of the final journal article on your personal or institutional web site or server for scholarly purposes
- The right to use the journal article or any part thereof in a printed compilation of your works, such as collected writings or lecture notes.

Article Style

Authors must strictly follow the guide for authors, or their articles may be rejected without review. Editors reserve the right to adjust the style to certain standards of uniformity. Follow Title, Authors, Affiliations, Abstract, Keywords, Introduction, Materials and Methods, Theory/Calculation, Conclusions, Acknowledgements, References order when typing articles. The corresponding author should be identified with an asterisk and footnote. Collate

acknowledgements in a separate section at the end of the article and do not include them on the title page, as a footnote to the title or otherwise.

Abstract and Keywords:

Enter an abstract of up to 250 words for all articles. This is a concise summary of the whole paper, not just the conclusions, and is understandable without reference to the rest of the paper. It should contain no citation to other published work. Include up to six keywords that describe your paper for indexing purposes.

Abbreviations and Acronyms:

Define abbreviations and acronyms the first time they are used in the text, even if they have been defined in the abstract. Abbreviations such as IEEE, SI, MKS, CGS, sc, dc, and rms do not have to be defined. Do not use abbreviations in the title unless they are unavoidable.

Text Layout for Peer Review:

Use single column layout, double spacing and wide (3 cm) margins on white paper at the peer review stage. Ensure that each new paragraph is clearly indicated. Present tables and figure legends in the text where they are related and cited. Number all pages consecutively; use 12 pt font size and standard fonts; Times New Roman, Helvetica, or Courier is preferred.

Research Papers should not exceed 12 printed pages in two-column publishing format, including figures and tables.

Technical Notes and *Letters* should not exceed 2,000 words.

Reviews should not exceed 20 printed pages in two-column publishing format, including figures and tables.

Equations:

Number equations consecutively with equation numbers in parentheses flush with the right margin, as in (1). To make equations more compact, you may use the solidus (/), the exp function, or appropriate exponents. Italicize Roman symbols for quantities and variables, but not Greek symbols. Use an dash (–) rather than a hyphen for a minus sign. Use parentheses to avoid ambiguities in denominators. Punctuate equations with commas or periods when they are part of a sentence, as in

$$C = a + b \qquad (1)$$

Symbols in your equation should be defined before the equation appears or immediately following. Use “Eq. (1)” or “equation (1),” while citing.

Figures and Tables:

All illustrations must be supplied at the correct resolution:

* Black and white and colour photos - 300 dpi

* Graphs, drawings, etc - 800 dpi preferred; 600 dpi minimum

* Combinations of photos and drawings (black and white and color) - 500 dpi

In addition to using figures in the text, upload each figure as a separate file in either .tiff or .eps format during submission, with the figure number.

Table captions should be written in the same format as figure captions; for example, “Table 1. Appearance styles.”. Tables should be referenced in the text unabbreviated as “Table 1.”

References:

Please ensure that every reference cited in the text is also present in the reference list (and viceversa). Any references cited in the abstract must be given in full. Unpublished results and personal communications are not recommended in the reference list, but may be mentioned in the text. Citation of a reference as “in press” implies that the item has been accepted for publication. Number citations consecutively in square brackets [1]. Punctuation follows the bracket [2]. Refer simply to the reference number, as in [3]. Use “Ref. [3]” or Reference [3]” at the beginning of a sentence: “Reference [3] was …”. Give all authors’ names; use “et al.” if there are six authors or more. For papers published in translated journals, first give the English citation, then the original foreign-language citation.

Books

[1] J. Clerk Maxwell*, A Treatise on Electricity and Magnetism,* 3rd ed., vol. 2. Oxford:Clarendon Press, 1892, pp.68-73.

Journals

[2] Y. Yorozu, M. Hirano, K. Oka, and Y. Tagawa, “Electron spectroscopy studies on magneto-optical media and plastic substrate interface”, *IEEE Transl. J. Magn. Japan*, vol. 2, pp. 740-741, August 1987.

Conferences

[3] Çolak I., Kabalci E., Bayindir R., and Sagiroglu S, “The design and analysis of a 5-level cascaded voltage source inverter with low THD”, *2nd PowerEng Conference*, Lisbon, pp. 575-580, 18-20 March 2009.

Reports

[4] IEEE Standard 519-1992, Recommended practices and requirements for harmonic control in electrical power systems, *The Institute of Electrical and Electronics Engineers*, 1993.

Text Layout for Accepted Papers:

A4 page margins should be margins: top = 24 mm, bottom = 24 mm, side = 15 mm. Main text should be given in two column. The column width is 87mm (3.425 in). The space between the two columns is 6 mm (0.236 in). Paragraph indentation is 3.5 mm (0.137 in). Follow the type sizes specified in Table. Position figures and tables at the tops and bottoms of columns. Avoid placing them in the middle of columns. Large figures and tables may span across both columns. Figure captions should be centred below the figures; table captions should be centred above. Avoid placing figures and tables before their first mention in the text. Use the abbreviation “Fig. 1,” even at the beginning of a sentence.

Type size (pts.)	Appearance		
	Regular	**Bold**	*Italic*
10	Authors' affiliations, Section titles, references, tables, table names, first letters in table captions,figure captions, footnotes, text subscripts, and superscripts	**Abstract**	
12	Main text, equations, Authors' names, [a]		*Subheading (1.1.)*
24	Paper title		

Submission checklist:

It is hoped that this list will be useful during the final checking of an article prior to sending it to the journal's Editor for review. Please consult this Guide for Authors for further details of any item. Ensure that the following items are present:

- ❖ One Author designated as corresponding Author:

• E-mail address

• Full postal address

• Telephone and fax numbers

- ❖ All necessary files have been uploaded

• Keywords: a minimum of 4

• All figure captions (supplied in a separate document)

• All tables (including title, description, footnotes, supplied in a separate document)

- ❖ Further considerations

• Manuscript has been "spellchecked" and "grammar-checked"

• References are in the correct format for this journal

• All references mentioned in the Reference list are cited in the text, and vice versa

• Permission has been obtained for use of copyrighted material from other sources (including the Web)

• Color figures are clearly marked as being intended for color reproduction on the Web (free of charge) and in print or to be reproduced in color on the Web (free of charge) and in black-and-white in print.

Article Template Containing Author Guidelines for Peer-Review

First Author*, Second Author**‡, Third Author***

*Department of First Author, Faculty of First Author, Affiliation of First Author, Postal address

**Department of Second Author, Faculty of First Author, Affiliation of First Author, Postal address

***Department of Third Author, Faculty of First Author, Affiliation of First Author, Postal address

(First Author Mail Address, Second Author Mail Address, Third Author Mail Address)

‡ Corresponding Author; Second Author, Postal address, Tel: +90 312 123 4567, Fax: +90 312 123 4567,corresponding@affl.edu

Received: xx.xx.xxxx Accepted:xx.xx.xxxx

Abstract- Enter an abstract of up to 250 words for all articles. This is a concise summary of the whole paper, not just the conclusions, and is understandable without reference to the rest of the paper. It should contain no citation to other published work. Include up to six keywords that describe your paper for indexing purposes. Define abbreviations and acronyms the first time they are used in the text, even if they have been defined in the abstract. Abbreviations such as IEEE, SI, MKS, CGS, sc, dc, and rms do not have to be defined. Do not use abbreviations in the title unless they are unavoidable.

Keywords- Keyword1; keyword2; keyword3; keyword4; keyword5.

2. Introduction

Authors should any word processing software that is capable to make corrections on misspelled words and grammar structure according to American or Native English. Authors may get help by from word

processor by making appeared the paragraph marks and other hidden formatting symbols. This sample article is prepared to assist authors preparing their articles to IJET.

Indent level of paragraphs should be 0.63 cm (0.24 in) in the text of article. Use single column layout, double-spacing and wide (3 cm) margins on white paper at the peer review stage. Ensure that each new paragraph is clearly indicated. Present tables and figure legends in the text where they are related and cited. Number all pages consecutively; use 12 pt font size and standard fonts; Times New Roman, Helvetica, or Courier is preferred. Indicate references by number(s) in square brackets in line with the text. The actual authors can be referred to, but the reference number(s) must always be given. Example: "..... as demonstrated [3, 6]. Barnaby and Jones [8] obtained a different result ...."

IJET accepts submissions in three styles that are defined as Research Papers, Technical Notes and Letter, and Review paper. The requirements of paper are as listed below:

- Research Papers should not exceed 12 printed pages in two-column publishing format, including figures and tables.
- Technical Notes and Letters should not exceed 2,000 words.
- Reviews should not exceed 20 printed pages in two-column publishing format, including figures and tables.

Authors are requested write equations using either any mathematical equation object inserted to word processor or using independent equation software. Symbols in your equation should be defined before the equation appears or immediately following. Use “Eq. (1)” or “equation (1),” while citing. Number equations consecutively with equation numbers in parentheses flush with the right margin, as in Eq. (1). To make equations more compact, you may use the solidus (/), the exp function, or appropriate exponents. Italicize Roman symbols for quantities and variables, but not Greek symbols. Use an dash (–) rather than a hyphen for a minus sign. Use parentheses to avoid ambiguities in denominators. Punctuate equations with commas or periods when they are part of a sentence, as in

$$C = a + b \tag{1}$$

Section titles should be written in bold style while sub section titles are italic.

3. Figures and Tables

3.1. Figure Properties

All illustrations must be supplied at the correct resolution:

- Black and white and colour photos - 300 dpi
- Graphs, drawings, etc - 800 dpi preferred; 600 dpi minimum
- Combinations of photos and drawings (black and white and colour) - 500 dpi

In addition to using figures in the text, Authors are requested to upload each figure as a separate file in either .tiff or .eps format during submission, with the figure number as Fig.1., Fig.2a and so on. Figures are cited as “Fig.1” in sentences or as “Figure 1” at the beginning of sentence and paragraphs. Explanations related to figures should be given before figure. Figures and tables should be located at the top or bottom side of paper as done in accepted article format.

Figure 1. Engineering technologies.

Table captions should be written in the same format as figure captions; for example, “Table 1. Appearance styles.”. Tables should be referenced in the text unabbreviated as “Table 1.”

Table 1. Appearance properties of accepted manuscripts

Type size (pts.)	Appearance		
	Regular	**Bold**	*Italic*
10	Authors’ affiliations, Abstract, keywords, references, tables, table names, figure captions, footnotes, text subscripts, and superscripts	**Abstract**	
12	Main text, equations, Authors’ names, Section titles		*Subheading (1.1.)*
24	Paper title		

4. Submission Process

The *International Journal of Engineering Technologies* operates an online submission and peer review system that allows authors to submit articles online and track their progress via a web interface. Articles that are prepared referring to this template should be controlled according to submission checklist given in “Guide f Authors”. Editor handles submitted articles to IJET primarily in order to control in terms of compatibility to aims and scope of Journal.

Articles passed this control are checked for grammatical and template structures. If article passes this control too, then reviewers are assigned to article and Editor gives a reference number to paper. Authors registered to online submission system can track all these phases.

Editor also informs authors about processes of submitted article by e-mail. Each author may also apply to Editor via online submission system to review papers related to their study areas. Peer review is a critical element of publication, and one of the major cornerstones of the scientific process. Peer Review serves two key functions:

- Acts as a filter: Ensures research is properly verified before being published
- Improves the quality of the research

5. Conclusion

The conclusion section should emphasize the main contribution of the article to literature. Authors may also explain why the work is important, what are the novelties or possible applications and extensions. Do not replicate the abstract or sentences given in main text as the conclusion.

Acknowledgements

Authors may acknowledge to any person, institution or department that supported to any part of study.

References

[1] J. Clerk Maxwell, *A Treatise on Electricity and Magnetism*, 3rd ed., vol. 2. Oxford:Clarendon Press, 1892, pp.68-73. (Book)

[2] H. Poor, *An Introduction to Signal Detection and Estimation*, New York: Springer-Verlag, 1985, ch. 4. (Book Chapter)

[3] Y. Yorozu, M. Hirano, K. Oka, and Y. Tagawa, "Electron spectroscopy studies on magneto-optical media and plastic substrate interface", *IEEE Transl. J. Magn. Japan*, vol. 2, pp. 740-741, August 1987. (Article)

[4] E. Kabalcı, E. Irmak, I. Çolak, "Design of an AC-DC-AC converter for wind turbines", *International Journal of Energy Research*, Wiley Interscience, DOI: 10.1002/er.1770, Vol. 36, No. 2, pp. 169-175. (Article)

[5] I. Çolak, E. Kabalci, R. Bayindir R., and S. Sagiroglu, "The design and analysis of a 5-level cascaded voltage source inverter with low THD", *2nd PowerEng Conference*, Lisbon, pp. 575-580, 18-20 March 2009. (Conference Paper)

[6] IEEE Standard 519-1992, Recommended practices and requirements for harmonic control in electrical power systems, *The Institute of Electrical and Electronics Engineers*, 1993. (Standards and Reports)

Article Template Containing Author Guidelines for Accepted Papers

First Author*, Second Author**‡, Third Author***

*Department of First Author, Faculty of First Author, Affiliation of First Author, Postal address

**Department of Second Author, Faculty of First Author, Affiliation of First Author, Postal address

***Department of Third Author, Faculty of First Author, Affiliation of First Author, Postal address

(First Author Mail Address, Second Author Mail Address, Third Author Mail Address)

‡ Corresponding Author; Second Author, Postal address, Tel: +90 312 123 4567,

Fax: +90 312 123 4567,corresponding@affl.edu

Received: xx.xx.xxxx Accepted:xx.xx.xxxx

Abstract- Enter an abstract of up to 250 words for all articles. This is a concise summary of the whole paper, not just the conclusions, and is understandable without reference to the rest of the paper. It should contain no citation to other published work. Include up to six keywords that describe your paper for indexing purposes. Define abbreviations and acronyms the first time they are used in the text, even if they have been defined in the abstract. Abbreviations such as IEEE, SI, MKS, CGS, sc, dc, and rms do not have to be defined. Do not use abbreviations in the title unless they are unavoidable.

Keywords Keyword1, keyword2, keyword3, keyword4, keyword5.

1. Introduction

Authors should any word processing software that is capable to make corrections on misspelled words and grammar structure according to American or Native English. Authors may get help by from word processor by making appeared the paragraph marks and other hidden formatting symbols. This sample article is prepared to assist authors preparing their articles to IJET.

Indent level of paragraphs should be 0.63 cm (0.24 in) in the text of article. Use single column layout, double-spacing and wide (3 cm) margins on white paper at the peer review stage. Ensure that each new paragraph is clearly indicated. Present tables and figure legends in the text where they are related and cited. Number all pages consecutively; use 12 pt font size and standard fonts; Times New Roman, Helvetica, or Courier is preferred. Indicate references by number(s) in square brackets in line with the text. The actual authors can be referred to, but the reference number(s) must always be given. Example: "..... as demonstrated [3,6]. Barnaby and Jones [8] obtained a different result ...."

IJET accepts submissions in three styles that are defined as Research Papers, Technical Notes and Letter, and Review paper. The requirements of paper are as listed below:

- Research Papers should not exceed 12 printed pages in two-column publishing format, including figures and tables.
- Technical Notes and Letters should not exceed 2,000 words.
- Reviews should not exceed 20 printed pages in two-column publishing format, including figures and tables.

Authors are requested write equations using either any mathematical equation object inserted to word processor or using independent equation software. Symbols in your equation should be defined before the equation appears or immediately following. Use “Eq. (1)” or “equation (1),” while citing. Number equations consecutively with equation numbers in parentheses flush with the right margin, as in Eq. (1). To make equations more compact, you may use the solidus (/), the exp function, or appropriate exponents. Italicize Roman symbols for quantities and variables, but not Greek symbols. Use an dash (-) rather than a hyphen for a

minus sign. Use parentheses to avoid ambiguities in denominators. Punctuate equations with commas or periods when they are part of a sentence, as in

$$C = a + b \quad (1)$$

Section titles should be written in bold style while sub section titles are italic.

6. Figures and Tables

6.1. Figure Properties

All illustrations must be supplied at the correct resolution:

- Black and white and colour photos - 300 dpi
- Graphs, drawings, etc - 800 dpi preferred; 600 dpi minimum
- Combinations of photos and drawings (black and white and colour) - 500 dpi

In addition to using figures in the text, Authors are requested to upload each figure as a separate file in either .tiff or .eps format during submission, with the figure number as Fig.1., Fig.2a and so on. Figures are cited as "Fig.1" in sentences or as "Figure 1" at the beginning of sentence and paragraphs. Explanations related to figures should be given before figure.

Fig. 1. Engineering technologies.

Figures and tables should be located at the top or bottom side of paper as done in accepted article format. Table captions should be written in the same format as figure captions; for example, "Table 1. Appearance styles.". Tables should be referenced in the text unabbreviated as "Table 1."

Table 1. Appearance properties of accepted manuscripts

Type size (pts.)	Appearance		
	Regular	**Bold**	*Italic*
10	Main text, section titles, authors' affiliations, abstract, keywords, references, tables, table names, figure captions, equations, footnotes, text subscripts, and superscripts	**Abstract-**	*Subheading (1.1.)*
12	Authors' names,		
24	Paper title		

6.2. Text Layout for Accepted Papers

A4 page margins should be margins: top = 24 mm, bottom = 24 mm, side = 15 mm. The column width is 87mm (3.425 in). The space between the two columns is 6 mm (0.236 in). Paragraph indentation is 3.5 mm (0.137 in). Follow the type sizes specified in Table. Position figures and tables at the tops and bottoms of columns. Avoid placing them in the middle of columns. Large figures and tables may span across both columns. Figure captions should be centred below the figures; table captions should be centred above. Avoid placing figures and tables before their first mention in the text. Use the abbreviation "Fig. 1," even at the beginning of a sentence.

7. Submission Process

The International Journal of Engineering Technologies operates an online submission and peer review system that allows authors to submit articles online and track their progress via a web interface. Articles that are prepared referring to this template should be controlled according to submission checklist given in "Guide f Authors". Editor handles submitted articles to IJET primarily in order to control in terms of compatibility to aims and scope of Journal. Articles passed this control are checked for grammatical and template structures. If article passes this control too, then reviewers are assigned to article and Editor gives a reference number to paper. Authors registered to online submission system can track all these phases. Editor also informs authors about processes of submitted article by e-mail. Each author may also apply to Editor via online

submission system to review papers related to their study areas. Peer review is a critical element of publication, and one of the major cornerstones of the scientific process. Peer Review serves two key functions:

- Acts as a filter: Ensures research is properly verified before being published
- Improves the quality of the research

8. Conclusion

The conclusion section should emphasize the main contribution of the article to literature. Authors may also explain why the work is important, what are the novelties or possible applications and extensions. Do not replicate the abstract or sentences given in main text as the conclusion.

Acknowledgements

Authors may acknowledge to any person, institution or department that supported to any part of study.

References

[7] J. Clerk Maxwell, A Treatise on Electricity and Magnetism, 3rd ed., vol. 2. Oxford:Clarendon Press, 1892, pp.68-73. (Book)

[8] H. Poor, An Introduction to Signal Detection and Estimation, New York: Springer-Verlag, 1985, ch. 4. (Book Chapter)

[9] Y. Yorozu, M. Hirano, K. Oka, and Y. Tagawa, "Electron spectroscopy studies on magneto-optical media and plastic substrate interface", IEEE Transl. J. Magn. Japan, vol. 2, pp. 740-741, August 1987. (Article)

[10] E. Kabalcı, E. Irmak, I. Çolak, "Design of an AC-DC-AC converter for wind turbines", International Journal of Energy Research, Wiley Interscience, DOI: 10.1002/er.1770, Vol. 36, No. 2, pp. 169-175. (Article)

[11] I. Çolak, E. Kabalci, R. Bayindir R., and S. Sagiroglu, "The design and analysis of a 5-level cascaded voltage source inverter with low THD", 2nd PowerEng Conference, Lisbon, pp. 575-580, 18-20 March 2009. (Conference Paper)

[12] IEEE Standard 519-1992, Recommended practices and requirements for harmonic control in electrical power systems, The Institute of Electrical and Electronics Engineers, 1993. (Standards and Reports)

INTERNATIONAL JOURNAL OF ENGINEERING TECHNOLOGIES (IJET)
COPYRIGHT AND CONSENT FORM

This form is used for article accepted to be published by the IJET. Please read the form carefully and keep a copy for your files.

TITLE OF ARTICLE (hereinafter, "The Article"):

……..…….....……

……..…….....……

……...……..……

LIST OF AUTHORS:

……..……...…..……

……..…….....……

……..……..……

CORRESPONDING AUTHOR'S ("The Author") NAME, ADDRESS, INSTITUTE AND EMAIL:

……..……

……..…….....……

……...……..……..…

COPYRIGHT TRANSFER

The undersigned hereby transfers the copyright of the submitted article to International Journal of Engineering Technologies (the "IJET"). The Author declares that the contribution and work is original, and he/she is authorized by all authors and/or grant-funding agency to sign the copyright form. Author hereby assigns all including but not limited to the rights to publish, distribute, reprints, translates, electronic and published derivates in various arrangements or any other versions in full or abridged forms to IJET. IJET holds the copyright of Article in its own name.

Author(s) retain all rights to use author copy in his/her educational activities, own websites, institutional and/or funder's web sites by providing full citation to final version published in IJET. The full citation is provided including Authors list, title of the article, volume and issue number, and page number or using a link to the article in IJET web site. Author(s) have the right to transmit, print and share the first submitted copies with colleagues. Author(s) can use the final published article for his/her own professional positions, career or qualifications by citing to the IJET publication.

Once the copyright form is signed, any changes about the author names or order of the authors listed above are not accepted by IJET.

Authorized/Corresponding Author **Date/ Signature**